Advanced Powder Materials 4 (2025) 100300

Contents lists available at ScienceDirect

Advanced Powder Materials

journal homepage: www.keaipublishing.com/en/journals/advanced-powder-materials

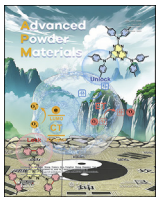

Recent progress on high-precision construction of nanoarchitectured SERS substrates for ultrasensitive bio-medical sensors

Heguang Liu [a,*], Ben Mou [a], Jinxin Li [b], Na Tian [a], Yiming Feng [c], Xiaodong Cui [d], Yury Kapitonov [e], Huageng Liang [c,**], Caiyin You [a,***], Yuan Li [b,****], Tianyou Zhai [b]

[a] School of Materials Science and Engineering, Xi'an University of Technology, Xi'an 710048, China
[b] State Key Laboratory of Materials Processing and Die & Mould Technology, School of Materials Science and Engineering, Huazhong University of Science and Technology, Wuhan 430074, China
[c] Union Hospital, Tongji Medical College, Huazhong University of Science and Technology, Wuhan 430022, China
[d] Physics Department, University of Hong Kong, Hong Kong, China
[e] Department of Photonics, Saint Petersburg State University, Saint Petersburg, 199034, Russia

ARTICLE INFO

Keywords:
SERS
SERS substrates
High-precision construction
Ultrasensitive bio-medical sensors
Enhancement mechanism

ABSTRACT

Surface-enhanced Raman spectroscopy (SERS) has evolved from a laboratory technique to a practical tool for ultra-sensitive detection, particularly in the biomedical field, where precise molecular identification is crucial. Despite significant advancements, a gap remains in the literature, as no comprehensive review systematically addresses the high-precision construction of SERS substrates for ultrasensitive biomedical detection. This review fills that gap by exploring recent progress in fabricating high-precision SERS substrates, emphasizing their role in enabling ultrasensitive bio-medical sensors. We carefully examine the key to these advancements is the precision engineering of substrates, including noble metals, semiconductors, carbon-based materials, and two-dimensional materials, which is essential for achieving the high sensitivity required for ultrasensitive detection. Applications in biomedical diagnostics and molecular analysis are highlighted. Finally, we address the challenges in SERS substrate preparation and outline future directions, focusing on improvement strategies, design concepts, and expanding applications for these advanced materials.

1. Introduction

Surface-enhanced Raman spectroscopy (SERS) is a Raman scattering effect that amplifies the signal intensity of molecules adsorbed on specific substrates [1]. It overcomes the low sensitivity of conventional Raman testing, enabling single-molecule detection [2]. Since its first discovery in 1974 and following the refinements of the mechanism by Van Duyne et al. and Albrecht et al., along with decades of continuous efforts and exploration by researchers, SERS has developed into a spectroscopic analysis technique that boasts advantages such as non-destructiveness, speed, convenience, efficiency, and high sensitivity-qualities that other techniques like infrared [3–6]. Thanks to these attractive merits, the SERS technique has been widely utilized in fields of trace and ultra-trace chemical molecule detection, as well as non-destructive biomolecule detection [7].

High-quality substrate materials are essential for SERS technology. In recent years, significant progress has been achieved in precisely constructing nanostructured substrates, involving feature-structured noble metal substrates, noble-free metal substrates, and noble metal composite substrates [8,9]. Notably, the feature-structured noble metal substrates achieved through nanostructure design, including nanorings (NRs), nanoframes (NFs), and nanoaggregates, generally exhibit an enhancement factor (EF) of 10^{10}~10^{12} [10–14]. This can be attributed to the exceptional physical characteristics of noble metals. For example, the negative fundamental dielectric constant is believed to significantly stimulate localized surface plasmon resonance (LSPR). Simultaneously,

* Corresponding authors.
** Corresponding author.
*** Corresponding authors.
**** Corresponding author.
E-mail addresses: heguangliu@xaut.edu.cn (H. Liu), leonard19800318@hust.edu.cn (H. Liang), caiyinyou@xaut.edu.cn (C. You), yuanli1@hust.edu.cn (Y. Li).
Peer review under the responsibility of Central South University.

https://doi.org/10.1016/j.apmate.2025.100300
Received 23 February 2025; Received in revised form 19 April 2025; Accepted 2 May 2025
Available online 15 May 2025

the novel noble-free metal substrates (e.g., metal oxide substrates, carbon-based material substrates, transition metal dichalcogenides (TMDs) substrates, layered double hydroxides (LDHs) substrates) precisely engineered via elements doping and bandgap regulation, can regulate the molecular polarization rate of the substrate material, thereby enhancing charge transfer (CT) and leading to a high EF of 10^6~10^8 [15–18]. Moreover, the composite substrates consist of noble metal particles and matrix materials, which involve carbon, metal-organic frameworks (MOFs), two-dimensional (2D) materials, and organic materials composite substrates, etc. [19–22]. In these substrates, the noble metal particles can offer strong electromagnetic enhancement (EM), while the shape control of the matrix material can manipulate the spacing of the noble metal particles, further enhancing the EM [23]. Nanoscale energy level regulation of some matrix materials, such as black phosphorus (BP), transition metal nitrides (TMNs), MXene, etc., can interact with probe molecules to provide CM. Consequently, the noble metal composite material attains excellent SERS performance due to the synergistic effect of EM and chemical enhancement (CM).

Benefiting from significant advancements in high-precision SERS substrates, SERS technology has been extensively utilized thus far in molecule detection and ultra-sensitive biological sensors [24–26]. Such as cancer analysis and monitoring, human health monitoring, small molecule analysis in plants, pesticide residue detection, and explosive molecule detection [27–32]. By carefully creating nanostructured substrates, it is feasible to significantly and reliably amplify the Raman signals of probe molecules and to identify specific compounds reliably [33,34].

In view of the current vigorous development of high-precision substrate preparation and application, it is necessary to conduct a systematic review of the progress in this field. Previous reviews have discussed the applications of various materials in the preparation of SERS substrates and their performance in specific application scenarios. However, the focus has mainly been on the performance of particular types of materials and their applications under conventional conditions. For instance, the advantages and disadvantages of MXene materials as SERS substrates and their performance in analytical chemistry, the preparation methods of semiconductor material SERS substrates and their improvements, the advantages of using MOFs materials in the preparation of SERS substrates and some applications in small molecule analysis, among others [35–37]. Up to date, little effort has been devoted to providing a comprehensive and systematic summary of the construction of various new materials for ultra-sensitive nano-structured SERS substrates and their applications in environments requiring ultra-sensitivity.

Herein, we aim to comprehensively review the latest advances in high-precision nanostructured SERS substrates and applications in ultra-sensitive environmental monitoring (Fig. 1). We briefly introduce two SERS enhancement mechanisms (EM and CM). Then, we summarized the current research status on the preparation of high-precision SERS substrates, categorizing them into electromagnetic-enhanced substrates (characteristic structure noble metal substrate, noble metal composite substrate), chemical-enhanced substrates, and co-enhanced substrates (electromagnetic co-chemically enhanced substrate, electromagnetic co-enrichment strategy substrate) based on the enhancement mechanism. We focus on exploring how various substrates can be strengthened through nanostructure design, specifically examining the relationship between their nanostructure construction and the reinforcement effect. Furthermore, we discuss the application of high-precision substrates in various ultra-sensitive environments, including ultra-sensitive biomedical sensors, micro, trace small molecule analysis and detection. Finally, based on our summary and understanding of the field, we provide insights into the challenges and development prospects of high-precision SERS substrates, focusing on the improvement strategies, design ideas, and application expansion of various high-precision substrates. We indeed hope this work will provide a fundamental understanding of the design, construction, and application of high-precision SERS substrates.

2. Raman enhancement mechanism

The intensity of Raman scattered light (I) is proportional to the square of the induced electric dipole moment of the molecule, where $P=\alpha \cdot E$, α is the molecular polarizability tensor, and E is the electric field strength [38,39]. Therefore, the intensity of Raman scattering may be enhanced by increasing the molecular polarizability tensor or the strength of the electric field around the molecule. The EM and CM models can reasonably explain the enhancement of Raman signals through changes in electric field strength and molecular polarizability tensor within a specific range.

2.1. Electromagnetic enhancement mechanism

Electromagnetic enhancement is a phenomenon that occurs on the surfaces of unique nanostructures, where the local electromagnetic field significantly amplifies the Raman signal intensity of molecules within its range. Specifically, when an electromagnetic wave impinges upon a metal surface, the distribution of free electrons on the metal surface becomes non-uniform. The positive (negative) electrons shift towards the

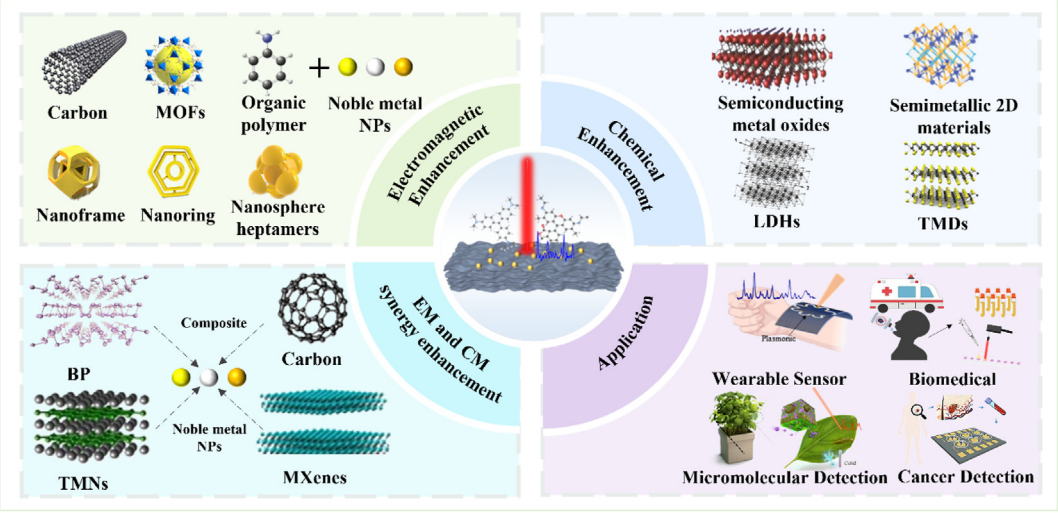

Fig. 1. High-precision classification and application overview of SERS substrates, including electromagnetic enhanced substrate, chemical enhanced substrate, coordinated enhanced substrate, and application [38–44].

remaining negative (positive) charge region under the effect of Coulomb force and acquire momentum, thereby enriching the positive (negative) electrons in this region. The enriched charged particles will cause the charge to depart from this region due to the repulsion among the same type of charges, thus forming a positive (negative) charge shock wave that vibrates up and down around the negative (positive) region (Fig. 2a). Surface plasmon plasmons (SPPs) are formed. Additionally, the free electrons on the metal surface oscillating up and down within the fixed positive charge region have their fixed frequency. When the frequency of the incident electromagnetic wave is equivalent to this frequency, the free electrons will undergo a collective resonance, known as surface plasma resonance (SPR). The field strength of the surface plasmon resonance reaches its maximum at the metal surface and then decreases exponentially in the direction perpendicular to the interface. Because the electron concentration of the continuous metal film is exceptionally high, the frequency of the plasma oscillation wave is also very high, approximately 10 THz [40]. Metal nanoparticles (NPs) possess far fewer free electrons than metal films, so their oscillation frequency can be reduced to the visible region. The wavelength at the resonance frequency generates intense light absorption, that is, LSPR. Noble metal NPs such as Au, Ag, and Cu have stronger LSPR, enabling them to obtain a stronger SERS signal. The size, morphology, and spacing of metal nanomaterials significantly influence LSPR.

In general, when a single molecule is placed in the LSPR region, its Raman scattering cross section is enhanced from 10^{-31} to 10^{-29} to 10^{4} $\sim 10^{12}$ times the original. Its specific enhancement principle is shown in Fig. 2b: When the incident photon beam with wavelength λ_0 interacts with the nanostructure, the incident field E_0 is locally enhanced so that the molecules in the range of the NPs feel the enhanced electric field intensity E_{LOS} (E_{LOS}=$M_{loc}(\lambda_0)$ E_0, $M_{loc}(\lambda_0)$ is the local electric field EF).

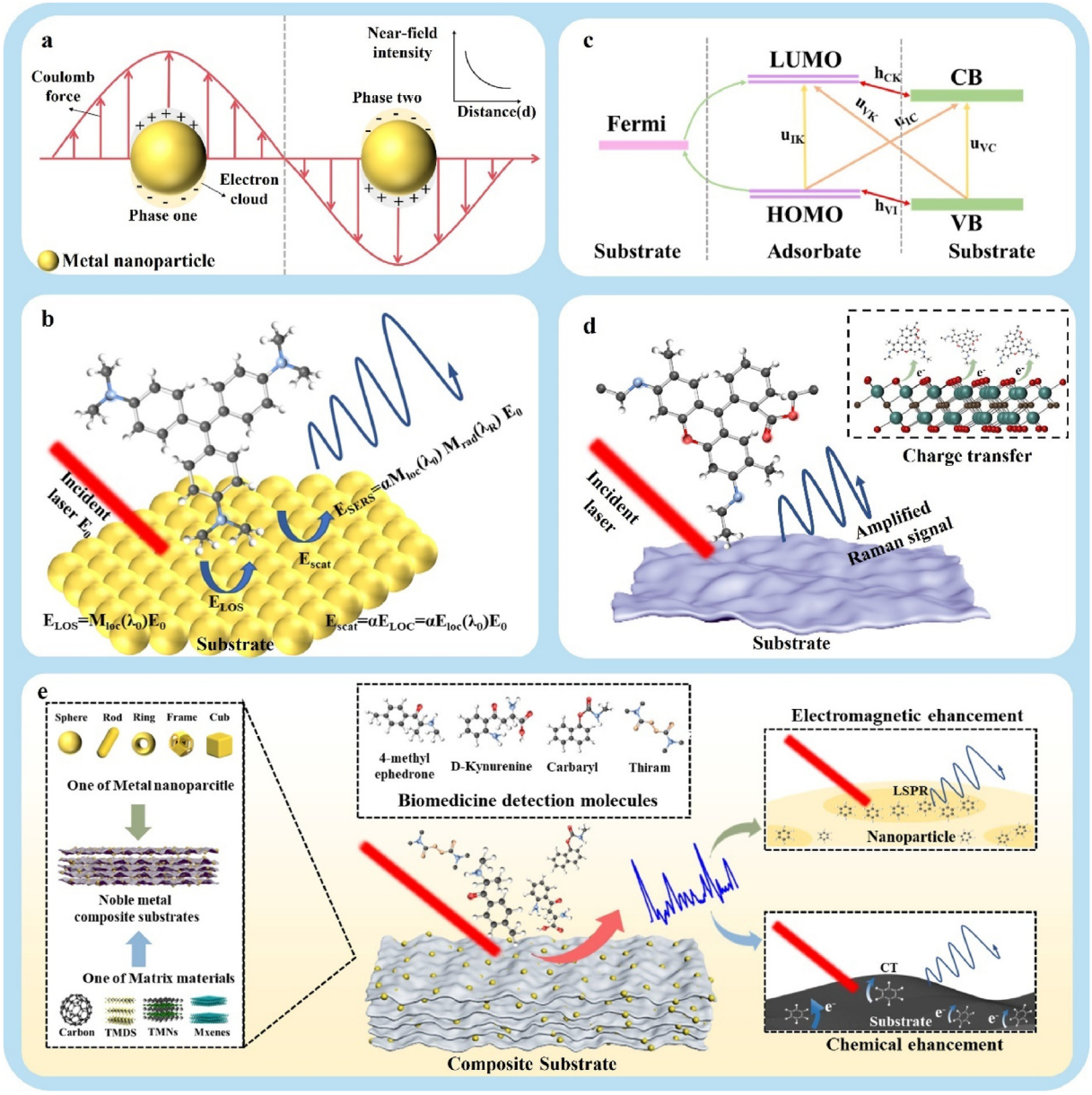

Fig. 2. Diagram of the enhanced mechanism of SERS. (a) Local electric field distribution of metal NPs. The near-field intensity decays exponentially with the increase of distance normal to the surface. (b) The schematic diagram of SERS electromagnetic enhancement. (c) CM mechanism between substrate and molecular. (d) The schematic diagram of SERS chemical enhancement. (e) Collaborative electromagnetic and chemical enhancement mechanisms. Schematic diagram and enhanced principle of detecting small biomedical molecules (4-methyl ephedrone, D-Kynurenine, Carbaryl, Thiram) on SERS substrate composite with precious metal particles [42,44].

Then, when these molecules are excited by the E_{LOS} electric field, they scatter Raman signals (wavelength λ_R, $\lambda_R \neq \lambda_0$), and the scattering field E_{scat} ($E_{scat}=\alpha E_{LOC}=\alpha M_{loc}(\lambda_0)\ E_0$) at wavelength λ_R is also enhanced compared with the molecules without nanostructures. This scattering field will interact with the NPs and get enhanced again, and this field that gets enhanced again by radiation can be expressed as $E_{SERS}=M_{rad}(\lambda_R)\ E_{scat}=M_{rad}(\lambda_R)\alpha E_{LOC}=\alpha M_{loc}(\lambda_0)M_{rad}(\lambda_R)E_0$. Thus, the SERS signal intensity of the molecule near the NPs was enhanced as $I_{SERS}\propto|E_{SERS}|^2=|\alpha M_{loc}(\lambda_0)\ M_{rad}(\lambda_R)|^2E_0^2$. In general, M_{rad} and M_{loc} values are close, so the SERS signal strength can be expressed as $I_{SERS}\propto\alpha^2M_{loc}^4E_0^2$. The field enhancement could occur twice in succession for a specific incident wavelength. At each stage, the electric field was enhanced by M_{loc}^2, and the total electric field sensed by the molecule was enhanced to M_{loc}^4 so that the SERS effect would be pronounced [41].

2.2. Chemical enhancement mechanism

Researchers discovered that several events could not be explained by mechanisms involving increased electromagnetic fields during the Raman experiment. For instance, altering the voltage of the Ag electrode would alter the Raman signal strength linked to the absorption molecule on the electrode surface, and some non-plasma metal surfaces would exhibit an amplification of the Raman signal, etc. These observations imply the existence of at least one additional mechanism, namely CM (Fig. 2c and d), which differs from electromagnetic field enhancement.

The differences in the current CM methods can be attributed to chemical reinforcement caused by CT. Stated differently, the CT process between the absorbent molecule and the metal surface is attributed to another mechanism distinct from EM [42]. Typically, the CT effect is obtained by raising the absorption target's polarization rate (α), which enlarges the Raman signal [43]. The presence of the CT effect leads to a higher Raman interval of the molecule, indicating a higher polarization rate of the absorption molecular tension. Various types of CT processes have used appropriate laser stimulation to amplify Ramana signals, mainly through optical-induced charge transfer (PICT) and base-state load transfer (GSCT) [44]. The Raman signal is enhanced by the Raman resonance effect, which involves laser jumping (μ_{VC}) between the conductive bands (CB) and underlying price bands (VB) and jumping between the molecule's maximum occupying molecular orbit (HOMO) and the least unoccupied molecular orbit (LUMO) (μ_{IK}) [45]. Conventional CT methods produce CT intermediates with longer Raman intervals by interacting between the molecule's HOMO or LUMO energy level and the underlying Fermi energy level [46,47]. Conversely, the PICT process takes place between HOMO and CB (μ_{IC}) CK or LUMO and VB (μ_{VK}), and the Herzberg-Teller logic (h_{VI} and h_{CK}) may even exploit this process to harness the energy of Germanic leaping or self-sonic jumping [48]. Furthermore, the GSCT effect may also be produced by molecules interacting with the conductive substrate, which raises the molecular polarization rate tension (h_{VI}) and produces a Raman amplification [49]. Strong electromagnets often cover chemical reinforcement because the impact of CM is restricted, and the EF is typically between 0.3 and 100, which is significantly lower than that of electromagnetic field enhancement [50].

2.3. Synergistic enhancement mechanism

Noble metal composite substrates consistently demonstrate superior SERS performance due to the synergistic interaction between noble metal particles and matrix materials, which enhances SERS through two distinct mechanisms. The noble metal composite substrate shown in Fig. 2e allows for combining noble metal particles with various shapes and matrix materials through structural design strategies. When a probe molecule is positioned on the substrate surface, the LSPR excited by noble metal particles generates a strong EM, while CT between the matrix material and the probe molecule contributes to the CM. The SERS signal of the probe molecule results from the combined enhancements of EM and CM.

3. Preparation of SERS substrates

3.1. SERS substrate of electromagnetic enhancement mechanisms

3.1.1. Characteristics of the structure of the noble metal substrate

Noble metal NPs (Au, Ag, and Cu) possess unique physical properties, such as a negative dielectric constant, which leads to significant LSPR and strong EM amplification [51]. This makes them ideal materials for constructing high EFs with low detection limits on advanced substrates. Moreover, because LSPR is highly sensitive to nanoparticle size, shape, and environment, researchers have developed complex plasmonic nanostructures to focus and enhance LSPR in confined spaces. Researchers have designed various plasmonic nanostructures, including NRs (Fig. 3a), NFs (Fig. 3b), chiral triangular NRs (Fig. 3c), and nanosphere heptamers (Fig. 3d), which significantly enhance the SERS properties of the substrate.

NRs are used as SERS substrates due to their large surface-to-volume ratio, enhanced electric field within the cavity, and symmetrical structure, which responds to light regardless of polarization direction. Each nanoring contains multiple smaller NRs within its interior, forming surface plasmon pairs that significantly amplify near-field focus. To enhance near-field focusing, Yoo et al. created Au nanoring structures (ANITs) using a multistep synthesis approach [52]. As shown in Fig. 3a, three rings are interleaved within a single structure. The near-field focusing ability of ANIT was studied by comparing it with an Au double nanoring sample. Two samples were compared: one resembling an ANIT without the middle NRs, and the other similar to an ANIT without the outer NRs. The simulated near-field focusing maps of a typical single particle for ANIT and Au double NRs are shown in Fig. 3e (i), (ii), and (iii), using 2-Naphthalenethiol (2-NTT) as a probe molecule. A comparison of Fig. 3e, f shows that the outer ring plays a crucial role in absorbing light and enhancing near-field focusing. ANITs with two circular nanogaps can efficiently focus the incident electromagnetic field onto a single nanostructure. The electric near field is significantly enhanced within the circular nanogap of the outer ring, leading to a substantial Raman enhancement of the absorbed analyte with EF=10^9. Yoo et al. also created Ag double NRs, with a circular nanocap sandwiched between two NRs of different diameters [53]. With EF of 7×10^8 and detection limit (LOD) of 10^{-7} M, it features a circular hot region due to strong surface plasmon coupling between the inner and outer NRs. Using a multistep reaction, Lee et al. fabricated heterometallic (Au-Pt-Au) NRs consisting of three intertwined rings [54]. The small circular nanogap between the inner and outer rings greatly enhances the electromagnetic near field through intraparticle coupling, boosting localized SERS at the single-particle level.

Nanoframes (NFs) feature internal open spaces and thin metallic ridges, enabling efficient light-matter interaction and the formation of various nano-gaps within a single structure, making them promising SERS substrates. Haddadnezhad et al. prepared an Au double-walled nanoframe (Au DWFs), with a single-walled truncated octahedral nanoframe nested in a core-shell configuration (Fig. 3b) [55]. Electromagnetic near-field focusing is enhanced as the gap between the inner and outer flat-walled frames narrows. When excited at 785 nm under different polarized light conditions, the surface charge density distribution and the electromagnetic near-field enhancement map of the double-walled nanoframe are shown in Fig. 3f (i) (ii). Oscillation of the electric field along the x-axis generates only weak hot spots between the inner and outer open frames. In contrast, excitation along the y-axis strongly enhances the near-field from the inner flat terrace to the outer terrace and from edge to edge. The combination of these two plasmon couplings leads to a significantly enhanced EF with a detection limit of 0.5 ppm. Similarly, Hila et al. fabricated an elongated pseudo-hollow nanoframe, consisting of four rectangular plates enclosing the sides and two open-frame ends, referred to as an Au dodecahedral wall nanoframe [56]. It exhibits an atomic-level molar detection limit for benzenethiol (BT) with LOD=10^{-18} M and EF=1.1×10^6. Zhao et al. prepare an Au

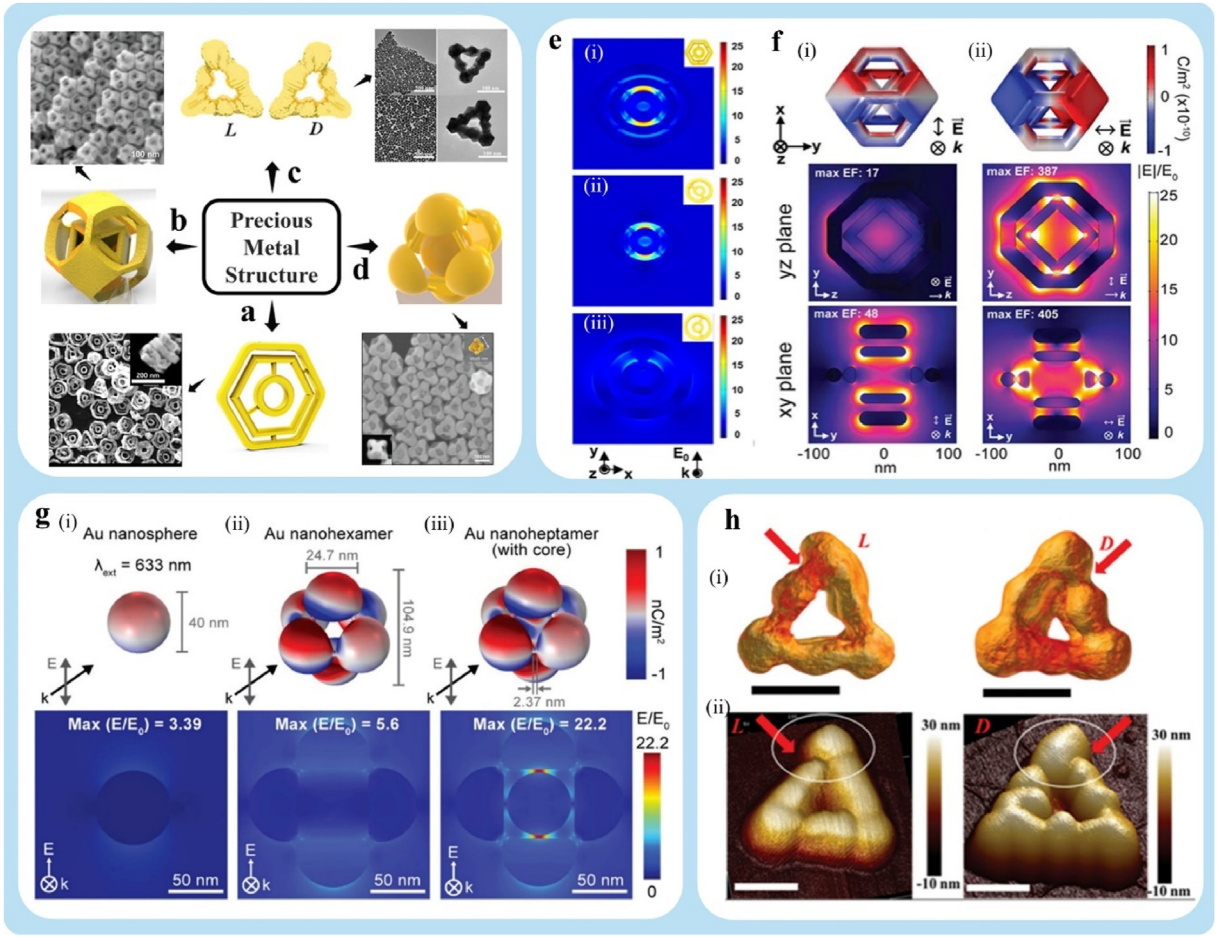

Fig. 3. (a) Schematic and SEM image of ANITs. Copyright 2021, American Chemical Society. (b) Schematic and SEM image of Au DWFs. Copyright 2023, American Chemical Society. (c) Schematic and SEM image of TNRs. Copyright 2021, Willey. (d) Schematic and SEM image of Au NHTs. Copyright 2024, American Chemical Society. (e) Contour maps of (i) ANITs, (ii) Au double NRs with middle and core rings, and (iii) Au double NRs with outer and core rings, respectively, enhanced by electric fields. Copyright 2021, American Chemical Society. (f) Au DWFs surface charge and field distribution pictures under 785 nm excitation with (i) x-axis and (ii) y-axis light polarization orientations. Copyright 2023, American Chemical Society. (g) Distribution of surface charge and electric field for (i) Au NSs, (ii) Au NHXs, and (iii) Au NHTs excited at 633 nm. Copyright 2024, American Chemical Society. (h) Electric-field simulation for (i) $_{L}$-Pt@Au TNRs and (ii) $_{D}$-Pt@Au TNRs. Copyright 2021, Willey.

truncated octahedral double-edge nanoframe with two functional surfaces [57]. It includes (1) eight thermally formed nanocaps from hexagonal nanoframes, with the hexagonal nanoframe containing core circular NRs for near-field focusing, and (2) six flat squares, enabling the formation of an ordered nanoframe array through self-assembly. Using 2-NTT as a probe, the SERS performance showed EF=10^{7} and LOD=10^{-17} M.

Chiral plasmonic nanostructures are highly effective for studying protein structure and dynamics due to their unique SERS-chiral anisotropy (SERS-ChA) effect [58]. They enable efficient and versatile enantioselective discrimination of enantiomers in various chiral molecules [59]. Wang et al. used a wet chemical process to fabricate chiral triangular Au NRs ($_{L/D}$-Pt@Au TNRs) with a Pt frame (Fig. 3c) [60]. The Pt@Au TNRs exhibit a hollow triangular morphology. Fig. 3h (i) and (ii) present the electric field simulations of $_{L}$-Pt@Au TNRs and $_{D}$-Pt@Au TNRs, respectively. The $_{L/D}$-Pt@Au TNRs exhibit strong optical activity. Due to the selective resonant coupling between the induced electric and magnetic dipoles of the enantiomers and the chiral plasmonic TNRs—an effect known as SERS-ChA—they can effectively distinguish between enantiomers. The chiral $_{D}$-Pt@Au TNRs serve as a label-free SERS platform. Aβ monomer, a marker for the detection of Alzheimer's Disease (AD), specifically Amyloid-β ($A\beta_{42}$) with 42 residues, shows a LOD of 4.5×10^{-15} M. Due to the unique SERS-ChA effect, chiral plasmonic nanostructures allow for efficient and versatile enantioselective discrimination of enantiomers from various chiral molecules.

Using Au nanospheres (Au NSs) as building blocks to construct spatial components is an effective strategy to endow nano-systems with unique optical properties. Fig. 3c shows how Zhao et al. created Au nanoheptamers (Au NHX) with an open structural layout [61]. The structure consists of six Au NSs arranged around a central Au sphere, connected by thin metal bridges in an octahedral pattern. A strong electromagnetic near-field is generated by the multiple hot spots formed between the nanospheres in the Au NHX. The surface charge, electric field distribution, and spectra of Au NSs, Au NHX, and Au nanoheptons (Au NHTs) are shown in Fig. 3g (i), (ii), and (iii). Under 633 nm excitation, simulations of the electric field distribution were performed, followed by bulk SERS measurements, showing electromagnetic near-field enhancements of 3.39 for Au NSs and 5.6 for Au NHX. A substantial near-field amplification is produced in the nanogap between the inner core Au and the six outer Au NSs when an additional inner core Au sphere is inserted. The increase in SERS is due to the Au NSs embedded in the Au NHT core, resulting in the highest EF of 22.2. The Au NHTs exhibit an extremely low detection limit (10^{-15} M) and a wide detectable range (10^{-5} to 10^{-15} M). Examples of such assemblies include one-dimensional (1D) chain structures, 2D trimer structures, and three-dimensional (3D) hexamer structures [62]. Kim et al. prepared plasmonic ring-shaped Au nanosphere hexamers (PCHs), resulting in highly uniform, repeatable, and polarization-independent single-particle SERS signals, with EF=3.8×10^{7}

and LOD=10^{-7} M [63]. In terms of performance and application, other Au nanosphere assemblies fall short of the heptamer.

The noble metal substrate exhibits an excellent EF, high SERS sensitivity, and the capability to detect trace quantities. However, repeatability remains a major challenge for the practical application of well-defined noble metal substrates due to the localized nature of LSPR. Additionally, noble metal substrates require extensive modification due to the high cost of precursor materials and the complex procedures needed to fabricate the fine features necessary for significant SERS enhancement. Moreover, the active surface of plasmonic metal NPs is unstable and can undergo chemical changes when stored for extended periods. As a result, plasmonic metal-based SERS may lose sensitivity and reproducibility, increasing overall operational costs.

3.1.2. *Noble metal composite structure substrate*

Noble metal NPs leverage their strong LSPR effect to achieve enhanced SERS performance. However, the localized nature of LSPR and the stability of the active surface of plasmonic metal NPs pose challenges to reproducibility, which limits their application in many areas. Material engineering, advanced manufacturing, and operational safeguards can all help to improve the stability of noble metal SERS substrates. These techniques strike a balance between plasmonic performance and durability, allowing for reliable, reproducible sensing in practical applications. For example, noble metal composite substrates formed by embedding noble metal particles into other materials can address the issues of stability and reproducibility. In noble metal composite substrates, noble metal particles provide strong LSPR, ensuring significant EM, while the matrix materials offer active sites for particle attachment and control particle spacing to ensure stability. Various materials have been developed for the preparation of noble metal composite substrates, including carbon materials, semiconductor oxides, TMDs, MOFs, organic materials, and MXenes.

Carbon-based materials possess several outstanding properties, including low toxicity, chemical inertness, and biocompatibility. Notably, they are easy to prepare, feature a larger specific surface area, and offer more active sites. They hold significant potential in the development of noble metal composite substrates [64]. For instance, Nong et al. developed SERS substrates by modifying graphene nanoribbons (GNRs) with Ag NPs (Fig. 4a) [65]. The arrangement from top to bottom includes a spacer dielectric, an Au reflector, a bilayer GNR, and Ag NPs. Fig. 4b illustrates the substrate production process. Simultaneous modulation of the local plasmon resonance of GNRs in the mid-infrared region and Ag NPs in the visible region allows for effective SERS. Fig. 4c shows the equivalent spatial distributions of the electric fields of graphene and metal plasmons. The hot spot of the graphene plasmon mode is confined to the edge of the GNR. The substrate's SERS performance, with an EF of 10^5 and an LOD of 10^{-9} M for Rhodamine 6G (R6G), also

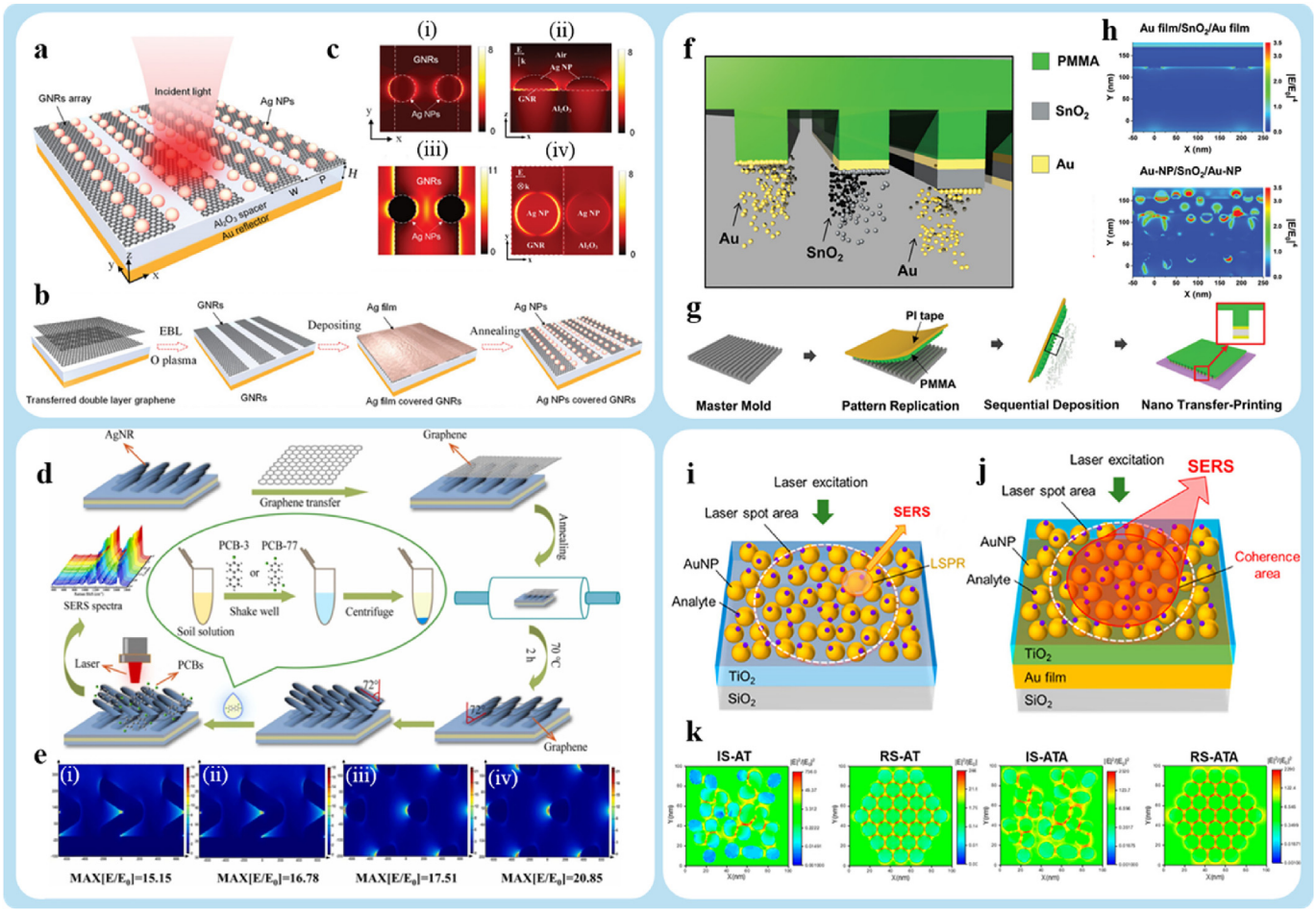

Fig. 4. (a) Experimental schematic of the Ag NPs modified GNRs SERS substrates, **(b)** procedures for fabricating the Ag NPs-modified GNRs SERS substrate, (c) Ag NPs' electric field distributions on the substrate with and without GNRs at the (i) x-z and (ii) x-y planes, as well as the matching distributions in the visible (iii) and infrared (iv) regions. Copyright 2021, Willey. (d) Ag NR@Graphene@Ag NR substrate preparation and SERS detection, (e) electric field distribution of (i) Ag NR@Ag NR, (ii) Ag NR@Graphene@Ag NR in the x-z plane and (iii) Ag NR@Ag NR and (iv) Ag NR@Graphene@Ag NR in the x-y plane. Copyright 2022, Elsevier. (f) Au DWF surface charge and field distribution images with (i) x-axis and (ii) y-axis light polarization directions, (g) detailed instructions for creating Au/SnO_2/Au nanowires, (h) simulation results for 3D-CMA with Au in the form of (i) thin film and (ii) NPs using the fourth power of electric field ($|E/E_0|^4$). Copyright 2021, Willey. (i) LSPR and (j) modal ultrastrong coupling, (k) cross-sectional near-field distributions. Copyright 2024, American Chemical Society.

demonstrates excellent uniformity and reproducibility. Similarly, Wang et al. developed modified Ag nanorods (Ag NR@Graphene@Ag NR) as SERS substrates with graphene as the interlayer to enhance the sensitivity of SERS detection for hydrophobic contaminants [66]. The graphene is layered with Ag NRs on both sides. The embedded graphene, with a significant electric field enhancement effect, supports the oblique V-shaped Ag NR structure in increasing the sensitivity of SERS detection (Fig. 4d). Numerous "hot spots" are created at the folds due to the annealing treatment, which shortens the nanogap between graphene and Ag NR. Finite-difference time-domain (FDTD) simulations confirm this (Fig. 4e). The Ag NR/Graphene/Ag NR substrate demonstrates excellent repeatability, with an EF of 1.6×10^{8}. Additionally, the substrate exhibits excellent sensitivity in detecting 4-chlorobiphenyl (PCB-3) and 3,3′,4,4′-tetrachlorobiphenyl (PCB-77). The detection limits were 1.72×10^{-10} M and 2.11×10^{-8} M, respectively. Principal component analysis (PCA) successfully identified the PCB mixture. This suggests that the Ag NR/Graphene/Ag NR substrate could play a crucial role in identifying and evaluating environmental mixtures of hydrophobic pollutants.

Compared to noble metals, semiconductor oxides offer low cost, advanced synthesis technology, rich diversity, and high chemical stability and biocompatibility, making them promising materials for SERS substrates. Han et al. developed a label-free chemo-resistive/SERS multimode sensor based on a system-assembled 3D cross-point multifunctional nanostructure (3D-CMA) (Fig. 4f) [67]. The substrate consists of two key components: optically and chemically active Au NPs and electroactive SnO_2 nanowires. SnO_2 nanowires decorated with an Au catalyst were fabricated using an advanced Solvent-Assisted Nano Transfer Printing (S-nTP) technique, forming a 3D nanostructure. The next phase in the process involves layer-by-layer deposition (Fig. 4g). The substrate can successfully selectively and quantitatively estimate the mixture gas composition below 100 ppm, with remarkable results even for mixtures of gaseous aromatic compounds (nitrobenzene and toluene) with very similar molecular structures. That is explained by the double-sided Au-NP/SnO_2/Au-NP nanogap hot spot that forms between the top and lower layers of the cross-point nanostructure (Fig. 4h). For gaseous analytes, the substrate exhibits a significant increase in the SERS signal under the influence of the EM mechanism. There is great potential for the benefits of multi-modal sensors in various gas detection applications, including biological diagnostics, environmental sensing, explosive detection, and food quality and safety monitoring. Similarly, Suganami et al. prepared a film comprising densely packed Au NPs (d-Au NPs)/TiO_2/Au film (d-ATA). An excellent SERS substrate with high sensitivity and spatial uniformity is achieved (Fig. 4i and j) [68]. The D-ATA substrate demonstrates the ultra-strong coupling of modes between the AuNPs and the LSPRs of the Fabry-Pérot nanocavity. Even without precise control over the form and arrangement of nano-AuNPs, the d-ATA substrate achieves higher sensitivity and more consistent signal intensity compared to the d-AuNP/TiO_2 substrate (Fig. 4k). Furthermore, 5.3×10^{-21} M R6G SERS experiments on this substrate showed a 3% spatial variation in signal intensity. These results suggest that the SERS signal originates from multiple quantum coherent plasmon particles under ultra-strong mode coupling.

MOFs are supramolecular structures formed via coordination bonds between metal ions or clusters and organic ligands. They exhibit remarkable functionalizability, a high specific surface area, active metal sites, a porous architecture, and tunable properties. [69]. MOFs, with their large specific surface area, are stabilized by π-π interactions, electrostatic forces, and hydrogen bonding. Metal NPs can be stabilized and supported within MOF structures. The MOFs' pores and interaction sites allow the SERS substrate to trap target molecules near the metal's EM zone [70]. However, the difficulty in controlling MOF nucleation and growth makes its site-selective deposition on metal nanocrystals challenging. Yang et al. developed a simple wet chemistry method for selectively depositing zeolitic imidazolate framework-8 (ZIF-8) on anisotropic Au nanobipyramids (NBPs) and nanorods [71]. ZIF-8 is selectively applied across the surface, including the ends and waist of the elongated Au nanocrystals (Fig. 5a). The Au NBPs were prepared through seed-mediated growth together with purification. Initially, CTAB (1 mM, 144 μL) was added to an aqueous solution of Hmim (1.32 M, 1 mL), followed by stirring for 10 min. Aqueous solutions of $Zn(NO_3)_2$ (24 mM, 1 mL), Au NBPs or NRs (longitudinal plasmon peak extinction adjusted to 5.0 at 0.5 cm optical path length, 1 mL), and CTAB (5 mM, 100 μL) were added progressively to the reaction solution. After stirring for 5 mis, the reaction solution was kept undisturbed at room temperature for 60 min. The resulting nanostructures were centrifuged twice and re-dispersed in methanol. The steric hindrance at the ends of the Au NBPs is smaller, which makes the ends effective nucleation sites for ZIF-8. ZIF-8 therefore prefers to grow at the ends of the Au NBPs. Using 4-ATP as a probe, the LOD of NBP-based nanostructures with end-deposited ZIF-8 is 10^{-8} M. This indicates that ZIF-8 can concentrate molecules in high-energy regions. FDTD simulations (Fig. 5b) were used to compare the local field intensity enhancement profiles of Au NBPs and similar nanostructures at their longitudinal plasmonic wavelengths. In conclusion, the electric field enhancement reaches its maximum. The electric field enhancement at both ends slightly increases with the deposition of ZIF-8. The NBP/End-ZIF nanostructure exhibits the highest electric field enhancement at both ends.

Due to their variety, well-established preparation methods, and low cost, organic polymers have been chosen as substrate materials for SERS systems [72–75]. Wang et al. developed a novel photoreduction polymerization technique to create conductive metal-polymer designs [76]. The Ag/polyaniline (PANI) nanocomposite was synthesized using maskless optical projection lithography (MOPL), which leverages multi-photon absorption and the LSPR effect (Fig. 5c). The SERS activity of R6G on an Ag/PANI nanocomposite square labyrinth achieved an LOD of 10^{-8} M. This is attributed to the EM produced by the strong LSPR effect of Ag NPs. As shown in Fig. 5d, the local electromagnetic field around the Ag NPs is enhanced due to the LSPR effect. At higher laser power, more "hot spots" are generated between the Ag NPs. Strong electromagnetic fields promote electron transport from the monomer to the plasma Ag NPs and enhance charge separation within the monomer. Similarly, Gullace et al. achieved layer-by-layer growth mediated by polyelectrolytes [77]. A reliable and label-free SERS substrate for electrostatic layer-by-layer assembly was created using metal NPs and polyelectrolytes. To optimize plasmonic properties, an intermediate layer of poly dimethyl diallyl ammonium chloride (PDDA) was used. Finally, the sensitivity of the best SERS platform was analyzed for the label-free detection of the antineoplastic drug tamoxifen (TAM) in tap water, realize the LOD of 3×10^{2} mg mL^{-1} and EF of 10^{6}.

In addition to the substrates mentioned above, there are reports of SERS substrates that do not fall into any specific category. Liu et al. developed a SERS substrate chip featuring a superhydrophobic surface [78]. The chip combines superhydrophobic surface treatment on a nanoporous substrate with 3D-assembled Au NPs for analyte enrichment in strong local fields (Fig. 5e). Notably, using a 1,2-bis(4-pyridyl)-ethylene molecule (BPE) and condensing the droplet into a 40 μL container, the LOD=10^{-9} M. FDTD simulations model the local field distribution of the substrate at a wavelength of 785 nm. Three distinct 3D-assembled substrates with pore sizes of 300 nm, 200 nm, and 90 nm were fabricated. The NP diameters and gap sizes were chosen to be in the ranges of 10–30 nm and 5–10 nm, respectively, based on the NP distribution and gap size analysis. Fig. 5f shows the electric field distribution for NPs with a 10 nm diameter and a 5 nm gap. The substrate with a 300 nm aperture exhibits a significantly stronger modeled local field near the edges of the Au NPs compared to the other two samples, indicating its excellent potential for enhanced SERS sensing. It is worth noting that the top Au layer enhances the coupling, thereby improving the sensing performance. Additionally, this chip can detect fentanyl at a concentration of 1 μg mL^{-1}. The 2.2% relative standard deviation (RSD) in inter-chip reproducibility highlights its potential for quantitative sensing of chemicals and drugs.

The crucial LSPR properties of noble metal particles enable the noble metal composite substrate to achieve exceptionally high EF. These

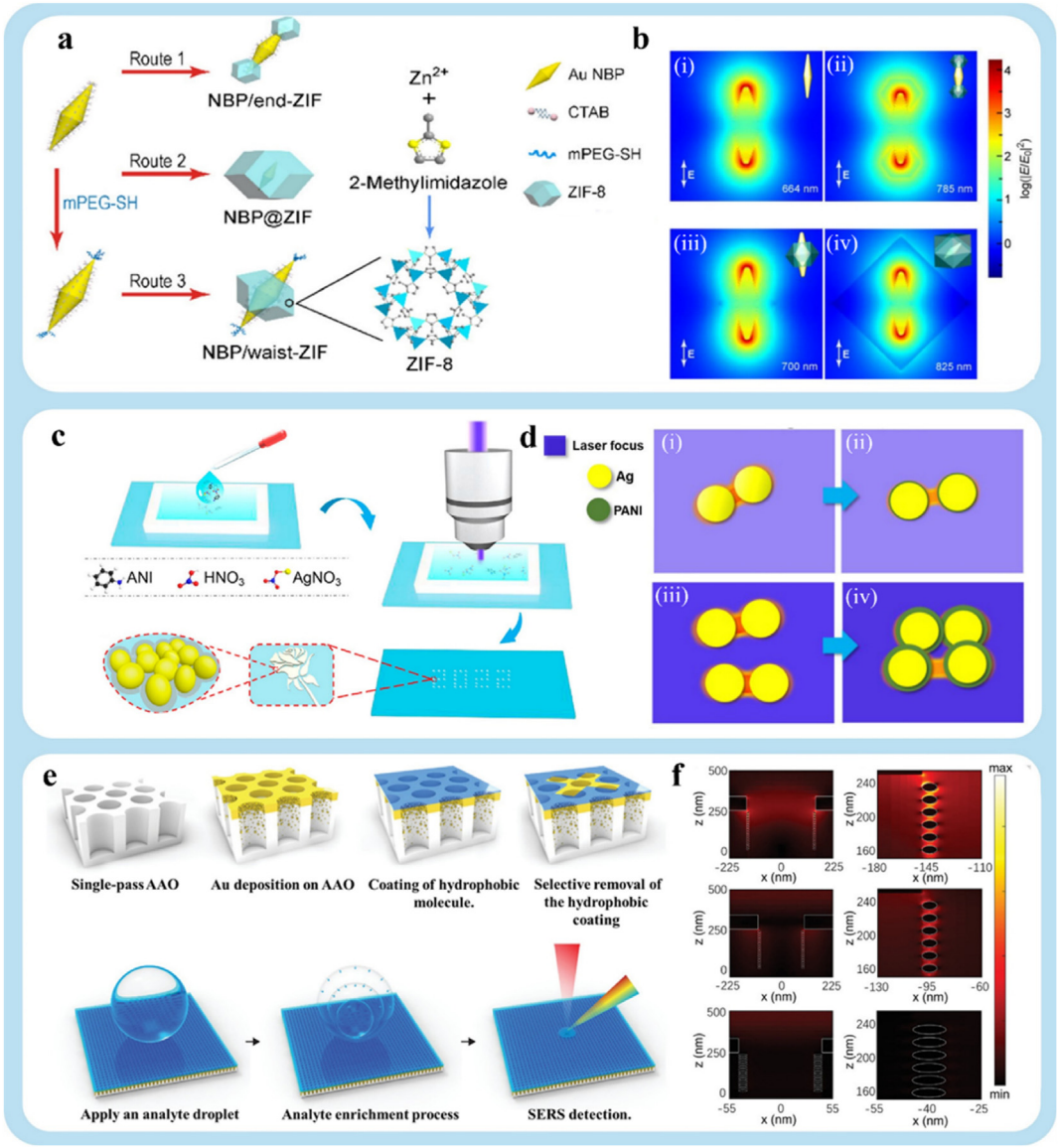

Fig. 5. (a) Diagram showing the paths for ZIF-8 selective deposition on Au NBPs, (b) FDTD simulation of the Au NBP and its derived nanostructures. (i) Au NBP, (ii) NBP/end-ZIF, (iii) NBP/waist-ZIF, (iv) NBP@ZIF. Copyright 2021, American Chemical Society. (c) Diagrammatic representation of the Ag/PANI nanocomposite production process, (d) diagram showing how the LSPR effect at varying laser intensities enhances the local electromagnetic field between Ag NPs. Copyright 2022, American Chemical Society. (e) Diagrammatic representation of the analyte enrichment approach and production process, (f) electric field distributions at 785 nm for samples with different pore sizes, 300 nm (top panel), 200 nm (middle panel), and 90 nm (bottom panel). Copyright 2022, Willey.

substrates are widely used across various industries, including biomedicine. Noble metal composite substrates are more cost-effective than conventional noble metal structured substrates, while still maintaining strong electromagnetic fields, thus broadening their potential applications. However, noble metal composite substrates still face several challenges, such as long storage times, low specificity, and high costs.

3.2. *SERS substrate of chemical enhancement mechanism*

Owing to its high LSPR, noble metal-based SERS substrates exhibit low LOD and strong EF. However, a key challenge in the practical use of noble metal-based substrates is their high fabrication cost, mainly due to expensive raw materials. Researchers have been focusing on developing noble metal-free substrates to lower the cost of SERS substrate fabrication. For instance, Tian et al. explored the development of SERS substrates incorporating various transition metals, such as cobalt, iron, nickel, platinum, and lead. The enhancement effect was marginal and has not attracted significant attention [79,80]. This is mainly because noble metals demonstrate strong SERS performance, while most other materials exhibit weak LSPR. The enhancement mechanism of many noble metal-free substrates is often based on CT effects through CM. To date, many noble metal-free SERS substrates have been developed, including metal oxides, carbon-based materials, semi-metallic 2D materials, TMDs, transition metal nitrides, and MXenes. Unlike noble metal substrates, noble metal-free substrates offer greater chemical stability, making them suitable for applications such as chemical analysis, biological imaging, diagnostics, and catalytic process monitoring [81,82]. Additionally, noble metal-free substrates provide significant cost advantages during production. Therefore, developing advanced noble metal-free SERS substrates can effectively address challenges such as cost and stability, making them more suitable for practical applications.

Carbon-based materials have been used to prepare SERS substrates [83]. Typically, they serve as a supporting matrix to load traditional noble metals (Au or Ag), enhancing Raman signals primarily via the EM effect [84]. Additionally, pure carbon materials can also serve as SERS substrates by leveraging the CM induced by CT between the carbon

materials and surface molecules. For example, Zhang et al. used a surfactant-free liquid-liquid interface-induced growth method to synthesize graphdiyne (GDY) hierarchical hollow microspheres (HHMSs) as SERS substrates, forming a self-supporting structure with an ultra-high specific surface area (Fig. 6a) [85]. GDY, a 2D carbon allotrope, possesses a direct band gap, excellent charge carrier mobility, and uniformly distributed pores. The graphitic acetylene hollow microspheres exhibited strong SERS properties, with an EF of 3.7×10^{7} for R6G and a LOD of 10^{-12} M. Experimental measurements and first-principles density functional theory (DFT) simulations confirmed that the substrate's SERS activity can be attributed to effective interfacial charge transfer (ICT) within the graphene-molecule system. The interactions between R6G molecules and GDY were carefully analyzed through first-principles simulations. The interaction between the R6G molecule and GDY was thoroughly assessed using first-principles simulations. First, the orbitals of GDY's sp-hybridized carbon atoms are more localized and exhibit more peaks in the projected density of states (PDOS) than the sp^2-hybridized carbon atoms in graphene, making the frontier PZ orbitals in GDY's co-adsorption system more similar to those in graphene. In the PDOS of GDY and R6G, the first peaks above the Fermi level are at 0.41 eV and 0.36 eV, respectively, while the initial peaks below the Fermi level are at −1.48 eV and −1.38 eV, respectively. In contrast to the graphene co-adsorption system, where the orbital level difference is > 0.71 eV, the difference in GDY is less than 0.10 eV. Second, first-principles calculations show that the adsorption energy of R6G on GDY is 2.24 eV, with 1.06 e of Bader charge transferred from the R6G molecule to GDY. The injected electrons are spread across the entire GDY surface, with charge buildup (highlighted in yellow) visible on the surface (Fig. 6b (i)). This leads to a stronger ICT effect between R6G and GDY. In the case of graphene, with an adsorption energy of 2.09 eV, 0.72 e is transferred from R6G to graphene, but most of the charge buildup and depletion occurs within R6G itself. There is minimal charge buildup on the graphene surface (Fig. 6b (ii)), leading to a significantly weaker SERS effect in graphene compared to GDY. Graphene exhibits a significantly lower SERS effect than GDY, despite its superior fluorescence quenching properties. Ultimately, the PDOS shows that the magnetic moment of the R6G molecule vanishes from 1.0 μB/molecule upon adsorption by GDY. In contrast, the magnetic moment of R6G remains unchanged when adsorbed on graphene. Significantly, R6G's unpaired electrons transfer to GDY, generating a pronounced ICT effect crucial for SERS. The multiple peaks in the PDOS indicate that GDY's sp-hybridized carbon atoms are key for enhancing the ICT effect between GDY and R6G. The fully sp^2-hybridized PZ orbitals in graphene are delocalized, making it difficult to generate an ICT effect with R6G, whereas the sp-hybridized carbon

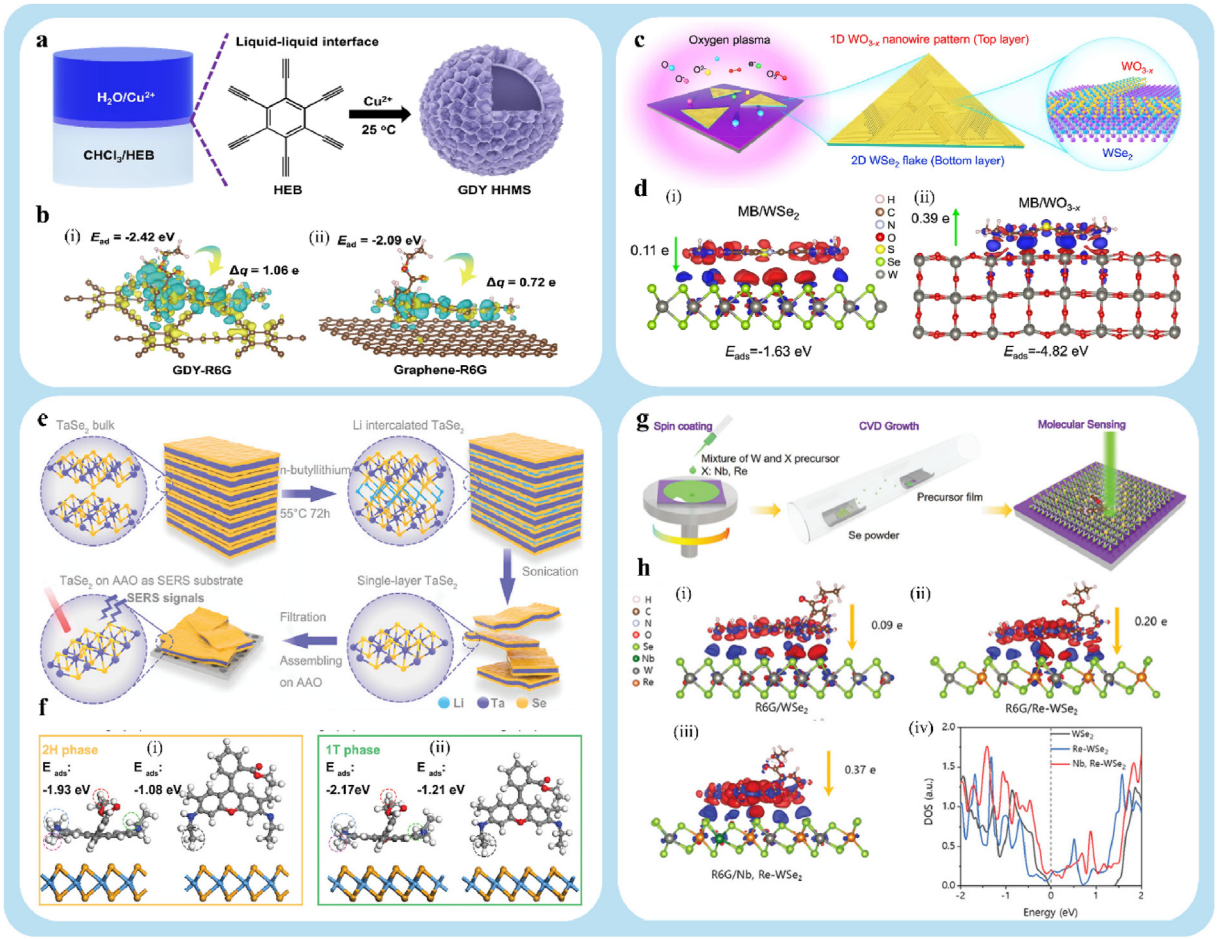

Fig. 6. (a) Diagrammatic representation of GDY HHMS synthesis, (b) charge density difference of R6G adsorbing on (i) GDY and (ii) graphene, where the yellow and cyan color marks the regions of charge accumulation and depletion, respectively. Copyright 2023, Springer Nature. (c) Diagrammatic representation of the synthesis of 1D oriented WO_{3-x} nanowires from 2D WSe_2 flake, (d) charge density differences of MB molecules on the (i) WSe_2 and (ii) WO_{3-x}, where the blue (red) corresponds to the charge accumulation (depletion). Copyright 2023, Springer Nature. (e) Diagrammatic representation of the $TaSe_2$ nanosheet production process, (f) DFT calculation results for the R6G molecules adsorbed on the 2H phase (i) and 1T phase (ii) $TaSe_2$ with parallel and perpendicular configurations. Copyright 2022, Willey. (g) Schematic illustration of the growth of pristine and heteroatom (X)-doped monolayer WSe_2 by chemical vapor deposition route (X represents Nb or Re), (h) charge density differences of R6G molecules on WSe_2 (i), Re-WSe_2 (ii), and Nb, Re-WSe_2 (iii), where the blue (red) corresponds to the charge accumulation (depletion). (iv) DOS of WSe_2, Re-WSe_2, and Nb, Re-WSe_2. Copyright 2021, Willey.

atoms in GDY provide localized flatness that better matches R6G's molecular orbitals. As a result, GDY demonstrates a much stronger SERS effect compared to graphene. The charge density difference of R6G adsorbed on graphene and GDY is shown in Fig. 6b (i) and (ii), with charge buildup and depletion represented by yellow and cyan, respectively.

SERS substrates have been fabricated using transition metal dichalcogenides (TMDCs) due to their tunable electronic structure, high chemical stability, and atomically flat surfaces [86]. Owing to their unique electronic and physicochemical properties, 2D TMDCs are combined with other nanostructures to form mixed-dimensional heterostructures, such as 2D-1D, which can further enhance SERS performance [87]. Moreover, the interaction between these hybrid materials and analytes remains largely unclear and requires time-resolved spectroscopy to be elucidated for ultrasensitive molecular sensing. Lv et al. achieved a facile synthesis of mixed-dimensional heterostructures through oxygen plasma treatment of 2D materials, fabricating a 1D/2D WO_{3-x}/WSe_2 heterostructure with good controllability and reproducibility (Fig. 6c) [88]. The 1D WO_{3-x} nanowire pattern is laterally aligned along the threefold symmetry direction of the 2D WSe_2. The WO_{3-x}/WSe_2 heterostructure exhibits high molecular sensitivity even in mixed solutions, with a LOD of 5×10^{-11} M and an EF of 5×10^{18} for methylene blue (MB). Fig. 6d (i) (ii) shows that the adsorption energy of MB molecules on the WO_{3-x} substrate is −4.82 eV, significantly stronger than the adsorption energy on the WSe_2 substrate (−1.63 eV). Additionally, an efficient CT of 0.39 e between the MB molecule and the WO_{3-x} substrate induces a stronger interface dipole for MB/WO_{3-x} compared to MB/WSe_2 (0.11 e). Thus, the ultrasensitive SERS capability of the heterostructure is attributed to the efficient CT enabled by the unique structure of the WO_{3-x} nanowires and the heterostructure itself.

Due to their strong interaction with analytes, atomically flat surface, and high density of states (DOS) near the Fermi level, half-metallic 2D materials with zero bandgap are ideal candidates for SERS substrates [89]. As a typical semimetallic 2D material, $TaSe_2$ exhibits charge density waves (CDW), superconductivity, and a tunable electronic structure, making it a promising candidate for SERS substrates and Raman biosensors [90–92]. Ge et al. prepared atomically thin $TaSe_2$ samples using the method shown in Fig. 6e [93]. The sample consists of two to three layers of $TaSe_2$ nanosheets with a diameter of 2.5 cm, used as a SERS substrate for various analyses. The $TaSe_2$ substrate exhibits excellent SERS performance, with a LOD of 10^{-10} M for R6G. Spectral analysis and DFT revealed the underlying mechanism behind the excellent SERS performance of $TaSe_2$. The high adsorption energy and large number of filled electrons near the Fermi level play a crucial role in the CM mechanism. Experimental results and DFT calculations reveal a strong interaction between $TaSe_2$ nanosheets and Raman probes. Additionally, the higher Fermi level of $TaSe_2$ accelerates electron migration to the HOMO of the SERS probe, increasing the probability of electron transfer. The DFT calculation results are shown in Fig. 6f (i) and (ii). The adsorption energy (EAD) of R6G molecules on 1T and 2H phase $TaSe_2$ layers was calculated for both parallel and perpendicular configurations. The parallel configuration is the most stable, with adsorption energies of 1.93 and 2.17 eV for the 2H and 1T phases of $TaSe_2$, respectively. In contrast, Eads values of −1.08 and −1.21 eV for the perpendicular configuration are less favorable than those for the parallel configuration, indicating a less stable state.

SERS substrates based on 2D metallic/half-metal TMDCs have been investigated due to their chemically active surfaces and high DOS at the Fermi level, which enhance Raman scattering cross-sections [94]. However, 2D metallic and semimetallic TMDCs are generally environmentally unstable. Therefore, using an in-situ replacement doping method, Lv et al. synthesized heavily doped WSe_2 (Re-WSe_2) substrates with varying doping levels [95]. As shown in Fig. 6g, the 1T″ phase of the $ReSe_2$ lattice is inherited by the Re-WSe_2 alloy when the rare earth concentration reaches approximately 50%. Nb atoms are added to further modify the electronic structure of the 1T″ Re-WSe_2 alloy. The synthesized 1T″ Nb, Re-WSe_2 substrate exhibits exceptional SERS performance, with a LOD of 5×10^{-15} M and an EF of 2×10^{9}. Notably, the substrate also exhibits excellent stability and specific detection capabilities in mixed molecular solutions, making it suitable for practical applications. DFT calculations were performed for WSe_2, Re-WSe_2, and Nb, Re-WSe_2 (Fig. 6h (i) (ii) (iii)). The R6G/WSe_2, R6G/Re-WSe_2, and R6G/Nb/Re-WSe_2 systems had adsorption energies of −1.94, −1.98, and −2.10 eV, respectively. This indicates that the R6G/Nb and Re-WSe_2 systems exhibit stronger interactions compared to other systems. Additionally, charge density difference and CT studies show that approximately 0.09, 0.20, and 0.37 e were transferred from R6G molecules to WSe_2, Re-WSe_2, and Nb, Re-WSe_2, respectively. The interface dipole generated between R6G and Nb in Re-WSe_2 is the strongest. Nb, Re-WSe_2 exhibits better SERS performance than WSe_2 and Re-WSe_2 due to its higher adsorption energy and more efficient CT of the probe molecules. WSe_2 has a valence band maximum (VBM) of −5.10 eV and a conduction band minimum (CBM) of −3.56 eV. After the addition of Re and Nb atoms to WSe_2, the band gaps of Re-WSe_2 and Nb, Re-WSe_2 disappear. Re-WSe_2 has Fermi levels of −4.73 and −5.02 eV, respectively. The varying electronic structures of the substrates influence their DOS at the Fermi level. Nb and Re-WSe_2 show higher DOS than pristine WSe_2 and Re-WSe_2, as illustrated by the DOS at the Fermi level in Fig. 6h (iv). This is beneficial for enhancing SERS performance. Overall, 1T″ Nb, Re-WSe_2 demonstrates more sensitive SERS performance compared to WSe_2 and Re-WSe_2, based on its adsorption energy, CT, and DOS at the Fermi level.

Borocarbonitride (BCN), a 2D conjugated compound composed of boron, carbon, and nitrogen, has garnered significant attention for its potential in energy storage and conversion applications [96]. Moreover, the composition of BCN can be easily modified to effectively tune its band structure. This property suggests that BCN could serve as an excellent substrate for SERS. Liang et al. developed a 2D BCN substrate with outstanding SERS performance through a structural engineering approach (Fig. 7a) [97]. In the absence of PEG, the final sample achieved a LOD of 10^{-8} M for crystal violet (CV). Additionally, BCN exhibits excellent thermal and chemical stability, which is crucial for its practical applications in industrial environments. Specifically, the CB energy level of BCN is aligned with the LUMO of the R6G molecule. The energy from vibrational coupling resonance is extracted through the Herzberg-Teller coupling mechanism. (Fig. 6b).

Molybdenum disulfide (MoS_2) has emerged as a promising non-precious material for SERS substrates. However, the CT rate is limited due to the catalytic inactivity of many MoS_2 basal planes. Its performance is further hindered by the high overpotential in hydrogen evolution reactions (HER) and the scarcity of active sites [98]. Therefore, increasing the number of active sites and modifying the surface electronic structure of MoS_2 are crucial for enhancing the efficiency of MoS_2-based photoelectrodes. Zhang et al. utilized a one-step hydrothermal process to incorporate ruthenium (Ru), accelerating CT and generating additional active sites [99]. They synthesized O-co-doped MoS_2 substrate material, labeled as $MSOR_x$. MoS_2 forms uniform nanoflowers (NFs) with a diameter of approximately 1 μm, as shown in Fig. 7c(i) and (iii). $MSOR_1$ NFs measure approximately 0.8 μm in diameter and consist of stacked sheets with high edge site exposure. The Ru and O co-doping induces more defects, weakening the interlayer connections and resulting in smaller MoS_2 NFs with thinner petals. TEM images of MoS_2 and $MSOR_1$ after 10 min of sonication are depicted in Fig. 7c(ii) and (iv). The flower-like nanosphere morphology is preserved. Conversely, the intrinsic structure of MoS_2 remains unchanged despite Ru and O co-doping. Notably, $MSOR_1$ exhibits the most vertically aligned and well-distributed structure. This unique structure exposes more active sites, enhancing the efficiency of both SERS and HER. Fig. 7d(i)(ii) illustrates the calculated electronic structures of Ru sites with and without OH* adsorption. It was found that the electronic structure around the Ru site was reconstructed due to the newly established interaction between Ru and O atoms. As a result, $MSOR_1$ demonstrates remarkable SERS performance, with an EF of 1.7×10^{6} and a LOD of 10^{-10} M for bilirubin.

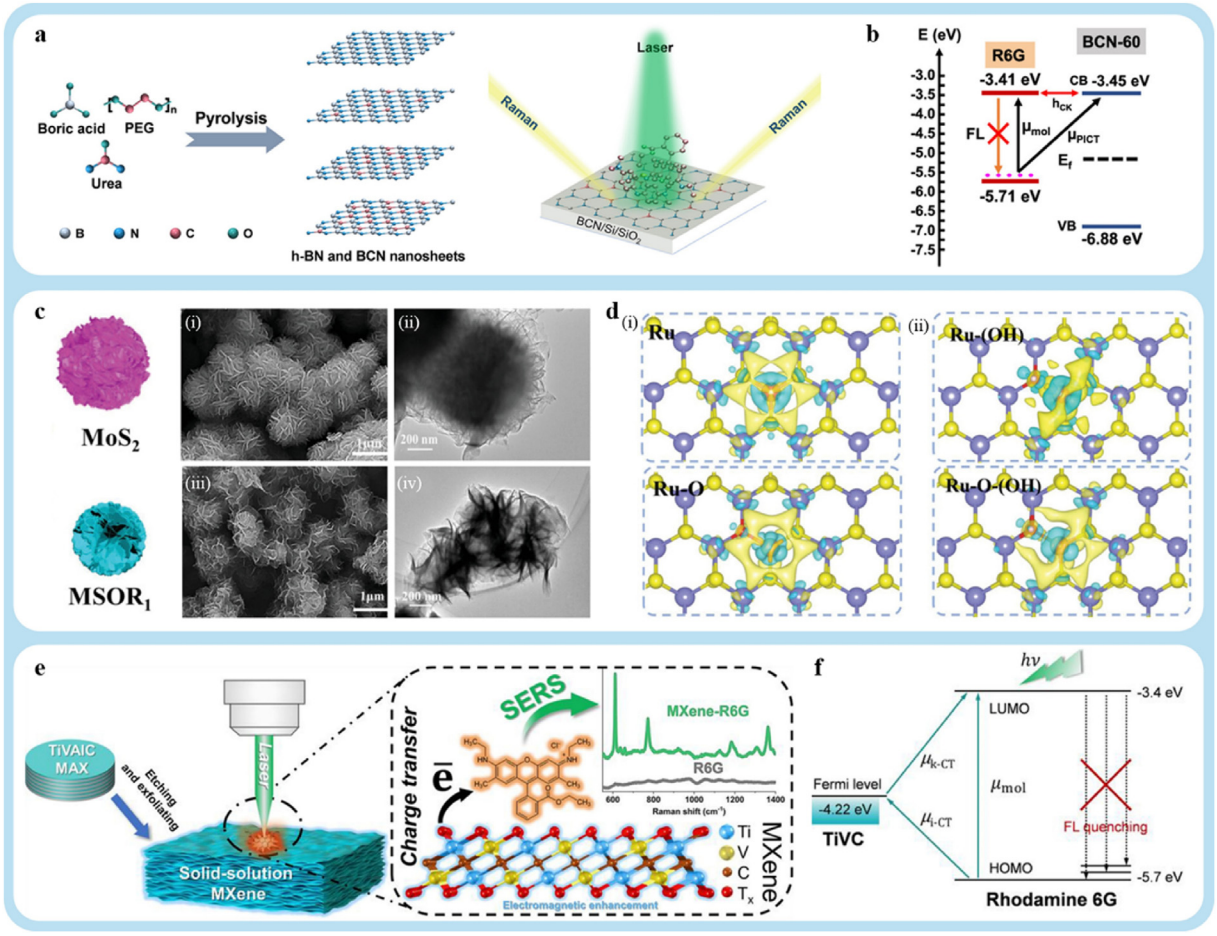

Fig. 7. (a) Diagrammatic representation of h-BN and BCN nanosheet production, (b) diagrammatic representation of the CT mechanism and energy band diagrams between R6G and BCN-60. Copyright 2022, American Chemical Society. (c) SEM image of MoS_2 NFs (i) and $MSOR_1$ NFs (iii), TEM image of MoS_2 NFs (ii) and $MSOR_1$ NFs (iv), (d) charge density difference of Ru and Ru-O sites with/without OH adsorption, the blue and yellow regions denote electronic depletion and accumulation, respectively. Copyright 2023, Willey. (e) Schematic of the 2D TiVC solid-solution MXene substrate and its application in SERS, (f) schematic illustration of the PICT process between R6G and TiVC. Copyright 2022, American Chemical Society.

The addition of Ru and O resulted in excellent HER and SERS activity, broad pH range universality, and long-term stability.

MXenes are 2D transition metal carbides/nitrides utilized in the fabrication of SERS substrates. MXenes exhibit excellent conductivity, hydrophilicity, biocompatibility, tunable electronic structure, and other desirable properties [100]. Another advantage of MXenes is their low manufacturing cost. He et al. reported that chemical etching can be performed in a single step [101]. Fig. 7e illustrates the large-scale production of highly crystalline TiVC nanosheet layers. The flexible TiVC film developed as a SERS substrate demonstrated excellent SERS performance. The detection limit for R6G reached the femtomole level, with an EF of 3.27×10^{12}. TiVC and the analyte separate more readily in the complex due to the high density of states near TiVC's Fermi level and the strong interaction between them. A significant enhancement in Raman signal is observed due to intermolecular CT resonance. Additionally, the enhanced CM-based selectivity of TiVC substrates was confirmed using various additional probe molecules in SERS detection. Fig. 7f shows the energy level distribution and possible PICT pathways in the TiVC-R6G complex. These include CT transitions from the molecular HOMO to the TiVC Fermi level (μI-CT, 1.48 eV), from the Fermi level to the molecular LUMO (μK-CT, 0.82 eV), and the molecular transition within R6G from HOMO to LUMO (μmol, 2.3 eV). Consequently, the polarization tensor of the R6G molecule is significantly enhanced by molecular and charge-transfer resonances induced by PICT, in accordance with the Herzberg-Teller vibrational coupling theory.

When comparing noble metal-based substrates, where the EM is the primary enhancement, with noble metal-free substrates, it is evident that the CM predominantly contributes to the latter's enhancement. The practical application of noble metal-free substrates in trace analysis is constrained by their relatively modest enhancement. Additionally, unlike noble metal-based substrates, there is no unified enhancement theory for noble metal-free substrates. As discussed in Section 2.2, the CT effect in the substrate-molecule complex can follow multiple possible pathways. Several noble metal-free SERS substrates can engage in one or more pathways simultaneously. Therefore, fabricating and utilizing noble metal-free substrates will become more straightforward if the primary role of the CT pathway in SERS amplification is identified and a unified understanding of it is developed as soon as possible.

3.3. SERS substrate of synchronous enhancement

3.3.1. EM and CM synergy enhancement

Because noble metal particles exhibit strong LSPR characteristics, EM is typically the primary mechanism used in noble metal composite substrates to achieve outstanding SERS performance. The matrix material often serves as a carrier for noble metal particles, providing active sites and regulating the distance between them, which significantly enhances the substrate's SERS performance. Additionally, when specific materials are used as the matrix, probe molecules can induce CT, leading to CM. This synergistic effect results in excellent SERS performance [102].

Section 2.2 covers the preparation of substrates without noble metals. These materials can also be combined with noble metal particles to synergistically enhance both EM and CM effects. This section discusses the fabrication of substrates with partial cooperative enhancement and the corresponding enhancement process.

TMNs are a promising class of materials for applications in optoelectronic sensing, energy storage, catalysis, and superconductors. The nitride anion (N^{3-}) provides unique electrical and bonding characteristics, which contribute to TMNs' exceptional physical and chemical properties [103]. However, TMNs, especially ultrafine tungsten nitride (WN) nanostructures in ambient conditions, exhibit low thermodynamic stability and require an extraordinarily high reaction barrier during synthesis [104]. As a result, ultrafine tungsten nitride nanostructures have been synthesized using traditional methods such as chemical solution growth and mixed solvent thermal implantation, although these methods result in limited production. Liu et al. synthesized highly crystalline tungsten nitride (W_2N, WN, W_3N_4, W_2N_3) nanocrystals, as shown in Fig. 8a [105]. These nanocrystals were immobilized in a fragile carbon layer, forming a hybrid nanoribbon structure. The hybrid WN/C nanoribbon demonstrates substantial LSPR and SERS effects, with an EF of 6.5×10^8 and a LOD of 10^{-12} M for Bisphenol-A (BPA). Moreover, the substrate exhibits exceptional resistance to radiation, oxidation, and corrosion—qualities not typically found in traditional noble metal substrates. The significant SERS performance of the substrate can be attributed to the synergistic effects of CM and EM. Due to their structural roughness, these carbon-coated nanoribbons are more likely to generate strong electromagnetic "hot spots" between closely spaced protrusions. As shown in Fig. 8b (i), the hot spot intensity near the nanoparticle gap is significantly stronger, with E/E_0 reaching a maximum value of 29.5. The FDTD data demonstrate the EM of densely arranged WN NPs.

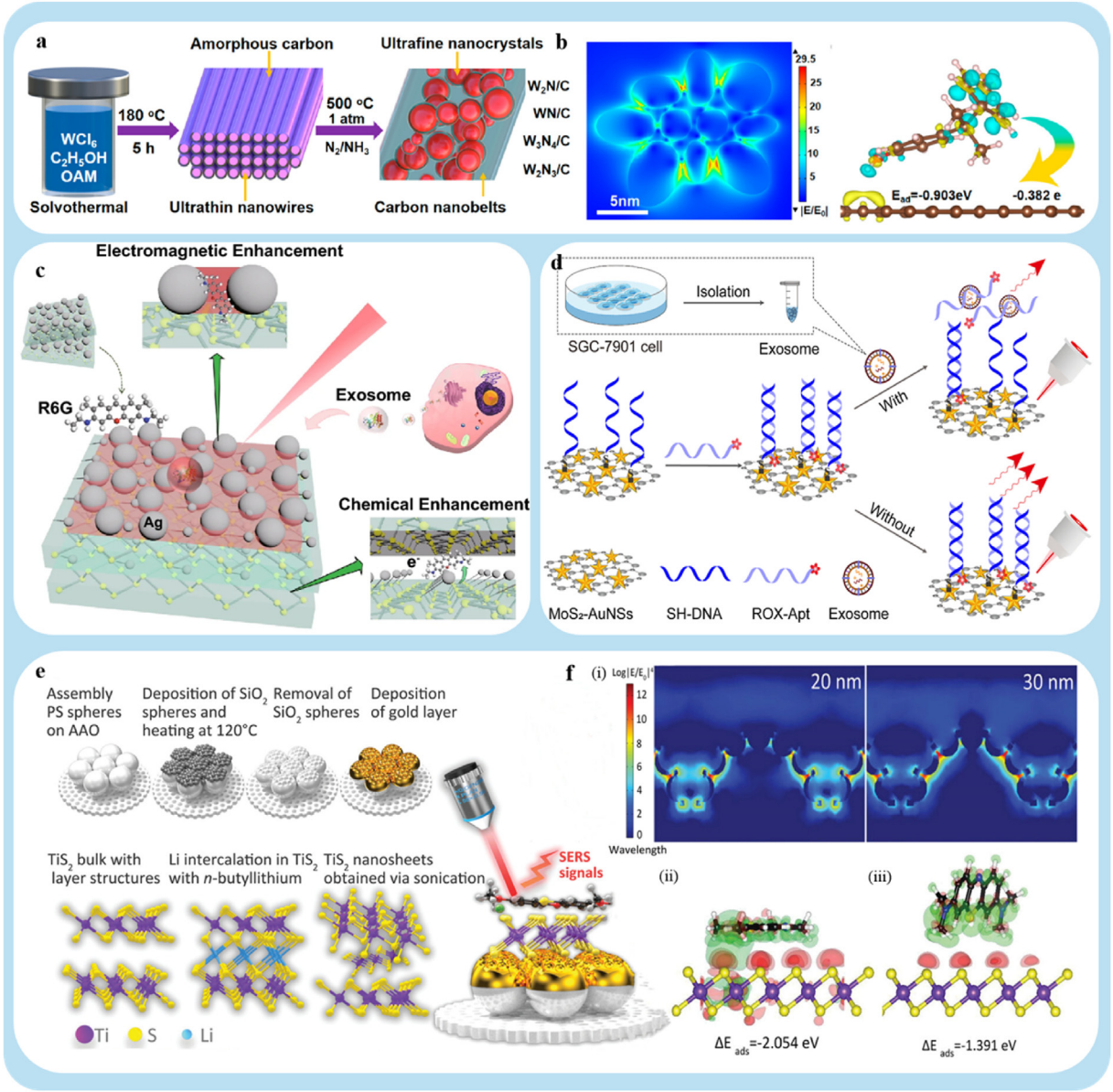

Fig. 8. (a) Diagrammatic representation of the WN/C hybrid nanobelt synthesis, (b) SERS properties and enhanced mechanism of the WN/C nanobelts. (i) Hot spots simulated by FDTD. (ii) Side views of the electron density differences BPA adsorbed on N-doped carbon nanobelts. Copyright 2022, American Chemical Society. (c) Schematic diagram of the synthesis and application of Ag/BP-NS SERS sensor. Copyright 2022, Springer Nature. (d) Fabrication of MoS_2-based aptasensor for exosome detection. Copyright 2022, Elsevier. (e) Fabrication process of SERS substrate, including deposition of Au layer on the rough surface of assembled PS spheres and exfoliation of TiS_2 nanosheets, (f) (i) electric field distributions of CGA substrates with different Au layer thicknesses under 633 nm excitation, (ii) (iii) DFT-calculated charge density difference of MB adsorbed on TiS_2 single layer. Copyright 2023, Willey.

Simultaneously, the CT effect induces a CM effect in porous carbon nanowires [52]. DFT simulations show that the adsorption EAD between the N-doped carbon shell and the bisphenol A (BPA) molecule is as high as 0.903 eV, indicating a strong interfacial interaction (Fig. 6b (ii)). Additionally, 0.382 eV was transferred from the N-doped carbon shell to the BPA molecule, according to the molecular charge analysis using Bader atom methods. The BPA/N-doped carbon shell exhibits a stronger coupling effect, as evidenced by the high adsorption energy and significant CT. As a result, the vibrational behavior of analyte molecules may be significantly enhanced. When EM and CM work synergistically, the substrate demonstrates high SERS performance.

BP nanosheets are 2D materials with high carrier mobility, strong photoelectric activity, a large specific surface area, good near-infrared absorption, and excellent photothermal conversion [106]. Research shows that the inherent SERS EF of BP is minimal. Kundu et al. used low-power laser irradiation to construct nanocavity arrays on BP nanosheets, achieving a LOD of 10 nM for R6G [107]. Therefore, to further enhance the SERS sensitivity of BP and its hybrid nanomaterials, novel nanostructures that synergistically combine EM and CM enhancements are needed. Lin et al. used a novel photoreduction technique to create a nanojunction with Ag NPs embedded in multilayer black phosphorus nanosheets (Ag/BP-NS), forming a SERS substrate (see Fig. 8c) [108]. Numerous ultra-small Ag NPs (3–5 nm) are firmly adhered to the BP surface and embedded within it, along with larger aggregated Ag NPs (~50 nm) that act as "hot spots" for EM. This structure facilitates a strong CM effect and opens a PICT channel between Ag, BP, and R6G. The substrate demonstrates outstanding SERS performance for R6G, with a LOD of 10^{-20} M. Due to the synergistic enhancement of EM and CM, the substrate shows exceptional SERS performance with an EF of 10^{11}. When exposed to excitation light, BP nanosheets generate a large number of photogenerated electrons, enhancing the efficiency of Ag nanoparticle reduction. Multiple Ag NPs produce strong electromagnetic fields, which can enhance the signal by approximately. Additionally, the heterostructure's high carrier mobility facilitates both CM and photoactivity.

Due to their large surface area, ease of functionalization, and high loading capacity for (bio) compounds, MoS_2 nanosheets are used as SERS-active substrates [109]. Strong SERS performance is achieved when noble metal particles attach to the large specific surface area of MoS_2. For example, Pan et al. developed a SERS substrate based on MoS_2 nanocomposites modified with Au nanostars (MoS_2-Au NSs) (Fig. 8d) [110]. ROX-labeled aptamers (ROX-Apt) were assembled on the surface of MoS_2-Au NSs to serve as recognition probes for specific binding. The substrate exhibits remarkable SERS performance due to the synergistic enhancement of EM effects from Au NSs and CM effects from MoS_2 nanosheets. The substrate has a LOD of 17 particles·μL^{-1} and can detect particles in the range of 55 to 5.5×10^5 particles·μL^{-1}.

$TaSe_2$ has shown outstanding SERS performance as a 2D semimetallic material, owing to its higher DOS compared to graphene and MoS_2. The CT probability depends linearly on the DOS near the Fermi level, according to the Fermi golden rule. The CT process relies primarily on fast electron transfer from the semimetallic 2D material to the analyte, which significantly enhances SERS performance. Ge et al. used a 2D TiS_2 nanosheet-coated concave Au array to fabricate a SERS substrate (Fig. 8e) [111]. This setup combines CT resonance with LSPR. The substrate exhibits exceptional SERS performance, with an EF of 2.1×10^9 and a LOD of 10^{-13} M for MB. The exfoliated 2D TiS_2 nanosheets, with semimetallic properties, accelerate CT to the test analyte, resulting in significant CM enhancement. Additionally, the concave Au array beneath the thin TiS_2 nanosheet, combined with the LSPR effect, provides substantial electromagnetic amplification (Fig. 8f). Silicon nanospheres were assembled on top of larger polystyrene nanospheres, etched, and coated with an Au layer to create the concave Au arrays.

MXene nanosheets have a highly anisotropic, sheet-like geometry. The monolayer nanosheets are conformally deposited onto noble metal nanoparticle SERS substrates and easily deform to match the underlying surface texture. Due to their flexibility compared to other 2D materials, monolayer MXene nanosheets can conform more easily and flexibly to the underlying SERS substrate [112]. This allows the target analyte to bind sufficiently close to the hot spot core (i.e., within <5 nm). MXene nanosheets significantly EM effects when in contact with Au NPs, improving LSPR on the substrate. Additionally, the abundant surface functional groups on MXene nanosheets allow for further cation modification in chemical bonding, enabling various on-demand sensing applications [113]. Consequently, MXene is frequently used as a deposited layer for tuning the Fermi level of SERS substrates. Yoo et al. developed a technique using this information to assemble ultrasensitive SERS NPs on a 2D surface, where Au was conformally coated with a few atomic layers of MXene (Fig. 9a) [114]. The MXene layer effectively promotes CT by positioning the substrate's Fermi level between the analyte's HOMO and LUMO levels. Additionally, the wrinkled surface structure formed by the conformal coverage of the MXene layer on the Au NP assembly helps trap the analyte within the hot spot between NPs, boosting the EM effect (Fig. 9b and c). With an analytical EF of up to 1.6×10^{10} for Rhodamine B (RhB) the proposed SERS platform demonstrates an innovative structural design using MXene layer deposition. Furthermore, Cr (VI) was detected at a low limit of 13 ng L^{-1}. This SERS platform can be expanded and generalized for the quantitative detection of a wide range of analytes, including biologically and environmentally significant compounds.

GaN has been utilized to create CM-based SERS substrates, which offer improved chemical stability and consistent SERS signals [115]. However, Substrates with CM processes are often not significantly enhanced. Although GaN and Ag have been used to create hybrid SERS substrates, this has only resulted in a restricted EF of 10^5 for semiconductor-based SERS [116]. In addition, compared to the SEF of metals, most hybrid SERS substrates show somewhat greater or even lower EF values. That severely restricts the extensive use of hybrid systems in SERS analysis. This indicates that adding a plasmonic metal coating to a semiconductor does not dramatically increase its SERS performance, necessitating more intricate design guidelines. Based on this, a hybrid SERS substrate with Ag serving as the plasmonic structure and GaN serving as the CT enhancement center was proposed by Lee et al. [117]. Ag nanowires may be conformally printed onto GaN nanopillars (AoG) to provide a very homogeneous and sensitive SERS substrate (Fig. 9d). Therefore, considerable SERS performance with a substrate EF of 1.4×10^{11} at 10 fM may be achieved for the R6G molecule with the slightest spot variation. A schematic performance-level diagram of R6G on an AoG substrate is shown in Fig. 9e. R6G has the LUMO level of 3.4 eV and the HOMO level of 5.7 eV. The excitation of electrons from the HOMO to the LUMO level of R6G by the Raman excitation laser initiates the CT process. Moreover, the photon energy can activate the trapped electrons in the GaN defect states. These electrons are subsequently injected into Ag's Fermi level after being moved to the conduction band of GaN. Thus, the CT process modifies the polarizability of the R6G molecule and increases the Raman intensity [118]. Thus, the GaN-Ag hybrid structure would be a sound system for EM and CM constructive interaction to maximize the SERS signal, where the CT process may borrow the strength of the EM-enhanced Raman scattering process. Furthermore, identifying dangerous antibiotics in aqueous solutions showed the ability to quantify and multiplex without surface treatment. By building intricate metal-semiconductor frameworks, this study paves the door for fabricating susceptible SERS substrates.

LDHs are a novel category of materials with two dimensions. Researchers have been interested in these materials' physical and chemical features because of their easy synthesis, variety of structures, plenty of adsorption sites, chemical composition, tunable morphological structure, high specific surface area, and distinctive physical characteristics [119, 120]. The sharp tip of its 3D hierarchical structure offers a practical CT pathway for CM [121]. Additionally, they can synthesize well-dispersed, dense Ag NPs that can provide rich hot spots for EM. Based on this, Kokulnathan et al. created and manufactured semiconductor cobalt-iron layered double hydroxides (CoFe-LDHs) and noble metal Ag nanospheres (Ag NSs) based on plasma for the detection of 4-nitrophenol (4-NP)

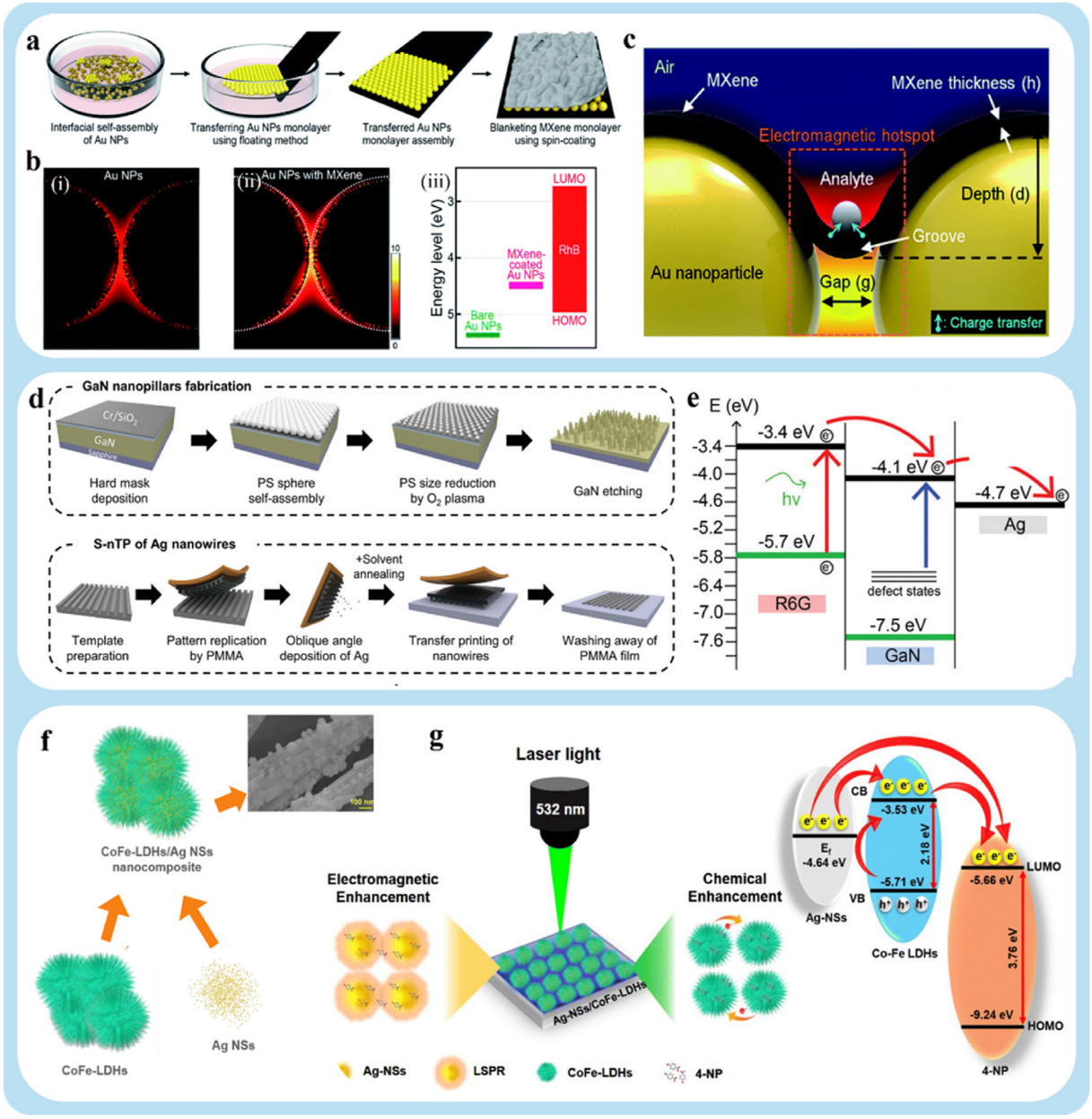

Fig. 9. (a) Schematic illustrations of the procedure to fabricate the MXene-coated Au NP assembly, (b) computational simulation results for the distribution of the absolute value of the electric field (i) near bare Au NPs and (ii) near MXene-coated Au NPs, (iii) energy diagram of experimentally measured work functions of bare Au NPs and MXene-coated Au NP assemblies, and HOMO/LUMO levels of RhB, (c) diagrammatic representations of the SERS platform with the analyte molecule situated in the deflected MXene monolayer's groove. Copyright 2022, the Royal Society of Chemistry. (d) Fabrication process of Ag NWs on GaN NPs (AoG) structure, (e) diagrammatic representation of R6G's energy level on the AoG structure in relation to the vacuum level. Copyright 2021, Willey. (f) Preparation of the Ag-NSs/CoFe-LDHs nanocomposite, (g) SERS mechanisms and CT process between the Ag-NSs/CoFe-LDHs nanocomposite and the 4-NP molecule. Copyright 2024, the Royal Society of Chemistry.

(Fig. 9f) [122]. The hydrothermal process, physical mixing, and chemical reduction were used to create Ag-NSs/CoFe-LDH nanocomposites. For 4-NP detection, the Ag-NSs/CoFe-LDHs nanocomposite exhibits a superior SERS response. Its high EF is 5.65×10^{11}, and its LOD is 2.36×10^{-14} M. The combined action of the CT mechanism from CoFe-LDHs and the electromagnetic process from Ag NSs is responsible for the enormous Raman signal increase (Fig. 9g). The Ag-NSs/CoFe-LDHs SERS substrate has excellent long-term stability, high repeatability, and homogeneity. Furthermore, with an anticipated recovery rate of 93%–95%, the Ag-NSs/CoFe-LDHs SERS substrate exhibits strong detection capability for actual environmental samples. This work will aid in developing S with plasmonic action and interfacial CT in metal/semiconductor nanocomposites. The ERS platform creates an additional path.

The Herzberg-Teller coupling theory states that linking the EM and CT effects may further enhance SERS performance, provided that plasmon-free substrates are reasonably combined. Generally speaking, the loading of noble metal particles and the selection of matrix materials determine how well the synergistic enhancing processes of CM and EM are realized. The noble metal particles' shape, loading, and spacing may be adjusted to enhance the substrate's EM efficiency. By choosing the suitable matrix material, excitation wavelength, and other factors, as well as the right doping plan, the CM of the substrate may be efficiently increased. The substrate's detection sensitivity, accuracy, enhancement effect, and similar properties may be successfully increased under the two

methods' synergistic influence. Its superior SERS performance can increase the use of SERS in various industries, including food safety, environmental monitoring, and biomedicine.

3.3.2. EM and enrichment strategy synergy enhancement

SERS substrate using evenly distributed, densely packed, ultrasensitive SERS sites ("hot spots") as the enhancing mechanism. The probe molecule's Raman signal will be significantly amplified when it is situated near the "hot spot." Because of the long-range nature of electromagnetic field enhancement, molecules can produce stronger Raman signals even without direct adsorption onto a metal surface. However, the intensity decreases rapidly as one gets farther away from the hot area. Different enrichment procedures may enrich the probe molecules in the "hot spot area to effectively increase the enhancing impact of the substrate." Furthermore, the enrichment technique may accomplish SERS detection of several tiny cross-sections or weakly adsorbed molecules. Weakly adsorbed molecules typically do not adsorb well to "hot spots" during fast aggregation. They are unable to show any discernible sensitivity as a result. Consequently, the issue of the enhancing impact of particular compounds may be successfully resolved by the synergistic enhancement of the enrichment approach and EM.

The molecules to be identified are enhanced by making an adsorbent and adding it to the liquid to be detected. This is an excellent method for finding compounds that are poorly adsorbed. Zhang et al., for instance, provided an enrichment approach demonstration. Mesoporous nanosponge, a porous β-CD polymer (MN-PCDP) immobilized by magnetic NPs, was synthesized (Fig. 10a) [123]. Add it to a solution of molecules that has to be identified as an adsorbent. The liquid to be detected was then put over a smooth, hydrophobic SERS substrate containing Au NPs of around 55 nm [124]. The SERS performance significantly improves under the combined influence of the enrichment technique and the substrate's EM. For instance, without a2n enrichment procedure, the substrate's detection limit for thiram (TMTD) is around 1 pM. Nevertheless, upon enrichment with MN-PCDP adsorbent, this value increases 10^2~10^3 times to around 5 fM. A complex matrix's influence in the actual sample environment was also eliminated by the MN-PCDP adsorbent's outstanding selective adsorption and enrichment capacity for a range of contaminants (BPA, carbendazim, diquat, etc.). Additionally, by immobilizing magnetic NPs, the steps of MN-PCDP adsorption, separation, and enrichment may be finished in two to 3 min. Therefore, a more extensive range of sensing devices are thought to be compatible with the robust sensing methodologies that are now in use, thanks to their ultra-fast, selective, and efficient molecular enrichment capabilities, providing easy, quick, flexible, and portable detection that is also affordable.

Furthermore, treating the liquid to be tested to enrich the molecules to be tested is also a successful enrichment approach. For instance, Song et al. created a technique (Fig. 10b) for ultrasensitive SERS detection of low analyte concentrations in water droplets on hierarchical plasma micro- and nanostructures using partial Leidenfrost evaporation assistance [125]. Initially, plasma micro/nano was created by combining Si micropillar arrays modified by carbon nanotubes (CNTs) with nano-layered metal nanoantennas as a SERS substrate. Then, thanks to the complementary effects of the enrichment approach and the substrate's EM, the SERS performance significantly improves. The substrate is enabled for SERS detection of nanomolar analytes (10^{-9} M) in aqueous solution with EF=10^7. When compared to natural evaporation, partial Leidenfrost-assisted droplet evaporation can efficiently shorten the analyte concentration process from hours to minutes, decrease the final analyte deposition footprint to a mere few hundred μm^2, and consequently increase the analyte density on the hot spot by three to four orders of magnitude. Accordingly, without further chemical treatment of the designed SERS surface, partial Leiden-Frost-assisted SERS on hierarchical plasmonic micro/nanostructures offers a versatile and simple method to bypass the diffusion limit for quick and ultrasensitive detection of low-concentration analyte droplets.

Another enrichment method involves adding noble metal particles as an enhancer by using the droplets' buoyancy, condensing the liquid drop, and enriching the molecules found in the liquid drop to improve the

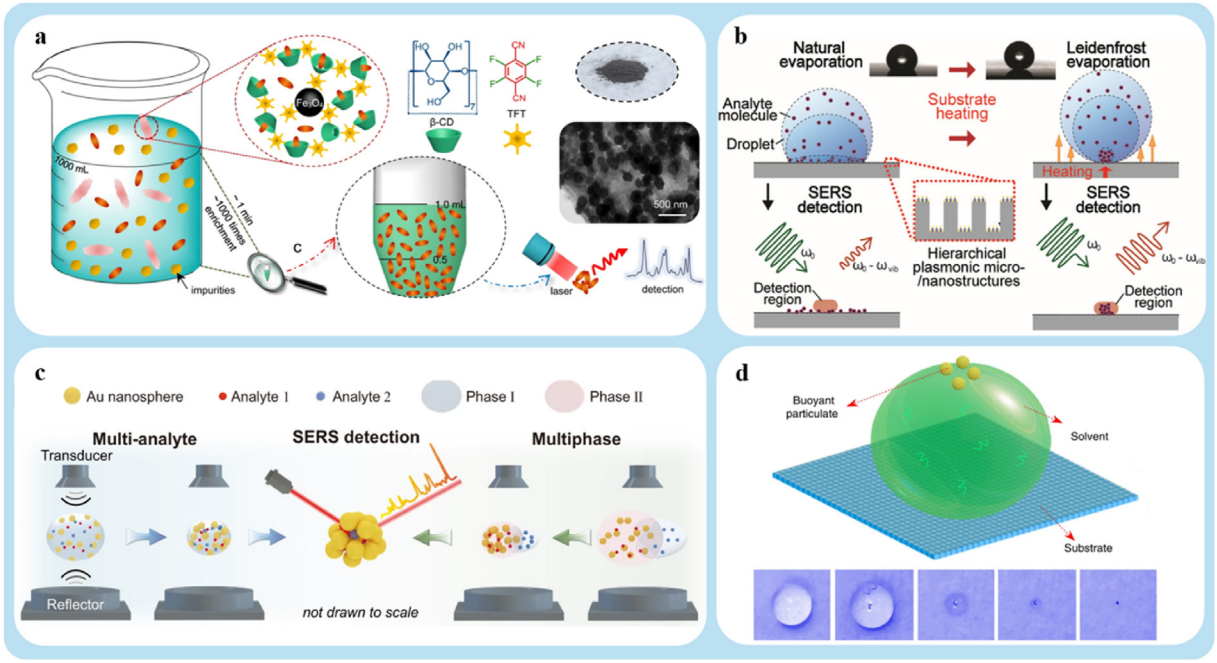

Fig. 10. (a) Diagram of the porous β-CD polymer-based current enrichment and detection process. Incorporate the processes of adsorption and desorption utilizing magnetic NPs immobilized porous β-CD polymer (MN-PCDP) with an enrichment of around 1000 times. Copyright 2021, Springer Nature. (b) Diagram demonstrating the detection of low-concentration analyte molecules in a Janus water droplet atop hierarchical plasmonic micro-/nanostructures using SERS aided by partial leidenfrost evaporation. Copyright 2020, American Chemical Society. (c) Diagram showing the multiplex and multiphase SERS detection that follow multianalyte and multiphase enrichment utilizing the DLE platform. Copyright 2022, Springer Nature. (d) Diagrammatic representations of the buoyant particulate approach. A slick surface, a solvent, and floating particles make up the suggested buoyant particulate technique. The ultimate aggregated pattern and the evaporation processes of suspended hollow silica-coated Au shell particles within a droplet. Copyright 2020, Springer Nature.

particle surface and increase the enhancement performance. For instance, utilizing a droplet suspension enrichment (DLE) platform, Chen et al. showed non-destructive analyte enrichment at any step (Fig. 10c) [126]. Au NPs were added as SERS enhancers into the suspended analyte solution droplets to achieve ultra-sensitive SERS detection and enrich the analyte. The platform shows exceptional SERS performance with a LOD of 10^{-18} M under the synergistic influence of the strong EM given by the Au NPs and the enrichment approach. The Au NPs may be concurrently concentrated with analytes in various phases. Precisely, the sound pressure of the sound wave generated by the piezoelectric transducer compensates for the gravity of the droplet, thus achieving droplet suspension [127]. The aqueous solution is then introduced into an organic phase (such as toluene) through the pipette suction to achieve multiphase analyte enrichment. Similarly, Zhang et al. presented a buoyant plasma particle-based plasmonic sensing technique for so-called few--to-single-particle nanosensors (Fig. 10d) [128]. The first step in creating large-sized (30–100 μm.), lightweight, floatable particles was to use a seed-mediated growth method. Specifically, Au NPs were coated on hollow SiO_2 large-sized floating particles, which prevented the coffee-ring effect and improved the analyte's ability to be spatially enriched at plasma-sensitive sites by aggregation and elevation effects. With a LOD of 10^{-18} M for CV, dimer and single-particle nanosensors demonstrate robust SERS performance when the enrichment approach and substrate EM work together. Many plasmon-enhanced sensing applications can benefit from employing current buoyant particle techniques, which provide easy, quick, adaptable, affordable, and portable detection.

The synergistic impact of the EM-enhanced substrate and the enrichment approach demonstrates the excellent SERS performance. It successfully resolves the issue of weakly adsorbed compounds with low enhancing effects and raises the SERS analysis's sensitivity, accuracy, and dependability. It offers a valuable method for trace material analysis and detection. This set of technologies is anticipated to become increasingly significant in the disciplines of environmental monitoring, biomedicine, and other related areas in the future. Encourage the advancement of technical innovation and scientific research.

4. Applications of SERS substrates

Currently, several practical applications of these substrates have been successfully implemented, driven by the indispensable advantages of SERS technology and extensive research on substrate fabrication in

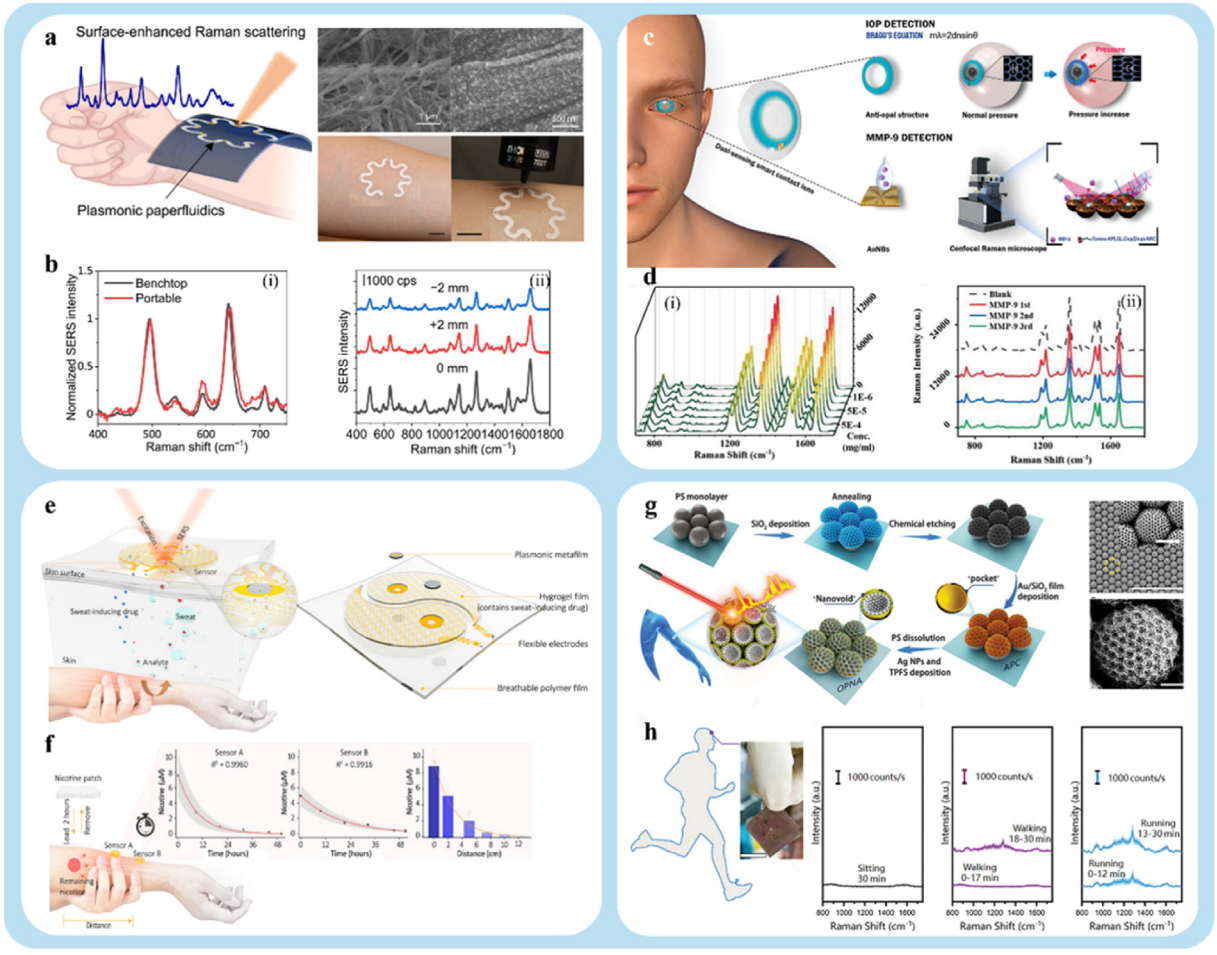

Fig. 11. (a) Conceptual illustration of a wearable plasmonic paper fluidic system for sweat collection, storage, and in situ SERS analysis, (b) (i) SERS spectra obtained using portable and tabletop spectrometers are compared, (ii) SERS spectra of 100 μM UA with the laser source and plasmonic sensor's distances altering prior to spectra normalization. Copyright 2022, American Association for the Advancement of Science. (c) Diagrammatic representation of the dual-purpose contact lens sensor, which consists of the peptide-functionalized Au NBs SERS substrate for MMP-9 detection and the antiopal structure for IOP monitoring, (d) (i) the raman spectra of tamra-pep on Au NBs after treatment with different concentrations of MMP-9 (1, 10, 50, 100, 500 ng mL^{-1},1 μg mL^{-1}), (ii) the raman spectra of Tamra-pep on Au NBs after each round of incubation with MMP-9 (10 ng mL^{-1}) for 3 times. Copyright 2022, Willey. (e) Plasmonic metamaterial–integrated wearable SERS sensing device. Schematic drawing showing the working principle and design of the device, (f) in vivo monitoring of the nicotine metabolization process in human skin. Copyright 2021, American Association for the Advancement of Science. (g) Preparation process of OPNA substrate and SEM images of APC and OPNA substrate, (h) the picture of perspiration filling the test zone on OPNA (right) after 12 min of jogging, and the mounting locations on a human forehead (left). Copyright 2022, Willey.

related fields. The following sections provide a comprehensive overview of the key applications of SERS substrates in analytical chemistry, biomedicine, wearable sensors, and small-molecule analysis.

4.1. Wearable sensor applications

Wearable sensor technology is poised to play a pivotal role in the future of personalized medicine. These sensors must overcome the mismatch between conventional rigid silicone-based sensors and soft, elastic biological tissues, allowing soft layers to conform to biological interfaces like the epidermis, eyes, and nerves [129–131]. In parallel, SERS technology offers exceptional specificity, ultra-high detection sensitivity, and non-invasive properties, making it ideal for use in wearable sensors for health monitoring.

Wearable sweat sensors primarily rely on enzymes and antibodies as biological recognition components to detect metabolites and stress indicators in sweat. While they enable precise measurement, enzymes and antibodies can degrade over time, affecting sensor performance. Mogera et al. developed a wearable paper-based microfluidic plasma device for continuous and simultaneous quantitative monitoring of sweat rate, metabolites, and sweat loss (Fig. 11a) [132]. Label-free SERS-based plasma sensors provide chemical "fingerprint" information for analyte identification. The device demonstrated sensitive detection and quantification of uric acid in sweat at both physiological and pathological concentrations (Fig. 11b). Additionally, the well-defined flow characteristics of the paper microfluidic device allow for accurate quantification of sweat volume and rate. The wearable plasmonic device is soft, flexible, and stretchable, allowing firm contact with the skin without causing chemical or physical irritation.

Contact lenses, which provide direct contact with the eye, have emerged as a popular wearable device for health monitoring. Biosensors can be integrated into contact lenses to enable real-time, non-invasive disease diagnosis. Ye et al. developed a biocompatible, dual-function intelligent contact lens sensor used to measure matrix metalloproteinase-9 (MMP-9) and monitor intraocular pressure (IOP) (Fig. 11c) [133]. The uniform nanobowl single-layer structure of the Au NBs SERS substrate is achieved through a metal film-coated nanosphere structure. The quantitative analysis of MMP-9 in tears yielded a result of 1.29 ng mL^{-1}, outperforming previous studies on MMP-9 detection or IOP monitoring (Fig. 11d). High-performance dual detection of MMP-9 and IOP can be achieved. The continuous, direct contact of the contact lens with tear fluid effectively resolves the issue of low tear fluid sampling for MMP-9 detection. The smart contact lens provides a convenient, non-invasive, and versatile tool for tracking health-related biomarkers in human tears.

Wearable sensors must withstand mechanical stresses and deformations associated with bodily movement, making durability a key requirement. Wang et al. proposed a wearable plasmonic electronic sensor with "universal" molecular identification capabilities (Fig. 11e) [134]. Individual drug metabolic profiles were produced, and trace drug changes in vivo were effectively observed as a proof-of-concept example. For example, the sensor was calibrated with artificial sweat containing varying nicotine concentrations to measure nicotine. Nicotine concentrations as low as 100 nM were detected. As shown in Fig. 11f, a volunteer had a nicotine patch (10 mg) applied to their forearm for 2 h before removal. One sensor (sensor A) was placed directly on the patch area after cleaning. The other sensor (sensor B) was placed about 2 cm away from the patch area. Nicotine levels in perspiration were monitored over the next 48 h. Nicotine levels at both sites showed an exponential decline, characteristic of drug metabolism. The results demonstrate that the biosensor can effectively monitor nicotine metabolism. Additionally, it illustrates how wearable sensors can track dynamic pharmacokinetics to assess an individual's drug metabolism. Furthermore, nicotine levels in the patch region (sensor A) were higher than in the area 2 cm away (sensor B). Most nicotine molecules absorbed quickly diffuse into the bloodstream, as they are stored under the surface epidermis beneath the patch. This leads to a proportional spatial decrease in nicotine levels along the arm. After patch removal, multiple sensors were positioned along the arm at regular intervals to verify this. As expected, nicotine concentrations in the extracted sweat samples progressively decreased with distance. This finding suggests that the integrated sensor has limitations in detecting targets stored under superficial skin layers. In future applications, the sensor should be positioned to maximize sensitivity. Further research is required to determine the relationship between subepidermal drug concentrations and levels in blood or interstitial fluid.

Inspired by the omnidirectional light collection in insect compound eyes, Zhu et al. developed a wearable SERS sensor featuring an omnidirectional plasmonic nanovoid array (OPNA) [135]. An artificial plasmonic compound eye (APC) was created by assembling a monolayer of metal NPs to form the array (Fig. 11g). The APC features a networked structure with omnidirectional "pockets" that act as "armor" to preserve the integrity of "hot spots" under mechanical deformation, while also providing broadband and omnidirectional enhancement in fragile nanoparticle arrays. The hydrophobic OPNA was designed with an asymmetric super-hydrophilic pattern on its surface, enabling it to naturally collect and concentrate analytes from sweat. The wearable and in situ analysis of SERS sensors offers high sensitivity (10^{-16} M) and stability, presenting excellent potential for point-of-care applications. As proof-of-concept, the dynamic variations in sweat dopamine (DA) concentration during different physical activities were monitored. Fig. 11h illustrates the significant potential of the OPNA sensor for wearable health monitoring applications. A flexible OPNA sensor was affixed to a participant's forehead to measure DA levels in sweat during various physical activities, such as walking, jogging, and sitting. In the "sitting" condition, no SERS signal for DA was detected, and within 30 min, 2 μL of sweat accumulated in each test region at 33–35 °C and approximately 65% humidity.

Although significant advancements have been made in integrating SERS technology with flexible electronics for wearable sensor design, challenges remain. Despite these advancements, several challenges remain. For example, wearable sensors must endure mechanical stresses and deformations from regular use. However, maintaining the integrity of delicate nanostructures in plasmonic metasurfaces is challenging during frequent body movement and daily activities. This implies that in real-world applications, the durability of the SERS substrate structure is a primary concern.

4.2. Biomedical applications

Biomedicine is a key field where SERS technology is extensively applied. The development of novel materials and tools has advanced significantly in recent years. These novel materials and devices enable SERS to be applied in bio-related systems [136,137]. The main advancements here are SERS bioassays conducted directly in cells and bioassays conducted in bodily fluids [138,139]. These applications include drug administration and detection, cancer diagnosis and treatment, and various emergency tests, such as stroke, abortion, and inflammation.

Preventing mortality from acute myocardial infarction (AMI) relies on accurate and timely diagnosis. Furthermore, the complementary roles of cardiac biomarkers, cardiac troponin I (cTnI) and creatine kinase myoencephalon (CK-MB), are crucial in both the early and late phases of AMI. Simultaneously detecting these biomarkers using traditional fluorescence and electrochemical methods is challenging. Lee et al. described a one-stop immunological SERS detection tool based on nanotechnology for progressive tracking of AMI episodes and rapid, accurate screening of various cardiac biomarkers (Fig. 12a) [140]. Anisotropic plasmonic Au nanocubes were used for optimal SERS, providing high yield, optimized excitation wavelength, and favorable optical properties. The addition of immobilized antibodies maximized the immunoassay reaction efficiency. The SERS platform enables rapid identification of AMI using a portable Raman spectrometer, thanks to its accurate estimation of AMI onset and

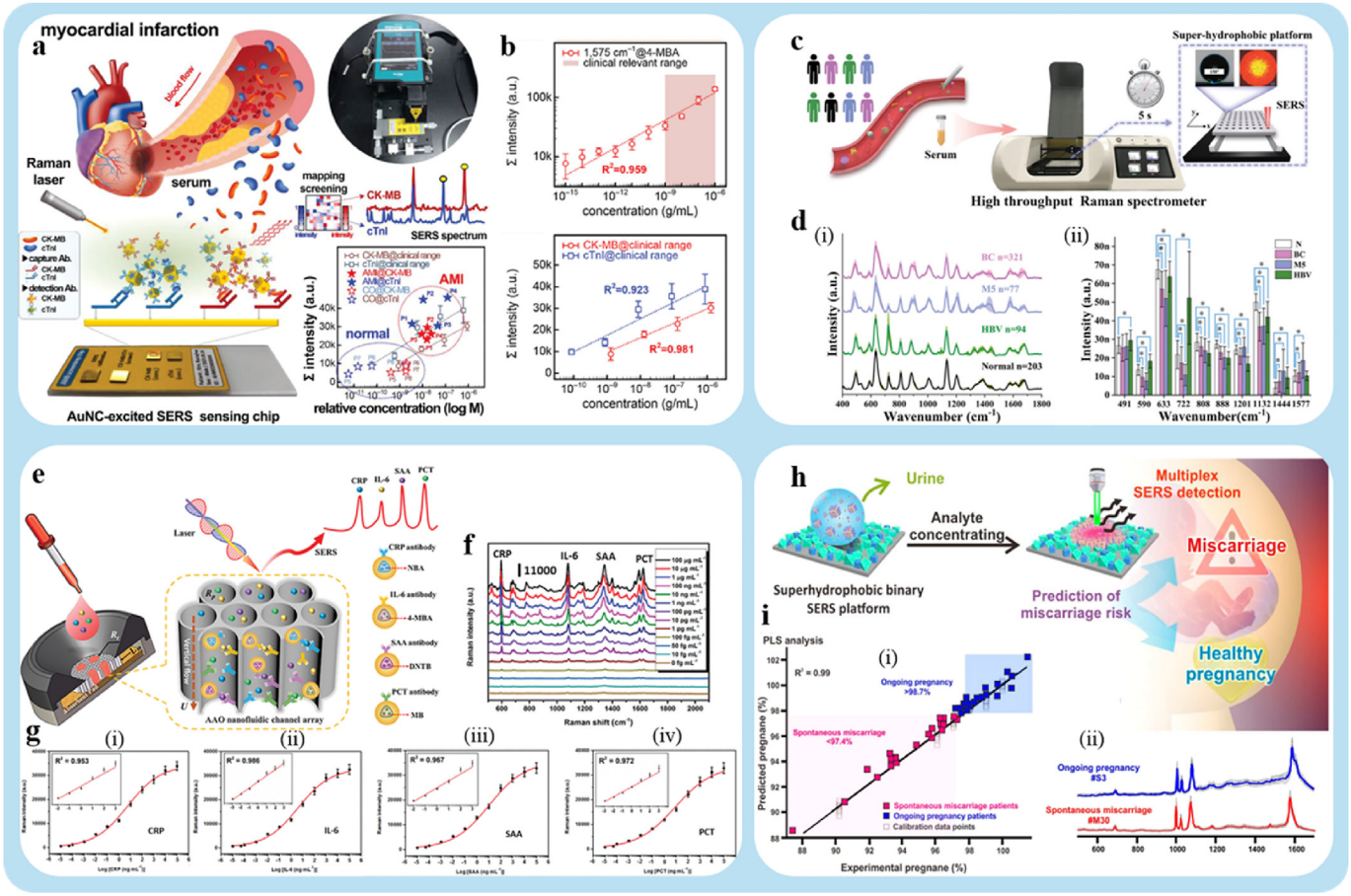

Fig. 12. (a) Diagram of a plasmonic nanocube-excited SERS readout technique for quick and accurate AMI screening and tracing based on an optical sensing chip for multiple cTnI and CK-MB biomarker detections, (b) concepts and calibration curves of multipurpose SERS immunoassay platform to detect (i) single CK-MB and (ii) a mixture of CK-MB and cTnI, respectively, along with their corresponding SERS response characteristics at bands 1575 cm^{-1}. Copyright 2024, Willey. (c) Diagram of the high-throughput and super-hydrophobic SERS platform for BC, M5, HBV, and N screening, (d) (i) normalized averaged SERS spectra comparison of the 321 BC, 94 HBV, 77 M5, and 203 N serum samples, (ii) the corresponding histograms of the average intensities and standard deviations of the SERS peaks of the BC, HBV, M5, and N groups. Copyright 2021, Willey. (e) Diagrammatic representation of the multiplex vertical flow assay (VFA) using nanoporous AAO for the identification of four inflammatory biomarkers using core-shell SERS nanotags encoded with raman dyes, (f) averaged raman spectra of the test array with different concentrations of CRP, IL-6, SAA, and PCT, (g) (i-iv) dose–responsive curves of CRP, IL-6, SAA, and PCT, respectively. Copyright 2020, Willey. (h) Diagrammatic representation of a SERS diagnostic platform based on metabolomics for stratifying miscarriage risk in pregnant women exhibiting signs of an impending miscarriage, (i) pregnane% from urine samples from 20 spontaneous miscarriages and 20 continuing pregnancies (i), urine sample SERS spectra from continuing pregnancy patient number 3(ii) and miscarriage patient number 30 are shown. Copyright 2020, American Chemical Society.

progression in human serum. This integrated platform, offering prompt treatment and monitoring, has had a significant impact on forensic and emergency medicine. CK-MB and cTnI were detected at concentrations as low as 6.56 FG·mL^{-1} and 11.81 FG·mL^{-1}, respectively (Fig. 12b).

Blood analysis is crucial for improving patient survival and enabling early cancer screening. However, developing efficient strategies for high-throughput blood analysis-based early cancer diagnosis remains challenging. Lin et al. designed a unique automated superhydrophobic platform paired with SERS and a label-free serum analysis system based on deep learning [141]. In addition, an efficient point-of-care diagnostic system and an automated high-throughput Raman spectrometer were developed (Fig. 12c). This system was designed to detect leukemia M5 (M5), hepatitis B virus (HBV), and breast cancer (BC). The grooves on the superhydrophobic terrace surface help localize and bring the target closer for analysis. Adding Ag NPs enhances sensitivity, achieving a LOD of approximately 10^{-12} M. Additionally, combining SERS with deep learning (DL) resulted in excellent diagnostic accuracy (98.6%) in the external holdover test set, suggesting that this method could lead to rapid, high-throughput, label-free disease screening tools.

There is an urgent need for the development of ultrasensitive and high-throughput detection tests to identify inflammatory diseases. Chen et al. developed the sensing membrane of a vertical flow analysis device using functionalized nanoporous anodic Al oxide (AAO) [142]. Encoded core-shell SERS nanotags were used to label several inflammatory biomarker tests (Fig. 12e). Multiple capture antibodies were applied to modify a 2×2 test array on porous AAO, enabling the extraction of inflammatory biomarkers from samples. The high surface area-to-volume ratio of the AAO film, along with its impact on plasmonic coupling, enhances the electromagnetic field of the encoded core-shell SERS nanotags. The detection limits for CRP, IL-6, SAA, and PCT were 53.4, 4.72, 48.3, and 7.53 FG·mL^{-1}, respectively. Consequently, high-throughput biomarker detection using porous AAO-based SERS VFA shows considerable potential. This approach holds potential for clinical diagnostics in resource-limited settings.

In the first trimester, 15%–20% of pregnancies result in threatened miscarriage, typically characterized by vaginal bleeding or abdominal discomfort. In 25% of these cases, the pregnancy results in spontaneous miscarriage [143]. To assess the risk of miscarriage in patients presenting with symptoms of threatened miscarriage, practitioners require a noninvasive point-of-care diagnostic tool. Kao et al. described a “limit--capture” technique for multiplex detection of two urine metabolite families associated with miscarriage risk [144]. Tetrahydrocortisone,

20α-diol-3α-glucuronide, and 5β-pregnan-3α could fill the gap in identifying impending miscarriage (Fig. 12h). This technique utilizes nanoscale surface chemistries to extract target compounds from a complex urine matrix. These compounds were then confined to a superhydrophobic SERS platform, delivering excellent performance with an EF of 10^{12} and a LOD of 10^{-12} M. The 30-min screening process includes urine preparation, sample drying on the SERS platform, SERS measurement, and stoichiometric analysis. A case-control study was conducted in 40 pregnant women presenting with symptoms of threatened miscarriage to quantify tetrahydrocortisone and pregnancy-related metabolites. These measurements closely corresponded with pregnancy outcomes. Compared to existing analytical platforms, the combination of SERS and metabonomics offers several advantages. Key features include label-free multiplexing, ultra-low subnanomolar detection limits (10^{-12} M), low sample volume requirements, simple sample handling, precise molecular fingerprints for accurate metabolite identification, and rapid noninvasive quantification. This method is particularly useful in scenarios with limited sample quantities, such as screening with tears or sputum. It can be applied for the detection of multiple diseases in diverse clinical settings.

Cancer is one of the most significant threats to human health, and the chances of curing advanced-stage cancer are very low. Therefore, improving cancer survival rates relies heavily on early detection and appropriate treatment [145]. Due to its high sensitivity, unique "fingerprint" properties, low phototoxicity, resistance to photobleaching, and in situ detection capabilities, SERS has proven to be an effective approach. Analytical diagnostic techniques play a crucial role in early cancer detection and treatment.

Lung cancer is one of the most common primary malignant tumors, and the survival rate of patients with it is extremely low [146]. However, most people with early-stage lung cancer exhibit no noticeable symptoms or pain, often missing the critical window for clinical intervention [147]. Gaseous aldehydes in human breath, associated with inflammation and oxidative stress, have been identified as traditional indicators of early lung cancer. Gao et al. first developed a large-scale (4-inch) commercial SERS wafer with an Ag/Si/Ag PMPD micro-nano porous structure [148]. Gaseous aldehydes serve as biomarkers for the diagnosis of early-stage lung cancer. Its unique particle structure is designed to fit within the micro-nano porous structure (Fig. 13a). The substrate exhibits strong SERS performance on gaseous aldehydes due to its dual capture of light and gaseous molecules. Gaseous aldehydes in exhaled breath are considered one of the most representative indicators of early lung cancer. For gaseous 4-ethylbenzaldehyde (EBA), the substrate has a LOD of 0.1 ppb and an RSD of approximately 16.5 %. The production of commercial

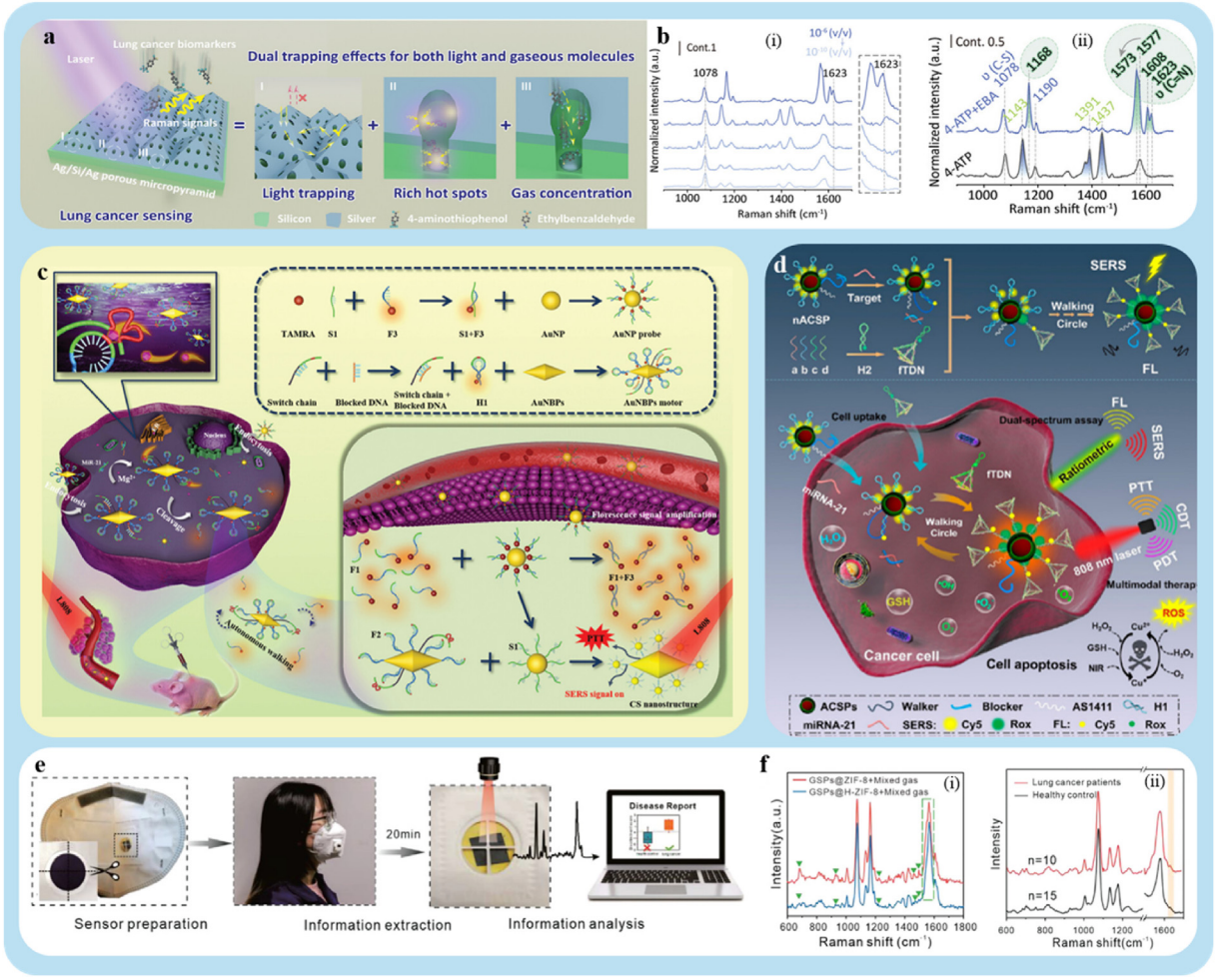

Fig. 13. (a) Direct preparation of the Ag/Si/Ag PMPD diagram on a 4-inch Si wafer, (b) (i) normalized raman spectra of 4-ATP before and after reacting with EBA, (ii) raman spectra of 4-ATP + EBA with different concentrations of 4-EBA. Copyright 2023, Willey. (c) Principle of target-induced CS nanostructures assembly strategy for simultaneous imaging and quantification of intracellular miR-21 and fluorescence-guided PTT. Copyright 2020, Willey. (d) Design of the fTDN-assisted DNA walking nanomachine for simultaneous ratiometric SERS-FL assay of miRNA-21 and illustration of the developed nanodevice for miRNA detection and imaging in live cells and ACSPs-mediated multimodal synergistic therapy. Copyright 2021, American Chemical Society. (e) Diagram of a SERS sensor for VOC detection and digital photos of paper-based SERS substrate and mask sensing device for the breath test, (f) (i) SERS spectra of 4-ATP reacted with aldehyde in simulated mixed gas, (ii) mean raman spectra from tests in healthy people and lung cancer patients. Copyright 2022, Willey.

SERS sensors can be significantly increased by dividing this large-scale sensor into smaller units (1 cm^2). Over 65 chips can be produced from a single 4-inch wafer. Additionally, a medical breathing bag incorporating this small chip was meticulously designed and studied. An early warning system was developed and implemented based on the findings of the breathing bag test. An early warning system was developed and implemented based on the findings of the breathing bag test. Compared to previous samples, the sensor demonstrates superior SERS performance and greater potential for large-scale production. It provides a new perspective and approach for the commercial application of SERS.

Integrating biological therapy and detection into a single system is an innovative therapeutic strategy for effective cancer treatment. Li et al. developed a targeted activation system using Au nanoparticle probes (AuNP probes) and Au nano bipyramidal motors (Au NBPs) [149]. A heart-satellite nanostructure (CS) assembly enables the quantification of intracellular microRNA-21 (miR-21), dual-signal imaging, and cancer treatment via photothermal therapy (PTT) (Fig. 13c). MiR-21 triggers the interaction between AuNP probes and Au NBPs upon entering cells, leading to the formation of CS nanostructures. This system enables successful scanning and quantification of miR-21 in individual cells, allowing differentiation between tumor and normal cells. Additionally, the assembly employs PTT to inhibit tumor growth and destroy tumor cells, guided by fluorescent signals. The in vitro and in vivo results demonstrate the promising potential of this method for cancer detection and therapy. Furthermore, the system exhibits high sensitivity and a low LOD.

MicroRNA (miRNA) serves as a critical biomarker for regulating genes associated with tumors [150]. Therefore, accurate miRNA analysis is essential for targeted therapy, clinical diagnosis, and prognosis monitoring. Detecting miRNAs within single live cells has been used to clarify miRNA distribution and track the progression of cancer treatment. However, reliable intracellular miRNA detection remains a significant challenge due to the complex tumor environment and the low abundance of miRNAs in tumor cells [151]. Based on this, He et al. constructed an integrated smart nanodevice composed of Au@$Cu_{2-x}S$@polydopamine NPs (ACSPs) and tetrahedral DNA nanostructures conjugated with fuel DNA (fTDNs) [152]. ACSP nanoprobes play a critical role in anti-tumor therapy and in situ monitoring of microRNAs (miRNAs) in cancer cells (Fig. 13d). By combining ACSPs as an efficient detection substrate with fTDNs, a SERS-high fluorescence (FL) dual-spectral biosensor was developed, achieving ultra-low background signals and excellent sensitivity. The detection limits of FL and SERS were 0.11 pM and 4.95 aM, respectively. The dual-signal ratio approach enabled accurate SERS quantification of miRNA in cancer cells and rapid FL imaging, improving diagnostic accuracy. In therapeutic applications, ASCs can function as integrative nanoscale agents for multimodal synergistic tumor treatment due to their high oxygen-generating capacity and excellent photothermal conversion efficiency. Notably, in vitro and in vivo studies have demonstrated potent anti-cancer properties and good biological safety, indicating potential applications in diagnosis and treatment.

Li et al. proposed using hollow ZIF-8 wrapped around Au superparticles with a yolk-shell structure as a SERS substrate to accurately identify biomarkers in complex exhaled breath and eliminate interference from other components [153]. Similar to the solid ZIF layer, the hollow ZIF-8 layer is enriched with gas molecules that interact with functional molecules on the surface of the superparticles, generating a strong reaction signal. The hollow ZIF layer has a detection limit five times lower than that of the core-shell structured material and can efficiently filter out interfering molecules not coupled with the target molecules. Additionally, a mask-type sensor was developed, and PC-LDA was applied to model the spectra, estimating the likelihood of illness in a natural population. To complete the breathing test conveniently and comfortably, the SERS substrate was filtered onto filter paper and placed at the breathing valve of the mask, forming a mask-type detector (Fig. 13e). The morning exhalations of ten lung cancer patients and fifteen healthy individuals were examined. The chemometric model was supervised using principal component-linear discriminant analysis (PC-LDA) to differentiate lung cancer patients from healthy individuals. Positive and negative results for lung cancer biomarkers can be identified by combining a machine learning-based classification algorithm with the SERS sensor based on GSPs and H-ZIF-8. This fast, simple, and affordable diagnostic technique offers numerous benefits and has the potential for lung cancer screening.

Despite the promise of SERS technology in biomedical applications like cancer diagnosis and disease monitoring, several hurdles remain that hinder its widespread practical use. For instance, diagnostics necessitate substrates that provide reliable, quantifiable outcomes across batches-a challenge for several SERS platforms, since nanoscale discrepancies in plasmonic hotspots result in erratic signal variances. It is believed that there will be applications in the high-end pharmaceutical industry in the future, but their practical use on a broad scale remains limited. Moreover, the available pertinent research relies on a limited array of real or simulated samples, and the impact of SERS substrates across a broad spectrum of practical applications, along with the associated challenges, remains inadequately addressed in the literature. Consequently, the practical utilization of SERS substrates in biomedicine remains a significant area for research.

4.3. Micromolecular detection applications

Due to its low detection limit, SERS has numerous applications in analytical chemistry. Additionally, SERS technology operates under gentle conditions, allowing sample analysis in less demanding environments. It avoids extreme temperatures or pressures required by some other analytical techniques. This feature makes SERS technology more suitable for analyzing delicate materials, such as biological samples. The ability to perform in-situ detection is a major advantage of SERS technology. This allows samples to be analyzed without altering or damaging their original condition. This is beneficial for studying a sample's characteristics and behavior in its natural state. Owing to these advantages, SERS has been applied in a wide range of fields. For example, SERS is used for detecting pesticide residues, monitoring plant health, and identifying explosives, drugs, and VOCs.

Gas sensors are highly sought after in industries such as environmental research and medicine. However, maintaining high sensitivity during multiple tests on complex gas samples remains a challenge for experts. Yang et al. incorporated $Ti_3C_2T_x$ MXene into a microfluidic gas sensor with a 3D transferable SERS substrate [154]. This resulted in the creation of a high-sensitivity, multiplex-detection microfluidic gas sensor (Fig. 14a). The use of MXene significantly enhances the sensor's adsorption efficiency for various gases. Sensitivity is improved by the in-situ gas vortex generated within the intricate nano-micron structure, which extends the time molecules remain in the SERS active zone. A proof-of-concept experiment based on the intrinsic SERS signal of the gas molecules demonstrates that the LOD for three common VOCs ranges from 10 to 50 ppb. Classical least squares (CLS) analysis reveals the precise composition of the gas mixture with an average accuracy of 90.6%. A color barcode was also generated based on CLS results to visually represent the sample's complex composition. Similarly, Yang et al. developed an intelligent microcontroller by integrating SERS spectroscopy with microfluidic chips [155]. This system combines multiple detection units to study physisorption and chemisorption mechanisms for the simultaneous detection of VOCs (Fig. 14c). Integrating microfluidics with various nanostructures on a single chip enables a customizable configuration for detecting diverse volatile substances. It has been shown that nine distinct aromatic gases, including aldehydes, ketones, and sulfides, can be simultaneously detected, achieving on-chip signal amplification with enhanced repeatability, excellent robustness (8% error), remarkable selectivity, and high sensitivity (ppb level). Ongoing research explores the use of universal gas sensors for diagnosing exhalation diseases and monitoring indoor air pollution.

The analysis and identification of specific small molecules in plants

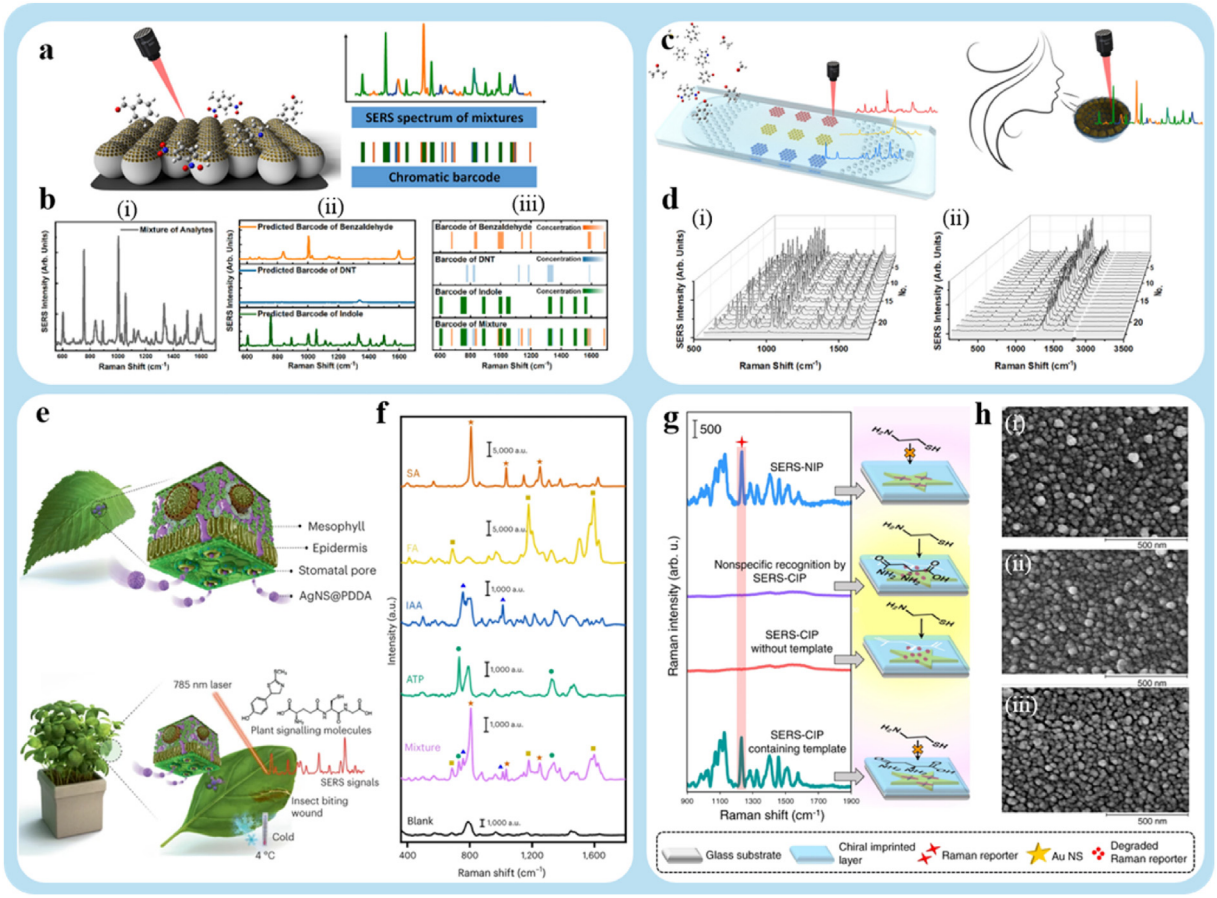

Fig. 14. (a) Schematic diagram of multiplex VOCs gas detection, (b) (i) the SERS spectrum of the example ternary gas mixture, (ii) the spectrum of each vaporized compound was calculated from the CLS results, (iii) the chromatic barcodes of each composition, the concentration was converted from the calculated intensity according to the standard detection curves. Copyright 2021, American Chemical Society. (c) Schematic diagram of the overall universal gas sensor and the principle of three different detection units, (d) SERS spectra of all 35 samples with different concentrations measured by (i) UB and (ii) UC. Copyright 2022, American Chemical Society. (e) Schematic of Ag NS@PDDA infiltration through stomatal pores and its distribution in the cross-section of the plant's leaf, (f) SERS spectra of various plant signaling molecules, namely, 10 μM SA, 10 μM FA, 100 μM IAA, 100 μM ATP, their mixture, and the SERS spectrum of Ag NS@PDDA alone. Copyright 2023, Springer Nature. (g) Raman spectra of DTTC on different platforms and corresponding platform statuses, (h) SEM images of (i) SERSCIP containing a D-asparagine template, (ii) SERS-CIP without a D-asparagine template, and (iii) SERS-NIP. Copyright 2022, Springer Nature.

can help determine their growth status. For example, plants release chemicals to trigger their defense mechanisms under stress. Identifying these stress-related molecules offers an opportunity to manage stress and prevent the onset of diseases. However, locating endogenous signaling molecules in living plants remains challenging due to their low concentration and interference from other substances. Using SERS, Son et al. developed a non-destructive nanoprobe for real-time identification of multiple stress-related endogenous chemicals in live plants (Fig. 14e) [156]. The probe consists of a silicon nanosphere encased in a corrugated Ag shell, modified with diallyl dimethyl ammonium chloride, a water-soluble cationic polymer. This structure enables interaction with multiple signaling molecules found in plants. The probe's outstanding SERS performance is demonstrated by an acquisition time of approximately 100 ms, with a signal-to-noise ratio of 64 and an EF of 2.9×10^{7}. The probes effectively measure stress-related chemicals indicating the early onset of plant disease, such as glutathione, crucifer alexins, extracellular adenosine triphosphate, and salicylic acid, under both biotic and abiotic stress. This demonstrates that the probe can detect stress at an early stage, enabling timely intervention to help plants manage diseases.

Discrimination between different molecules is crucial in environmental and biological sciences. Detecting chiral molecules can be difficult due to their intrinsic lack of optical activity or unavoidable nonspecific binding of the incorrect enantiomer. Arabi et al. presented an "inspector" identification mechanism (IRM), which is implemented on a polydopamine (PDA) layer coated with a SERS tag layer containing chiral imprints (Fig. 14g) [157]. The IRM operates based on an imprinted PDA that detects changes in permeability after molecular chiral recognition and permeability analysis. The correct enantiomer can precisely recognize and fill the chiral imprint, while the incorrect one cannot. Subsequently, the linear form of the aminothiol molecule is added as a detector to assess the state. It can only pass through empty spaces and loosely populated cavities, leading to a reduction in the SERS signal. Non-specific recognition of the incorrect enantiomer is prevented, and chiral information is acquired only through strong enantiospecific binding. Due to its sensitivity and adaptability, the IRM can effectively discriminate between chiral compounds.

SERS-based biomolecule detection is a rapidly advancing field, but detecting sugars in bodily fluids in an unlabeled and sensitive manner remains challenging. Zhang et al. created a new SERS substrate ($AgNS_{600}$) by mechanically scratching a smooth Ag sheet, forming a multi-dimensional "hot spot" area that captures glucose molecules through nanoscale grooves on the substrate's surface [158]. Enhanced SERS fingerprinting was successfully achieved (Fig. 15a). The platform demonstrated a detection limit as low as 0.5×10^{-18} M in deionized water, highlighting its speed, reliability, and reproducibility. The platform's adaptability and specificity were further demonstrated by detecting various monosaccharides, polysaccharides, and mixed samples, distinguished using machine learning and heat mapping. Importantly,

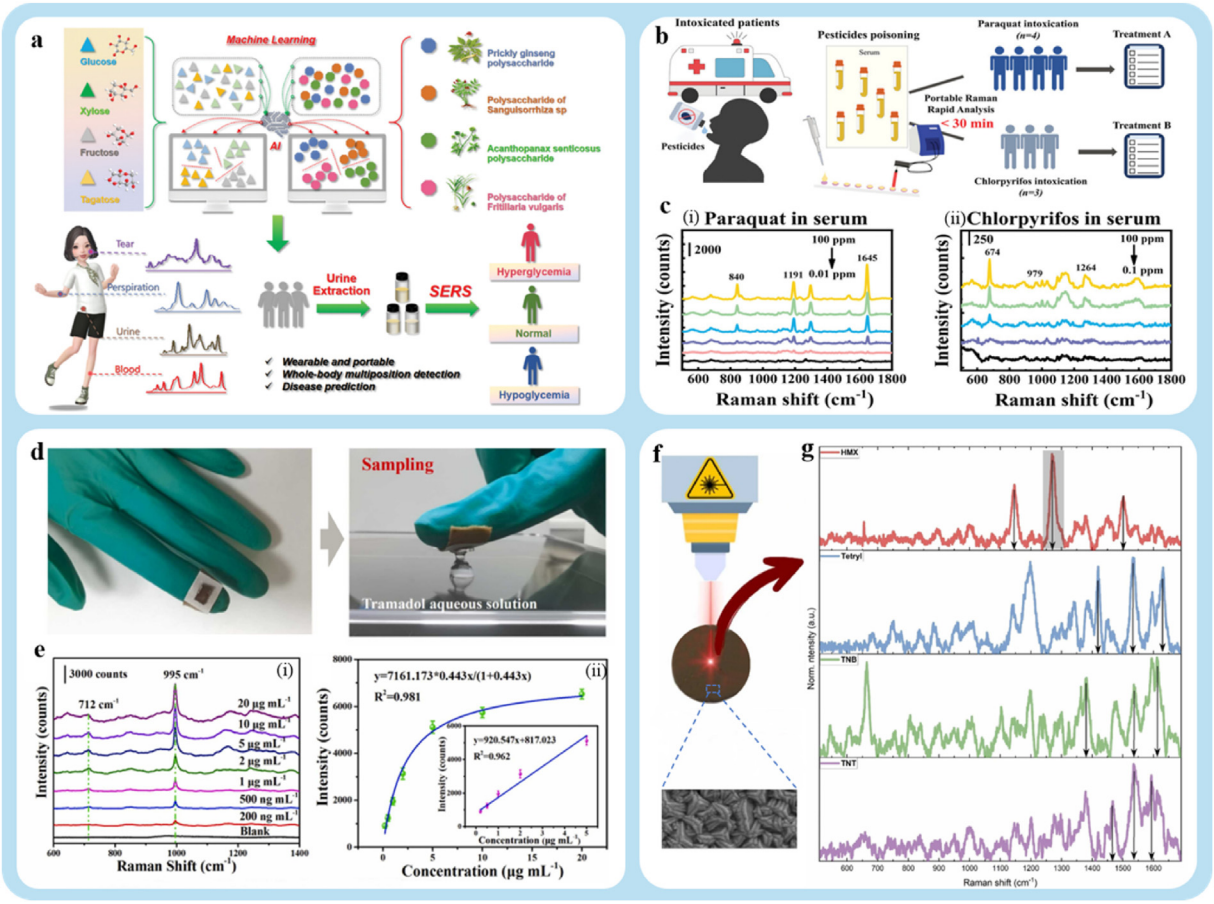

Fig. 15. (a) Through LDA classification, the SERS spectra of 4 monosaccharides and 4 polysaccharides were intelligently distinguished. And wearable and portable SERS substrates are used to detect bodily fluids in several positions and anticipate possible metabolic illnesses linked to glycemics. Copyright 2023, Willey. (b) Diagrammatic illustration of a quick paper-based SERS detection platform for determining PQ and CPF poisoning in patient serum in order to select the best emergency therapy, (c) SERS spectra of (i) PQ and (ii) CPF in human blood at doses ranging from 100 to 0.01 ppm and 100 to 0.1 ppm, respectively, (d) demonstration diagram of glove-based SERS sensor collecting liquid samples. Copyright 2023, Willey. (e) (i) Oncentration-dependent SERS spectra of tramadol in serum, (ii) function of the peak intensity at 995 cm^{-1} with the spiked sample concentration. Copyright 2023, Elsevier. (f) Screenshot for detection of explosive molecules, (g) raman spectra of the explosive compounds octogen-HMX, tetryl, 1,3,5-trinitrobenzene-TNB, and 2,4,6-trinitrotoluene-TNT. Copyright 2024, Elsevier.

real samples were tested, and results showed that the platform can detect and identify glucose-related SERS signals in blood, urine, tears, and sweat. Moreover, signal intensity analysis of multiple distinctive peaks can be used to non-invasively predict diabetes.

The label-free detection, ultra-high sensitivity, and unique chemical fingerprints of SERS-based biosensors have attracted significant interest. Lin et al. developed a wafer-scale, highly uniform, ultrasensitive, portable paper-based SERS detection apparatus [159]. The platform features rich and dense Au nanobeads with tight gap distances, directly deposited onto ultra-low surface energy fluorosilane-modified cellulose fibers by precisely controlling atomic diffusion through simple heat evaporation. With an EF of 3.9×10^{11} and a sub-femtomolar detection limit (single-molecule level), the paper-based SERS substrate demonstrates exceptional performance. This technique recognizes twelve distinct analytes, including clinical drugs, pesticides (thiram, paraquat, carbaryl, chlorpyrifos), environmental carcinogens (benzopyrene), and illegal narcotics (methamphetamine, mephedrone), through their chemical fingerprints. Therefore, this scalable, portable, ultra-sensitive fiber-based SERS substrate is a valuable tool for biofluid analysis, point-of-care diagnostics, and precision medicine. It is also suitable for clinical applications, such as therapeutic drug monitoring for personalized medication adjustment and ultra-early diagnosis of pesticide poisoning (Fig. 15b). The exploration of these fields opens up new possibilities.

SERS technology relies on non-destructive analysis of sample molecules and their unique fingerprint features, offering significant potential for restricted substance identification and detection. Zhang et al. developed a flexible glove-based SERS sensor for portable detection and identification of restricted substances (Fig. 15d) [160]. The glove-based SERS sensor is constructed by attaching a flexible tape substrate to the glove's fingertip for analyte extraction, followed by the adhesion of an opal photonic crystal made of polystyrene spheres (PS) to enhance the Raman signal. Au trioctahedra (Au TOH) were consistently assembled onto the adhesive tape using an interfacial self-assembly method, enhancing signal repeatability. Additionally, the adhesive tape substrate improves sampling efficiency, offers high flexibility, and facilitates conformal contact with uneven surfaces. The glove-based SERS sensor, with an RSD of less than 6%, is unaffected by different degrees of bending and stretching. The sensor can detect trace amounts of tramadol (69.19 ng mL^{-1}) and midazolam (35.03 ng mL^{-1}) in serum, demonstrating low detection limits. It offers substantial advantages in portable analysis and efficient sample extraction. Additionally, the sensor can accurately detect methamphetamine in complex binary mixtures. The glove-type SERS sensor, with its simple sampling and high sensitivity, provides a foundation for developing user-friendly wearable SERS sensors.

Security standards, forensic investigations, and contamination studies rely on the accurate and timely identification of explosives and their harmful effects. Shvalya et al. developed an enhanced substrate design for detecting various explosives by precisely controlling the oxidation of the tungsten surface and depositing an Au layer [161]. This resulted in an excellent SERS substrate for detecting molecules (Fig. 15f). The junction

of the tungsten Wulff facets forms a trench-like morphology, enhancing the SERS response by over 300% and increasing nano-roughness compared to the untreated surface. Following ultrafast Ar/O_2 plasma cleaning, the substrate demonstrates excellent repeatability, with a RSD of less than 15%. The signal recovery rate exceeds 95%. With a 10-s collection time and motion scan mode, the detection limit of the "surface dry" measurement is better than 10^{-8} M. These substrates successfully classified the chemical fingerprints of HMX, Tetryl, TNB, and TNT, with a LOD of 10^{-7} M in the "water droplet on the surface" scenario, two orders of magnitude better than the UV–Vis spectroscopy method. This demonstrates the effectiveness of the label-free SERS screening sensor in monitoring trace explosives in aqueous media.

SERS technology offers several benefits, including high sensitivity, speed, accuracy, and non-invasive, non-destructive analysis. It has numerous potential applications in analysis and detection. However, the choice of substrate plays a critical role in detection and analysis, as the effectiveness of SERS technology heavily depends on the substrate material. This reliance can lead to unpredictable outcomes. Consequently, ongoing research is needed to design and develop superior SERS substrates to meet the growing range of analytical and detection demands. Additionally, the applicability of many substrate materials is significantly limited by their cost. Further efforts are needed to address this issue.

5. Summary and perspectives

In conclusion, this work reviews the recent research progress of SERS, focusing on the preparation and application of substrates. Research on substrate preparation can be broadly categorized into noble metal and composite substrates, as well as noble-free metal substrates, based on EM and CM mechanisms. Noble metal substrates primarily rely on EM as the enhancement mechanism, largely due to the superior LSPR performance of noble metals. This generates a strong local electric field. By controlling the nanostructure or the gap between noble metal particles, the enhancement effect of the substrate can be significantly improved. Therefore, research on high-quality, customized nanostructures is a key driving force in the ongoing development of these substrates. In noble metal composite substrates, unlike pure noble metal substrates, the substrate material significantly influences the performance, alongside the noble metal's nanostructure. The matrix material typically acts as a support for noble metal particles, and the number of active sites directly affects the loading of these particles, which in turn influences substrate performance. Therefore, matrix materials are typically chosen for their chemical activity and large specific surface area. Additionally, when certain unique materials are used as matrix materials, they may generate a CT effect with probe molecules. This contributes to CM, where the substrate often demonstrates superior performance when combined with EM. Thus, advancements in material preparation methods are also a key driving force in the development of noble metal composites. Finally, reducing the high cost of noble metal-based substrates is crucial for the widespread application of SERS. The high cost of noble metal substrates arises from the expensive precursor materials and the complex procedures needed to fabricate their intricate structures. Replacing noble metals (Au, Ag, etc.) with cheaper alternatives (Cu, Al, etc.) is a potential solution. The challenge lies in maintaining high EFs and chemical stability, and current progress in this area remains limited. However, advancements in preparation techniques, including those for noble metals, can help mitigate the cost issue to some extent.

Noble metal-free substrates primarily rely on CM as the enhancement mechanism. However, unlike noble metal NPs and their composites, no unified enhancement theory exists for noble metal-free substrates. As discussed in Section 2.2, the CT effect in substrate-molecule complexes can follow multiple potential pathways. Different noble metal-free SERS substrates may participate in multiple or alternative pathways simultaneously. Therefore, identifying the primary contribution of the CT pathway to SERS enhancement and establishing a unified understanding of it is crucial for the development of noble metal-free SERS substrates. Noble metal-free substrates offer advantages such as enhanced activity, inherent chemical stability, and high specificity for target molecules [162,163]. Additionally, compared to the high costs of precursor materials and preparation technologies for noble metal-based substrates, noble metal-free substrates offer an unmatched cost advantage. However, noble metal-free substrates often suffer from poor SERS performance, a drawback of the CM mechanism. Thus, enhancing the performance of noble metal-free substrates is crucial for future development. The specific performance of various substrates is listed in Table 1. Future efforts should focus on two aspects: first, since the CT effect drives CM, improving the CT efficiency of substrate materials is essential. This can be achieved through experimental methods, such as band gap tuning, element doping, and similar approaches. In addition to overall material design, noble metal-free substrates are being developed. Materials with LSPR, such as nitrides and metal semiconductors, may also be developed. Notably, noble metal-free SERS substrates can generate strong synergistic enhancements, significantly improving SERS performance.

Researchers have developed wearable sensors, SERS nanolabels, chemical sensors, hand-selective systems, and specialized platforms for a wide range of sensing strategies across various fields. In human testing, many SERS-based wearable sensors can monitor physiological states through tears, sweat, and other secretions, reflecting both physiological and pathological information. In biomedicine, SERS labels and platforms are used for various applications, including emergency screenings (e.g., stroke, miscarriage, inflammation), early cancer diagnosis, drug delivery, and testing. However, since SERS technology depends on enhancing substrates, producing high-quality substrates remains a major challenge in SERS applications. Although large-scale industrial production of

Table 1
Comparison of the properties of the typical SERS substrates.

Substrates	Probe	LOD (mol/L)	EF	Refs.
ANITs	2-NTT		10^9	[52]
Au double NRs	2-NTT	10^{-7}	7×10^8	[53]
Au DWFs	2-NTT	5×10^{-8}	6.52×10^7	[55]
Elongated pseudo-hollow NFs	BT	10^{-18}	1.1×10^6	[56]
Au truncated octahedral double-edge NFs	2-NTT	10^{-17}	10^7	[57]
$_{L/D}$-Pt@Au TNRs	$A\beta_{42}$	4.5×10^{-15}		[60]
Au NHX	BT	10^{-15}		[61]
PCHs	2-NTT	10^{-7}	3.8×10^7	[63]
Ag NPs modified GNRs	R6G	10^{-9}	10^5	[65]
Ag NR@Graphene@Ag NR	PCB-3	1.72×10^{-10}	1.6×10^8	[66]
Au-NP/SnO_2/Au-NP	R6G	10^{-11}	4.6×10^5	[67]
Au NBP/End-ZIF	4-ATP	10^{-8}	7.36×10^7	[71]
Ag/PANI	R6G	10^{-8}	10^6	[76]
3D-Assembled Metallic NPs	BPE	10^{-9}	1.14×10^6	[78]
GDY HHMSs	R6G	10^{-12}	3.7×10^7	[85]
WO_{3-x}/WSe_2	MB	5×10^{-11}	5×10^{18}	[88]
$TaSe_2$ nanosheets	R6G	10^{-10}		[93]
Nb, Re-WSe_2	R6G	5×10^{-15}	2×10^9	[95]
2D BCN	CV	10^{-7}		[97]
$MSOR_1$	Bilirubin	10^{-10}	1.7×10^6	[99]
TiVC MXene	R6G	10^{-7}	3.27×10^{12}	[101]
Hybrid WN/C nanobelts	BPA	10^{-12}	6.5×10^8	[105]
Ag/BP-NS	R6G	10^{-20}	1.01×10^{11}	[108]
TiS_2/CGA	MB	10^{-13}	2.1×10^9	[111]
MXene-blanketed Au NP	RhB		1.6×10^{10}	[114]
Ag NWs on GaN NPs	R6G	10^{-15}	1.4×10^{11}	[117]
Ag-NSs/CoFe-LDHs	4-NP	2.36×10^{-14}	5.65×10^{11}	[122]

substrates differs from laboratory preparation, significant improvements are still needed in the production process. Furthermore, as society advances, artificial intelligence (AI) technologies, including machine learning and deep learning, may offer valuable insights for designing high-efficiency SERS substrates and improving analytical performance. AI has made breakthroughs in drug discovery, material design, and organic synthesis [164–166]. New computational methodologies, such as molecular design algorithms, can explore vast chemical spaces and support fields like molecular property prediction, molecule design, reverse synthesis, reaction prediction, and result forecasting [167–171]. Thus, applying supervised and unsupervised learning modes, along with algorithms like K-nearest neighbors, support vector machines, random forest, boosting, and neural networks, can greatly enhance SERS analytical performance [172]. Integrating AI with SERS technology will be a powerful tool for designing novel substrate materials with superior SERS performance, optimizing architecture, studying enhancement mechanisms, and improving analytical capabilities. It is believed that overcoming these challenges will enable SERS technology to play a crucial role across diverse application areas.

CRediT authorship contribution statement

Heguang Liu: Writing – review & editing, Supervision, Conceptualization. **Ben Mou:** Writing – original draft, Investigation. **Jinxin Li:** Investigation. **Na Tian:** Funding acquisition, Conceptualization. **Yiming Feng:** Investigation. **Xiaodong Cui:** Writing – review & editing. **Yury Kapitonov:** Writing – review & editing. **Huageng Liang:** Writing – review & editing. **Caiyin You:** Supervision, Funding acquisition. **Yuan Li:** Writing – review & editing, Conceptualization. **Tianyou Zhai:** Writing – review & editing.

Declaration of competing interest

The authors declare that they have no known competing financial interests or personal relationships that could have appeared to influence the work reported in this paper.

Acknowledgments

This work was financially supported by the projects funded by the Education Department of Shaanxi Provincial Government (NO. 23JP116), the Natural Science Fund of Shaanxi Province (NO. 2024JC-YBMS-396), the National Natural Science Foundation of China (NO. 52171191, 52371198, U22A20137), the Constructing National Independent Innovation Demonstration Zones (XM2024XTGXQ05), and Shenzhen Science and Technology Innovation Program (JCYJ20220818102215033, GJHZ20210705142542015, JCYJ20220530160811027), Guangdong HUST Industrial Technology Research Institute, Guangdong Provincial Key Laboratory of Manufacturing Equipment Digitization (2023B1 212060012).

References

[1] Y. Zhao, A. Kumar, Y. Yang, Unveiling practical considerations for reliable and standardized SERS measurements: lessons from a comprehensive review of oblique angle deposition-fabricated silver nanorod array substrates, Chem. Soc. Rev. 53 (2024) 1004–1057.
[2] S. Nie, S.R. Emory, Probing single molecules and single nanoparticles by surface-enhanced Raman scattering, Science 275 (1997) 1102–1106.
[3] M. Fleischmann, P.J. Hendra, A.J. McQuillan, Raman spectra of pyridine adsorbed at a silver electrode, Chem. Phys. Lett. 26 (1974) 163–166.
[4] D.L. Jeanmaire, R.P. Van Duyne, J. Electroanal, Surface Raman spectro electrochemistry: part I. heterocyclic, aromatic, and aliphatic amines adsorbed on the anodized silver electrode, Chem. Interfacial Electrochem. 84 (1977) 1–20.
[5] M.G. Albrecht, J.A. Creighton, Anomalously intense Raman spectra of pyridine at a silver electrode, J. Am. Chem. Soc. 99 (1977) 5215–5217.
[6] W. Yang, D. Lim, Recent advances in the synthesis of intra-nanogap Au plasmonic nanostructures for bioanalytical applications, Adv. Mater. 32 (2020) 2002219.
[7] H. Hu, Y. Tian, P. Chen, W. Chu, Perspective on tailored nanostructure-dominated spp effects for SERS, Adv. Mater. 36 (2023) 2303001.
[8] H. Ma, S.Q. Pan, W.L. Wang, X. Yue, X.H. Xi, S. Yan, D.Y. Wu, X. Wang, G. Liu, B. Ren, Surface-enhanced Raman spectroscopy: current understanding, challenges, and opportunities, ACS Nano 18 (2024) 14000–14019.
[9] S.P. Usha, H. Manoharan, R. Deshmukh, R.A. lvarez-Diduk, E. Calucho, V.V.R. Sai, A. Merkoçi, Attomolar analyte sensing techniques (AttoSens): a review on a decade of progress on chemical and biosensing nanoplatforms, Chem. Soc. Rev. 50 (2021) 13012–13089.
[10] S. Lee, S. Lee, J. Son, J.M. Kim, J. Lee, S. Yoo, M. Haddadnezhad, J. Shin, J. Kim, J.M. Nam, S. Park, Web-above-a-ring (WAR) and Web-above-a-lens (WAL) nanostructures for highly engineered plasmonic-field tuning and SERS enhancement, Small 17 (2021) 2101262.
[11] M.J. Oh, S. Kwon, S. Lee, I. Jung, S. Park, Octahedron in a cubic nanoframe: strong near-field focusing and surface-enhanced Raman scattering, ACS Nano 18 (2024) 7656–7665.
[12] J.Y. Kim, E.H. Koh, J. Yang, C. Mun, S. Lee, H. Lee, J. Kim, S. Park, M. Kang, D. Kim, H.S. Jung, 3D Plasmonic gold nanopocket structure for SERS machine learning-based microplastic detection, Adv. Funct. Mater. 34 (2024) 2307584.
[13] R. Jiang, J. Li, L. Li, Y. Lu, H. Zhang, M. Li, Engineering near-infrared plasmonic spiky gold nanostructures for highly efficient surface-enhanced Raman spectroscopy-guided cancer hyperthermia therapy, Adv. Funct. Mater. 34 (2024) 2307631.
[14] J. Son, G.H. Kim, Y. Lee, C. Lee, S. Cha, J.M. Nam, Toward quantitative surface-enhanced Raman scattering with plasmonic nanoparticles: multiscale view on heterogeneities in particle morphology, surface modification, interface, and analytical protocols, J. Am. Chem. Soc. 144 (2022) 22337–22351.
[15] Z. Li, L. Zhai, Q. Zhang, W. Zhai, P. Li, B. Chen, C. Chen, Y. Yao, Y. Ge, H. Yang, P. Qiao, J. Kang, Z. Shi, A. Zhang, H. Wang, J. Liang, J. Liu, Z. Guan, L. Liao, V.A. Neacșu, C. Ma, Y. Chen, Y. Zhu, C.S. Lee, L. Ma, Y. Du, L. Gu, J.F. Li, Z.Q. Tian, F. Ding, H. Zhang, 1T′-transition metal dichalcogenide monolayers stabilized on 4H-Au nanowires for ultrasensitive SERS detection, Nat. Mater. 23 (2024) 1355–1362.
[16] Q. Chen, M. Betker, C. Harder, C.J. Brett, M. Schwartzkopf, N.M. Ulrich, M.E.T. Molares, C. Trautmann, L.D. Söderberg, C.L. Weindl, V. Körstgens, P.M. Buschbaum, M. Ma, S.V. Roth, Biopolymer-templated deposition of ordered and polymorph titanium dioxide thin films for improved surface-enhanced Raman scattering sensitivity, Adv. Funct. Mater. 32 (2022) 2108556.
[17] Q. Lv, X. Wu, J. Tan, B. Liu, L. Gan, J. Li, Z. Huang, F. Kangbc, R. Lv, Ultrasensitive molecular sensing of few-layer niobium diselenide, J. Mater. Chem. A 9 (2021) 2725–2733.
[18] S. Zhao, H. Wang, L. Niu, W. Xiong, Y. Chen, M. Zeng, S. Yuan, L. Fu, 2D GaN for highly reproducible surface-enhanced Raman scattering, Small 17 (2021) 2103442.
[19] J. Li, W. Shen, X. Liang, S. Zheng, Q. Yu, C. Wang, C. Wang, B. Gu, 2D film-like magnetic SERS tag with enhanced capture and detection abilities for immunochromatographic diagnosis of multiple bacteria, Small (2024) 2310014.
[20] J.A. Allegretto, J. Dostalek, Metal–organic frameworks in surface enhanced Raman spectroscopy–based analysis of volatile organic compounds, Adv. Sci. 11 (2024) 2401437.
[21] P. Zhou, S. Cheng, Q. Li, Y. Pang, R. Xiao, Multifunctional MoS_2@AuNSs nanoflakes as SERS and photothermal tags for single-cell bacterial detection and in-situ inactivation, Chem. Eng. J. 471 (2023) 144514.
[22] T. Gao, T. Yachi, X. Shi, R. Sato, C. Sato, Y. Yonamine, K. Kanie, H. Misawa, K. Ijiro, H. Mitomo, Ultrasensitive surface-enhanced Raman scattering platform for protein detection via active delivery to nanogaps as a hotspot, ACS Nano 18 (2024) 21593–21606.
[23] H.J. Park, S. Cho, M. Kim, Y.S. Jung, Carboxylic acid-functionalized, graphitic layer-coated three-dimensional SERS substrate for label-free analysis of alzheimer's disease biomarkers, Nano Lett. 20 (2020) 2576–2584.
[24] N. Choi, S. Schlücker, Convergence of surface-enhanced Raman scattering with molecular diagnostics: a perspective on future directions, ACS Nano 18 (2024) 5998–6007.
[25] A. Stefancu, J. Aizpurua, I. Alessandri, I. Bald, J.J. Baumberg, L.V. Besteiro, P. Christopher, M. Correa-Duarte, B.D. Nijs, A. Demetriadou, R.R. Frontiera, T. Fukushima, N.J. Halas, P.K. Jain, Z.H. Kim, D. Kurouski, H. Lange, J.F. Li, L.M. Liz-Marzán, I.T. Lucas, A.J. Meixner, K. Murakoshi, P. Nordlander, W.J. Peveler, R. Quesada-Cabrera, E. Ringe, G.C. Schatz, S. Schlücker, Z.D. Schultz, E.X. Tan, Z.Q. Tian, L. Wang, B.M. Weckhuysen, W. Xie, X.Y. Ling, J. Zhang, Z. Zhao, R.Y. Zhou, E. Cortés, Impact of surface enhanced Raman spectroscopy in catalysis, ACS Nano 18 (2024) 29337–29379.
[26] L. Xu, Y. Xie, A. Liu, L. Xie, X. Miao, Z. Hou, L. Xiang, T. Jiang, A. Wu, J. Lin, Innovative applications and perspectives of surface-enhanced Raman spectroscopy technology in biomedicin, Small 21 (2025) 2409698.
[27] C. Duffield, L.M.R. Gomez, S.C.H. Tsao, Y. Wang, Recent advances in SERS assays for detection of multiple extracellular vesicles biomarkers for cancer diagnosis, Nanoscale 17 (2025) 3635–3655.
[28] S. Premachandran, R. Haldavnekar, S. Ganesh, S. Das, K. Venkatakrishnan, B. Tan, Self-functionalized superlattice nanosensor enables glioblastoma diagnosis using liquid biopsy, ACS Nano 17 (2023) 19832–19852.
[29] J. Wang, Y.C. Kao, Q. Zhou, A. Wuethrich, M.S. Stark, H. Schaider, H.P. Soyer, L.L. Lin, M. Trau, An integrated microfluidic-SERS platform enables sensitive phenotyping of serum extracellular vesicles in early stage melanomas, Adv. Funct. Mater. 32 (2022) 2010296.
[30] J. Park, J.A. Thomasson, C.C. Gale, G.A. Sword, K.M. Lee, T.J. Herrman, C.P.C. Suh, Adsorbent-SERS technique for determination of plant VOCs from live cotton plants and dried teas, ACS Omega 5 (2020) 2779–2790.

[31] Z.F. Gao, Y.X. Li, L.M. Dong, L.L. Zhen, J.Z. Li, Y. Shen, F. Xia, Photothermal-induced partial leidenfrost superhydrophobic surface as ultrasensitive surface-enhanced Raman scattering platform for the detection of neonicotinoid insecticides, Sens. Actuators, A 348 (2021) 130728.
[32] Y. Huang, W. Liu, Z. Gong, W. Wu, M. Fan, D. Wang, A.G. Brolo, Detection of buried explosives using a surface-enhanced Raman scattering (SERS) substrate tailored for miniaturized spectrometers, ACS Sens. 5 (2020) 2933–2939.
[33] Y. Xu, W. Aljuhani, Y. Zhang, Z. Ye, C. Li, S.E.J. Bell, A practical approach to quantitative analytical surface-enhanced Raman spectroscopy, Chem. Soc. Rev. 54 (2025) 62–84.
[34] D.C. May, A. Bonifacio, T. Bocklitz, A. Markin, N. Markina, S. Fornasaro, A. Dwivedi, T. Dib, E. Farnesi, C. Liu, A. Ghosh, J. Popp, Biomedical SERS–the current state and future trends, Chem. Soc. Rev. 53 (2024) 8957–8979.
[35] A. Patra, B.M. B, G. Manasa, A.K. Samal, C.S. Rout, 2D MXenes as a promising candidate for surface-enhanced Raman spectroscopy: state of the art, recent trends, and future prospects, Adv. Funct. Mater. 33 (2023) 2306680.
[36] V. Rajput Samriti, R.K. Gupta, J. Prakash, Engineering metal oxide semiconductor nanostructures for enhanced charge transfer fundamentals and emerging SERS applications, J. Mater. Chem. C 10 (2022) 73–95.
[37] M.S.S. Bharati, V.R. Soma, Flexible SERS substrates for hazardous materials detection: recent advances, Opto-Electron. Adv. 4 (2021), 210048–210048.
[38] C. Huang, A. Li, X. Chen, T. Wang, Understanding the role of metal-organic frameworks in surface-enhanced Raman scattering application, Small 16 (2020) 2004802.
[39] J. Mosquera, Y. Zhao, H. Jang, N. Xie, C. Xu, N.A. Kotov, L.M. Liz-Marzán, Plasmonic nanoparticles with supramolecular recognition, Adv. Funct. Mater. 30 (2020) 1902082.
[40] Y. Lu, M. Li, Rational design of near-infrared II: plasmonic optofunctional materials for diagnostic and therapeutic applications, Adv. Funct. Mater. 34 (2024) 2312753.
[41] N. Logan, C. Cao, S. Freitag, S.A. Haughey, R. Krska, C.T. Elliott, Advancing mycotoxin detection in food and feed: novel insights from surface-enhanced Raman spectroscopy (SERS), Adv. Mater. 36 (2024) 2309625.
[42] J.R. Lombardi, R.L. Birke, T. Lu, J. Xu, Charge-transfer theory of surface enhanced Raman spectroscopy: herzberg-teller contributions, J. Chem. Phys. 84 (1986) 4174–4180.
[43] Y. Huang, X. Wang, K. Lai, Y. Fan, B.A. Rasco, Trace analysis of organic compounds in foods with surface-enhanced Raman spectroscopy: methodology, progress, and challenges, Compr. Rev. Food Sci. Food Saf. 19 (2020) 622–642.
[44] K. Ge, Y. Hu, G. Li, Fabrication of branched gold copper nanoalloy doped mesoporous graphitic carbon nitride hybrid membrane for surface-enhanced Raman spectroscopy analysis of carcinogens, J. Hazard. Mater. 432 (2022) 128742.
[45] Y. Ni, C. Zhang, Y. Yuan, M. Xu, J. Yao, Determination on origination of surface-enhanced Raman scattering effect on nano ZnO substrate, Hua Hsueh Hsueh Pao 77 (2019) 641.
[46] X. Pan, X. Zhou, X. Liao, R. Yu, K. Yu, S. Lin, Y. Ding, W. Luo, M. Yan, L. Mai, Ultrafast ion sputtering modulation of two-dimensional substrate for highly sensitive Raman detection, ACS Mater. Lett. 4 (2022) 2622–2630.
[47] D. Wu, J. Chen, Y. Ruan, K. Sun, K. Zhang, W. Xie, X. Zhao, X. Wang, A novel sensitive and stable surface enhanced Raman scattering substrate based on a MoS_2 quantum dot/reduced graphene oxide hybrid system, J. Mater. Chem. C 6 (2018) 12547–12554.
[48] X.X. Han, W. Ji, B. Zhao, Y. Ozaki, Semiconductor-enhanced Raman scattering: active nanomaterials and applications, Nanoscale 9 (2017) 4847–4861.
[49] H. Sun, S. Cong, Z. Zheng, Z. Wang, Z. Chen, Z. Zhao, Metal-organic frameworks as surface- enhanced Raman scattering substrates with high tailorability, J. Am. Chem. Soc. 141 (2019) 870–878.
[50] B.N.J. Persson, K. Zhao, Z. Zhang, Chemical contribution to surface-enhanced Raman scattering, Phys. Rev. Lett. 96 (2006) 207401.
[51] C.M. Guvenc, F.M. Balci, S. Sarisozen, N. Polat, S. Balci, Colloidal bimetallic nanorings for strong plasmon exciton coupling, J. Mater. Chem. C 124 (2020) 8334–8340.
[52] S. Yoo, S. Go, J. Son, J. Kim, S. Lee, M. Haddadnezhad, H. Hilal, J.M. Kim, J.M. Nam, S. Park, Au nanorings with intertwined triple rings, J. Am. Chem. Soc. 143 (2021) 15113–15119.
[53] S. Yoo, J. Lee, J. Kim, J.M. Kim, M. Haddadnezhad, S. Lee, S. Choi, D. Park, J.M. Nam, S. Park, Silver double nanorings with circular hot zone, J. Am. Chem. Soc. 142 (2020) 12341–12348.
[54] S. Lee, I. Jung, J. Son, S. Lee, M. Park, J.E. Kim, W. Park, J. Lee, J.M. Nam, S. Park, Heterogeneous component Au (outer)–Pt (middle)–Au (inner) nanorings: synthesis and vibrational characterization on middle Pt nanorings with surface-enhanced Raman scattering, ACS Nano 16 (2022) 11259–11267.
[55] M. Haddadnezhad, I. Jung, W. Park, J.W. Lee, W. Park, J. Kim, S. Park, Plasmonic double-walled nanoframes with face-to-face nanogaps for strong SERS activity, Nano Lett. 23 (2023) 6831–6838.
[56] H. Hilal, M. Haddadnezhad, M.J. Oh, I. Jung, S. Park, Plasmonic dodecahedral-walled elongated nanoframes for surface-enhanced Raman spectroscopy, Small 20 (2024) 2304567.
[57] Q. Zhao, H. Hilal, J. Kim, W. Park, M. Haddadnezhad, J. Lee, W. Park, J.W. Lee, S. Lee, I. Jung, S. Park, All-hot-spot bulk surface-enhanced Raman scattering (SERS) substrates: attomolar detection of adsorbates with designer plasmonic nanoparticles, J. Am. Chem. Soc. 144 (2022) 13285–13293.
[58] Z. Liu, J. Ai, P. Kumar, E. You, X. Zhou, X. Liu, Z. Tian, P. Bouř, Y. Duan, L. Han, N.A. Kotov, S. Ding, S. Che, Enantiomeric discrimination by surface-enhanced Raman scattering: chiral anisotropy of chiral nanostructured gold films, Angew. Chem. 132 (2020) 15338–15343.
[59] Y. Wang, X. Zhao, Z. Yu, Z. Xu, B. Zhao, Y. Ozaki, A chiral-label-free SERS strategy for the synchronous chiral discrimination and identification of small aromatic molecules, Angew. Chem. 132 (2020) 19241–19248.
[60] G. Wang, C. Hao, W. Ma, A. Qu, C. Chen, J. Xu, C. Xu, H. Kuang, L. Xu, Chiral plasmonic triangular nanorings with SERS activity for ultrasensitive detection of amyloid proteins in alzheimer's disease, Adv. Mater. 33 (2021) 2102337.
[61] Q. Zhao, J. Lee, M. JinOh, W. Park, S. Lee, I. Jung, S. Park, Three-dimensional Au octahedral nanoheptamers: single-particle and bulk near-field focusing for surface-enhanced Raman scattering, Nano Lett. 24 (2024) 1074–1080.
[62] A.R. Salmon, M.E. Kleemann, J. Huang, W.M. Deacon, C. Carnegie, M. Kamp, B. Nijs, A. Demetriadou, J.J. Baumberg, Light-induced coalescence of plasmonic dimers and clusters, ACS Nano 14 (2020) 4982–4987.
[63] J. Kim, S. Lee, J. Son, J. Kim, H. Hilal, M. Park, I. Jung, J.M. Nam, S. Park, Plasmonic cyclic Au nanosphere hexamers, Small 19 (2023) 2205956.
[64] J. Li, W. Shen, X. Liang, S. Zheng, Q. Yu, C. Wang, C. Wang, B. Gu, 2D Film-like magnetic SERS tag with enhanced capture and detection abilities for immunochromatographic diagnosis of multiple bacteria, Small (2024) 2310014.
[65] J. Nong, L. Tang, G. Lan, P. Luo, Z. Li, D. Huang, J. Shen, W. Wei, Combined visible plasmons of Ag nanoparticles and infrared plasmons of graphene nanoribbons for high-performance surface-enhanced Raman and infrared spectroscopies, Small 17 (2021) 2004640.
[66] Q. Wang, J. Li, Y. Song, L. Duan, C. Yan, L. Qu, Y. Wu, C. Han, Graphene-embedded oblique V-shaped silver nanoarrays for hydrophobic pollutants pre-concentration and high-sensitivity SERS detection, J. Hazard. Mater. 426 (2022) 128085.
[67] H.J. Han, S.H. Cho, S. Han, J.S. Jang, G.R. Lee, E.N. Cho, S.J. Kim, l.D. Kim, M.S. Jang, H.L. Tuller, J.J. Cha, Y.S. Jung, Synergistic integration of chemo-resistive and SERS sensing for label-free multiplex gas detection, Adv. Mater. 33 (2021) 2105199.
[68] Y. Suganami, T. Oshikiri, H. Mitomo, K. Sasaki, Y.E. Liu, X. Shi, Y. Matsuo, K. Ijiro, H. Misawa, Spatially uniform and quantitative surface-enhanced Raman scattering under modal ultrastrong coupling beyond nanostructure homogeneity limits, ACS Nano 18 (2024) 4993–5002.
[69] G. Lu, G. Meng, Q. Liu, L. Feng, J. Luo, X. Liu, Y. Luo, P.K. Chu, Advanced strategies for solid electrolyte interface design with MOF materials, Adv. Powder Mater. 3 (2024) 100154.
[70] C.Y. Lai, Y.T. Chen, S.W. Hsu, Metal-organic framework-Ag nanocomposites as photocatalysts and in situ surface-enhanced Raman spectroscopy sensors to study the mechanisms of CO_2 reduction reactions, ACS Appl. Nano Mater. 7 (2024) 24224–24234.
[71] X. Yang, Y. Liu, S.H. Lam, J. Wang, S. Wen, C. Yam, L. Shao, J. Wang, Site-selective deposition of metal-organic frameworks on gold nanobipyramids for surface-enhanced Raman scattering, Nano Lett. 21 (2021) 8205–8212.
[72] M. Arabi, A. Ostovan, Z. Zhang, Y. Wang, R. Mei, L. Fu, X. Wang, J. Ma, L. Chen, Label-free SERS detection of Raman-inactive protein biomarkers by Raman reporter indicator: toward ultrasensitivity and universality, Biosens. Bioelectron. 174 (2011) 112825.
[73] A. Ostovan, M. Arabi, Y. Wang, J. Li, B. Li, X. Wang, L. Chen, Greenificated molecularly imprinted materials for advanced applications, Adv. Mater. 34 (2022) 2203154.
[74] M. Arabi, L. Chen, Technical challenges of molecular-imprinting-based optical sensors for environmental pollutants, Langmuir 38 (2022) 5963–5967.
[75] X. Chen, A. Ostovan, M. Arabi, Y. Wang, L. Chen, J. Li, Molecular imprinting-based SERS detection strategy for the large-size protein quantitation and curbing non-specific recognition, Anal. Chem. 96 (2024) 6417–6425.
[76] R.R. Wang, M.L. Zheng, W.C. Zhang, J. Liu, T. Li, X.Z. Dong, F. Jin, Micropattern of silver/polyaniline core–shell nanocomposite achieved by maskless optical projection lithography, Nano Lett. 22 (2022) 9823–9830.
[77] S. Gullace, V.M. García, V. Martín, D. Larios, V.G. Consolaro, F. Obelleiro, G. Calogero, S. Casalini, P. Samorì, Universal fabrication of highly efficient plasmonic thin-films for label-free SERS detection, Small 17 (2021) 2100755.
[78] Y. Liu, N. Zhang, D. Tua, Y. Zhu, J. Rada, W. Yang, H. Song, A.C. Thompson, R.L. Collins, Q. Gan, Superhydrophobic 3D-assembled metallic nanoparticles for trace chemical enrichment in SERS sensing, Small 18 (2022) 2204234.
[79] Z.Q. Tian, B. Ren, D.Y. Wu, Surface-enhanced Raman scattering: from noble to transition metals and from rough surfaces to ordered nanostructures, J. Phys. Chem. B 106 (2002) 9463–9483.
[80] B. Ren, Q.J. Huang, W.B. Cai, B.W. Mao, F.M. Liu, Z.Q. Tian, Surface Raman spectra of pyridine and hydrogen on bare platinum and nickel electrodes, J. Electroanal. Chem. 415 (1996) 175–178.
[81] G. Demirel, H. Usta, M. Yilmaz, M. Celik, H.A. Alidagibe, F. Buyukserin, Surface-enhanced Raman spectroscopy (SERS): an adventure from plasmonic metals to organic semiconductors as SERS platforms, J. Mater. Chem. C 6 (2018) 5314–5335.
[82] R. Wang, M. Chen, J. Han, X. Zhang, Z. Zhang, T. Yao, Y. Wang, L. Xu, X. Wang, P. Xu, B. Song, Entropy engineering on 2D metal phosphorus trichalcogenides for surface-enhanced Raman scattering, Adv. Funct. Mater. 34 (2024) 2312322.
[83] J. Li, H. Heng, J. Lv, T. Jiang, Z. Wang, Z. Dai, Graphene oxide-assisted and DNA-modulated SERS of AuCu alloy for the fabrication of apurinic/apyrimidinic endonuclease 1 biosensor, Small 15 (2019) 1901506.
[84] Y. Fan, H. Cheng, C. Zhou, X. Xie, Y. Liu, L. Dai, J. Zhanga, L. Qu, Honeycomb architecture of carbon quantum dots: a new efficient substrate to support gold for stronger SERS, Nanoscale 4 (2012) 1776.

[85] L. Zhang, W. Yi, J. Li, G. Wei, G. Xi, L. Mao, Surfactant-free interfacial growth of graphdiyne hollow microspheres and the mechanistic origin of their SERS activity, Nat. Commun. 14 (2023) 6318.

[86] P. Miao, J.K. Qin, Y. Shen, H. Su, J. Dai, B. Song, Y. Du, M. Sun, W. Zhang, H.L. Wang, C.Y. Xu, P. Xu, Unraveling the Raman enhancement mechanism on 1T′-phase ReS_2 nanosheets, Small 14 (2018) 1704079.

[87] J. Zhou, W. Zhang, Y.C. Lin, J. Cao, Y. Zhou, W. Jiang, H. Du, B. Tang, J. Shi, B. Jiang, X. Cao, B. Lin, Q. Fu, C. Zhu, W. Guo, Y. Huang, Y. Yao, S.S.P. Parkin, J. Zhou, Y. Gao, Y. Wang, Y. Hou, Y. Yao, K. Suenaga, X. Wu, Z. Liu, Heterodimensional superlattice with in-plane anomalous hall effect, Nature 609 (2022) 46–51.

[88] Q. Lv, J. Tan, Z. Wang, P. Gu, H. Liu, L. Yu, Y. Wei, L. Gan, B. Liu, J. Li, F. Kang, H.M. Cheng, Q. Xiong, R. Lv, Ultrafast charge transfer in mixed-dimensional WO_{3-x} nanowire/WSe_2 heterostructures for attomolar-level molecular sensing, Nat. Commun. 14 (2023) 2717.

[89] L. Tao, K. Chen, Z. Chen, C. Cong, C. Qiu, J. Chen, X. Wang, H. Chen, T. Yu, W. Xie, S. Deng, J.B. Xu, 1T′ Transition metal telluride atomic layers for plasmon-free SERS at femtomolar levels, J. Am. Chem. Soc. 140 (2018) 8696–8704.

[90] C. Song, X. Yuan, C. Huang, S. Huang, Q. Xing, C. Wang, C. Zhang, Y. Xie, Y. Lei, F. Wang, L. Mu, J. Zhang, F. Xiu, H. Yan, Plasmons in the van der waals charge-density-wave material 2H-$TaSe_2$, Nat. Commun. 12 (2021) 386.

[91] C.S. Lian, C. Heil, X. Liu, C. Si, F. Giustino, W. Duan, Coexistence of superconductivity with enhanced charge density wave order in the two-dimensional limit of $TaSe_2$, J. Phys. Chem. Lett. 10 (2019) 4076–4081.

[92] Y. Chen, W. Ruan, M. Wu, S. Tang, H. Ryu, H.Z. Tsai, R. Lee, S. Kahn, F. Liou, C. Jia, O.R. Albertini, H. Xiong, T. Jia, Z. Liu, J.A. Sobota, A.Y. Liu, J.E. Moore, Z.X. Shen, S.G. Louie, S.K. Mo, M.F. Crommie, Strong correlations and orbital texture in single-layer 1T-$TaSe_2$, Nat. Phys. 16 (2020) 218–224.

[93] Y. Ge, F. Wang, Y. Yang, Y. Xu, Y. Ye, Y. Cai, Q. Zhang, S. Cai, D. Jiang, X. Liu, B. Liedberg, J. Mao, Y. Wang, Atomically thin $TaSe_2$ film as a high-performance substrate for surface-enhanced Raman scattering, Small 18 (2022) 2107027.

[94] X. Song, Y. Wang, F. Zhao, Q. Li, H.Q. Ta, M.H. Rümmeli, C.G. Tully, Z. Li, W.J. Yin, L. Yang, K.B. Lee, J. Yang, I. Bozkurt, S. Liu, W. Zhang, M. Chhowalla, Plasmon-free surface-enhanced Raman spectroscopy using metallic 2D materials, ACS Nano 13 (2019) 8312–8319.

[95] Q. Lv, J. Tan, Z. Wang, L. Yu, B. Liu, J. Lin, J. Li, Z.H. Huang, F. Kang, R. Lv, Femtomolar-level molecular sensing of monolayer tungsten diselenide induced by heteroatom doping with long-term stability, Adv. Funct. Mater. 32 (2022) 2200273.

[96] C.N.R. Rao, K. Gopalakrishnan, Borocarbonitrides $B_xC_yN_z$: synthesis, characterization, and properties with potential applications, ACS Appl. Mater. Interfaces 9 (2017) 19478–19494.

[97] C. Liang, Z.A. Lu, M. Zheng, M. Chen, Y. Zhang, B. Zhang, J. Zhang, P. Xu, Band structure engineering within two-dimensional borocarbonitride nanosheets for surface-enhanced Raman scattering, Nano Lett. 22 (2022) 6590–6598.

[98] S. Lakshmy, B. Mondal, N. Kalarikkal, C.S. Rout, B. Chakraborty, Recent developments in synthesis, properties, and applications of 2D Janus MoSSe and $MoSe_xS_{(1-x)}$ alloys, Adv. Powder Mater. 3 (2024) 100204.

[99] Y. Zhang, T. Yang, J. Li, Q. Zhang, B. Li, M. Gao, Construction of Ru, O Co-doping MoS_2 for hydrogen evolution reaction electrocatalyst and surface-enhanced Raman scattering substrate: high-performance, recyclable, and durability improvement, Adv. Funct. Mater. 33 (2023) 2210939.

[100] S. Sahoo, R. Kumar, I. Hussain, K. Zhang, Heteroatom doping in 2D MXenes for energy storage/conversion applications, Adv. Powder Mater. 3 (2024) 100246.

[101] Z. He, T. Rong, Y. Li, J. Ma, Q. Li, F. Wu, Y. Wang, F. Wang, Two-dimensional TiVC solid-solution MXene as surface-enhanced Raman scattering substrate, ACS Nano 16 (2022) 4072–4083.

[102] Y. Guo, J. Peng, W. Qin, J. Zeng, J. Zhao, J. Wu, W. Chu, L. Wang, C. Wu, Y. Xie, Freestanding cubic ZrN single-crystalline films with two-dimensional superconductivity, J. Am. Chem. Soc. 141 (2019) 10183–10187.

[103] J.G. Chen, Carbide and nitride overlayers on early transition metal surfaces: preparation, characterization, and reactivities, Chem. Rev. 96 (1996) 1477–1498.

[104] W. Sun, C.J. Bartel, E. Arca, S.R. Bauers, B. Matthews, B. Orvañanos, B.R. Chen, M.F. Toney, L.T. Schelhas, W. Tumas, J. Tate, A. Zakutayev, S. Lany, A.M. Holder, G. Ceder, A map of the inorganic ternary metal nitrides, Nat. Mater. 18 (2019) 732–739.

[105] D. Liu, W. Yi, Y. Fu, Q. Kong, G. Xi, In situ surface restraint-induced synthesis of transition-metal nitride ultrathin nanocrystals as ultrasensitive SERS substrate with ultrahigh durability, ACS Nano 16 (2022) 13123–13133.

[106] G. Zhao, W. Ma, X. Wang, Y. Xing, S. Hao, X. Xu, Self-water-absorption-type two-dimensional composite photocatalyst with high-efficiency water absorption and overall water-splitting performance, Adv. Powder Mater. 1 (2022) 100008.

[107] A. Kundu, R. Rani, K.S. Hazra, Controlled nanofabrication of metal-free SERS substrate on few layered black phosphorus by low power focused laser irradiation, Nanoscale 11 (2019) 16245–16252.

[108] C. Lin, S. Liang, Y. Peng, L. Long, Y. Li, Z. Huang, N.V. Long, X. Luo, J. Liu, Z. Li, Y. Yang, Visualized SERS imaging of single molecule by Ag/Black phosphorus nanosheets, Nano-Micro Lett. 14 (2022) 75.

[109] R. Rani, A. Yoshimura, S. Das, M.R. Sahoo, A. Kundu, K.K. Sahu, V. Meunier, S.K. Nayak, N. Koratkar, K.S. Hazra, Sculpting artificial edges in monolayer MoS_2 for controlled formation of surface-enhanced Raman hotspots, ACS Nano 14 (2020) 6258–6268.

[110] H. Pan, Y. Dong, L. Gong, J. Zhai, C. Song, Z. Ge, Y. Su, D. Zhu, J. Chao, S. Su, L. Wang, Y. Wan, C. Fan, Sensing gastric cancer exosomes with MoS_2-based SERS apta sensor, Biosens. Bioelectron. 215 (2022) 114553.

[111] Y. Ge, Y. Yang, Y. Zhu, M. Yuan, L. Sun, D. Jiang, X. Liu, Q. Zhang, J. Zhang, Y. Wang, 2D TiS_2-nanosheet-coated concave gold arrays with triple-coupled resonances as sensitive SERS substrates, Small (2023) 2302410.

[112] K.L. Firestein, J.E. Treifeldt, D.G. Kvashnin, J.F.S. Fernando, C. Zhang, A.G. Kvashnin, E.V. Podryabinkin, A.V. Shapeev, D.P. Siriwardena, P.B. Sorokin, D. Golberg, Young's modulus and tensile strength of Ti_3C_2 MXene nanosheets as revealed by in situ TEM probing, AFM nanomechanical mapping, and theoretical calculations, Nano Lett. 20 (2020) 5900–5908.

[113] Z. Yu, L. Jiang, R. Liu, W. Zhao, Z. Yang, J. Zhang, S. Jin, Versatile self-assembled MXene-Au nanocomposites for SERS detection of bacteria, antibacterial and photothermal sterilization, Chem. Eng. J. 426 (2021) 131914.

[114] Z. Yu, L. Jiang, R. Liu, W. Zhao, Z. Yang, J. Zhang, S. Jin, Simultaneously intensified plasmonic and charge transfer effects in surface enhanced Raman scattering sensors using an MXene-blanketed Au nanoparticle assembly, J. Mater. Chem. A 10 (2022) 2945–2956.

[115] L. Yang, Y. Peng, Y. Yang, J. Liu, H. Huang, B. Yu, J. Zhao, Y. Lu, Z. Huang, Z. Li, J.R. Lombardi, A novel ultra-sensitive semiconductor SERS substrate boosted by the coupled resonance effect, Adv. Sci. 6 (2019) 1900310.

[116] S. Siddhanta, V. Thakur, C. Narayana, S.M. Shivaprasad, Universal metal-semiconductor hybrid nanostructured SERS substrate for biosensing, ACS Appl. Mater. Interfaces 4 (2012) 5807–5812.

[117] K.H. Lee, H. Jang, Y.S. Kim, C.H. Lee, S.H. Cho, M. Kim, H. Son, K.B. Bae, D.V. Dao, Y.S. Jung, I.H. Lee, Synergistic SERS enhancement in GaN-Ag hybrid system toward label-free and multiplexed detection of antibiotics in aqueous solutions, Adv. Sci. 8 (2021) 2100640.

[118] Y. Liu, H. Ma, X.X. Han, B. Zhao, Metal–semiconductor heterostructures for surface-enhanced Raman scattering: synergistic contribution of plasmons and charge transfer, Mater. Horiz. 8 (2021) 370–382.

[119] J. Zhao, C. Zhou, Y. Guo, Z. Shen, G. Luo, Q. Wu, L. Yang, X. Wang, Z. Hu, Balancing loading mass and gravimetric capacitance of NiCo-layered double hydroxides to achieve ultrahigh areal performance for flexible supercapacitors, Adv. Powder Mater. 3 (2024) 100151.

[120] T. Kokulnathan, T.J. Wang, F. Ahmed, N. Arshi, Fabrication of flower-like nickel cobalt-layered double hydroxide for electrochemical detection of carbendazim, Surf. Interfaces 36 (2023) 102570.

[121] X. Li, X. Lin, G. Fang, H. Dong, J. Li, S. Cong, L. Wang, S. Yang, Interfacial layer-by-layer self-assembly of PS nanospheres and Au@Ag nanorods for fabrication of broadband and sensitive SERS substrates, J. Colloid Interface Sci. 620 (2022) 388–398.

[122] T. Kokulnathan, K.M.A. Kumar, T.J. Wang, E.A. Kumar, A.J. Anthuvan, K.J. Chena, Y.Y. Liang, Plasmonic coupling of silver nanospheres loaded on cobalt-iron layered double hydroxides: a robust SERS probe for 4-nitrophenol detection, J. Mater. Chem. A 12 (2024) 7287.

[123] L. Zhang, Y. Guo, R. Hao, Y. Shi, H. You, H. Nan, Y. Dai, D. Liu, D. Lei, J. Fang, Ultra-rapid and highly efficient enrichment of organic pollutants via magnetic mesoporous nanosponge for ultrasensitive nanosensors, Nat. Commun. 12 (2021) 6849.

[124] D. Zhang, H. You, L. Yuan, R. Hao, T. Li, J. Fang, Hydrophobic slippery surface-based surface-enhanced Raman spectroscopy platform for ultrasensitive detection in food safety applications, Anal. Chem. 91 (2019) 4687–4695.

[125] J. Song, W. Cheng, M. Nie, X. He, W. Nam, J. Cheng, W. Zhou, Partial leidenfrost evaporation-assisted ultrasensitive surface-enhanced Raman spectroscopy in a janus water droplet on hierarchical plasmonic micro/nanostructures, ACS Nano 14 (2020) 9521–9531.

[126] X. Chen, Q. Ding, C. Bi, J. Ruan, S. Yang, Lossless enrichment of trace analytes in levitating droplets for multiphase and multiplex detection, Nat. Commun. 13 (2022) 7807.

[127] G. Brenn, L.J. Deviprasath, F. Durst, C. Fink, Evaporation of acoustically levitated multi-component liquid droplets, Int. J. Heat Mass Tran. 50 (2007) 5073–5086, 2007.

[128] D. Zhang, L. Peng, X. Shang, W. Zheng, H. You, T. Xu, B. Ma, B. Ren, J. Fang, Buoyant particulate strategy for few-to-single particle-based plasmonic enhanced nanosensors, Nat. Commun. 11 (2020) 2603.

[129] X. Guo, J. Li, M. Arabi, X. Wang, Y. Wang, L. Chen, Molecular-imprinting-based surface-enhanced Raman scattering sensors, ACS Sens. 5 (2020) 601–619.

[130] K. Ge, Y. Hu, G. Li, Recent progress on solid substrates for surface-enhanced Raman spectroscopy analysis, Biosensors 12 (2022) 941.

[131] C. Chung, Y.K. Kim, D. Shin, S.R. Ryoo, B.H. Hong, D.H. Min, Biomedical applications of graphene and graphene oxide, Chem. Res. 46 (2013) 2211–2224.

[132] U. Mogera, H. Guo, M. Namkoong, M.S. Rahman, T. Nguyen, L. Tian, Wearable plasmonic paper-based microfluidics for continuous sweat analysis, Sci. Adv. 8 (2022) eabn1736.

[133] Y. Ye, Y. Ge, Q. Zhang, M. Yuan, Y. Cai, K. Li, Y. Li, R. Xie, C. Xu, D. Jiang, J. Qu, X. Liu, Y. Wang, Smart contact lens with dual-sensing platform for monitoring intraocular pressure and matrix metalloproteinase-9, Adv. Sci. 9 (2022) 2104738.

[134] Y. Wang, C. Zhao, J. Wang, X. Luo, L. Xie, S. Zhan, J. Kim, X. Wang, X. Liu, Y. Ying, Wearable plasmonic-metasurface sensor for noninvasive and universal molecular fingerprint detection on biointerfaces, Sci. Adv. 7 (2021) eabe4553.

[135] K. Zhu, K. Yang, Y. Zhang, Z. Yang, Z. Qian, N. Li, L. Li, G. Jiang, T. Wang, S. Zong, L. Wu, Z. Wang, Y. Cui, Wearable SERS sensor based on omnidirectional plasmonic nanovoids array with ultra-high sensitivity and stability, Small 18 (2022) 2201508.
[136] L. Xu, Y. Xie, A. Liu, L. Xie, X. Miao, Z. Hou, L. Xiang, T. Jiang, A. Wu, J. Lin, Innovative applications and perspectives of surface-enhanced Raman spectroscopy technology in biomedicine, Small 21 (2025) 2409698.
[137] D. Cialla-May, A. Bonifacio, T. Bocklitz, A. Markin, N. Markina, S. Fornasaro, A. Dwivedi, T. Dib, E. Farnesi, C. Liu, A. Ghosh, J. Popp, Biomedical SERS–the current state and future trends, Chem. Soc. Rev. 53 (2024) 8957–8979.
[138] Y. Lu, M. Li, Rational design of near-infrared II plasmonic optofunctional materials for diagnostic and therapeutic applications, Adv. Funct. Mater. 34 (2024) 2312753.
[139] N. Lyu, A.H. Barforoushi, L.M.R. Gomez, W. Zhang, Y. Wang, SERS biosensors for liquid biopsy towards cancer diagnosis by detection of various circulating biomarkers: current progress and perspectives, Nano Converg 11 (2024) 22.
[140] H. Lee, W. Kim, M.Y. Song, D.H. Kim, H.S. Jung, W. Kim, S. Choi, One-stop plasmonic nanocube-excited SERS immunoassay platform of multiple cardiac biomarkers for rapid screening and progressive tracing of acute myocardial infarction, Small 20 (2024) 2304999.
[141] X. Lin, D. Lin, Y. Chen, J. Lin, S. Weng, J. Song, S. Feng, High throughput blood analysis based on deep learning algorithm and self-positioning super-hydrophobic SERS platform for non-invasive multi-disease screening, Adv. Funct. Mater. 31 (2021) 2103382.
[142] R. Chen, X. Du, Y. Cui, X. Zhang, Q. Ge, J. Dong, X. Zhao, Vertical flow assay for inflammatory biomarkers based on nanofluidic channel array and SERS nanotags, Small 16 (2020) 2002801.
[143] S.M. Lek, C.W. Ku, J.C.A. Jr, R. Malhotra, N.S. Tan, T. Stbye, T.C. Tan, Validation of serum progesterone <35nmol/L as a predictor of miscarriage among women with threatened miscarriage, BMC Pregnancy Childbirth 17 (2017) 78.
[144] Y.C. Kao, X. Han, Y.H. Lee, H.K. Lee, G.C.P. Quang, C.L. Lay, H.Y. F Sim, V.J.X. Phua, L.S. Ng, C.W. Ku, T.C. Tan, I.Y. Phang, N.S. Tan, X.Y. Ling, Multiplex surface-enhanced Raman scattering identification and quantification of urine metabolites in patient samples within 30 min, ACS Nano 14 (2020) 2542–2552.
[145] D. Chen, Y. Ma, A. Yang, L. Hu, H. Zhou, J. Xu, S. Chen, D. Nie, W. Feng, H. Cai, Y. Cong, J. Pi, L. Rao, X. Huang, P. Sun, H. Zhou, Dual-enhanced SERS satellite immuno-nanocomplex for multiple PSA-mediated PHI assay toward clinical prostate cancer screening, Adv. Sci. 12 (2025) 2411747.
[146] L.T. Afonso, G.A.V. Willson, C.G. Astrain, L.M. Márzan, SERS in 3D cell models: a powerful tool in cancer research, Chem. Soc. Rev. 53 (2024) 5118–5148.
[147] Y. Huang, T. Xie, K. Zou, Y. Gu, G. Yang, F. Zhang, L.L. Qu, S. Yang, Ultrasensitive SERS detection of exhaled biomarkers of lung cancer using a multifunctional solid phase extraction membrane, Nanoscale 13 (2021) 13344–13352.
[148] Y. Gao, H. Zhu, X. Wang, R. Shen, X. Zhou, X. Zhao, Z. Li, C. Zhang, F. Lei, J. Yu, Promising mass-productive 4-inch commercial SERS sensor with particle in micro-nano porous Ag/Si/Ag structure using in auxiliary diagnosis of early lung cancer, Small 19 (2023) 2207324.
[149] N. Li, F. Shen, Z. Cai, W. Pan, Y. Yin, X. Deng, X. Zhang, J.O. Machuki, Y. Yu, D. Yang, Y. Yang, M. Guan, F. Gao, Target-induced core–satellite nanostructure assembly strategy for dual-signal-on fluorescence imaging and Raman quantification of intracellular microRNA guided photothermal therapy, Small 16 (2020) 2005511.
[150] B. Chen, P. Xu, J. Wang, C. Zhang, The role of MiRNA in polycystic ovary syndrome (PCOS), Gene 706 (2019) 91–96.
[151] B. Li, Y. Liu, Y. Liu, T. Tian, B. Yang, X. Huang, J. Liu, B. Liu, Construction of dual-color probes with target-triggered signal amplification for in situ single-molecule imaging of microRNA, ACS Nano 14 (2020) 8116–8125.
[152] P. He, W. Han, C. Bi, W. Song, S. Niu, H. Zhou, X. Zhang, Many Birds, One stone: a smart nanodevice for ratiometric dual-spectrum assay of intracellular MicroRNA and multimodal synergetic cancer therapy, ACS Nano 15 (2021) 6961–6976.
[153] A. Li, X. Qiao, K. Liu, W. Bai, T. Wang, Hollow metal organic framework improves the sensitivity and anti-interference of the detection of exhaled volatile organic compounds, Adv. Funct. Mater. 32 (2022) 2202805.
[154] K. Yang, K. Zhu, Y. Wang, Z. Qian, Y. Zhang, Z. Yang, Z. Wang, L. Wu, S. Zong, Y. Cui, $Ti_3C_2T_x$ MXene-loaded 3D substrate toward on-chip multi-gas sensing with surface-enhanced Raman spectroscopy (SERS) barcode readout, ACS Nano 15 (2021) 12996–13006.
[155] K. Yang, C. Zhang, K. Zhu, Z. Qian, Z. Yang, L. Wu, S. Zong, Y. Cui, Z. Wang, A programmable plasmonic gas microsystem for detecting arbitrarily combinated volatile organic compounds (VOCs) with ultrahigh resolution, ACS Nano 16 (2022) 19335–19345.
[156] W.K. Son, Y.S. Choi, Y.W. Han, D.W. Shin, K. Min, J. Shin, M.J. Lee, H. Son, D.H. Jeong, S.Y. Kwak, In vivo surface-enhanced Raman scattering nanosensor for the real-time monitoring of multiple stress signalling molecules in plants, Nat. Nanotechnol. 18 (2023) 205–216.
[157] M. Arabi, A. Ostovan, Y. Wang, R. Mei, L. Fu, J. Li, X. Wang, L. Chen, Chiral molecular imprinting-based SERS detection strategy for absolute enantiomeric discrimination, Nat. Commun. 13 (2022) 5757.
[158] T. Zhang, Y. Li, X. Lv, S. Jiang, S. Jiang, Z. Sun, M. Zhang, Y. Li, Ultra-sensitive and unlabeled SERS nanosheets for specific identification of glucose in body fluids, Adv. Funct. Mater. 34 (2023) 2315668.
[159] H.Y. Lin, W.R. Chen, L.C. Lu, H.L. Chen, Y.H. Chen, M. Pan, C. Chen, C. Chen, T.H. Yen, D. Wan, Direct thermal growth of gold nanopearls on 3D interweaved hydrophobic fibers as ultrasensitive portable SERS substrates for clinical applications, Small 19 (2023) 2207404.
[160] M. Zhang, Y. Lu, L. Zhang, X. Xu, B. Li, X. Zhao, X. Yan, C. Wang, P. Sun, X. Liu, G. Lu, Flexible and wearable glove-based SERS sensor for rapid sampling and sensitive detection of controlled drugs, Sens. Actuators, B 386 (2023) 133738.
[161] V. Shvalyaa, J. Olenika, D. Vengusta, J. Zavaśnika, J. Štrbaca, M. Modica, O. Baranova, U. Cvelbar, Nanosculptured tungsten oxide: high-efficiency SERS sensor for explosives tracing, J. Hazard. Mater. 476 (2024) 135171.
[162] J. Langer, D.J. Aberasturi, J. Aizpurua, R.A.A. Puebla, B. Auguié, J.J. Baumberg, G.C. Bazan, S.E.J. Bell, A. Boisen, A.G. Brolo, J. Choo, D.C. May, V. Deckert, L. Fabris, K. Faulds, F.J.G. Abajo, R. Goodacre, D. Graham, A.J. Haes, C.L. Haynes, C. Huck, T. Itoh, M.K. ll, J. Kneipp, N.A. Kotov, H. Kuang, E.C.L. Ru, H.K. Lee, J. Li, X.Y. Ling, S.A. Maier, T. Mayerhöfer, M. Moskovits, K. Murakoshi, J.M. Nam, S. Nie, Y. Ozaki, I.P. Santos, J.P. Juste, J. Popp, A. Pucci, S. Reich, B. Ren, G.C. Schatz, T. Shegai, S. Schlücker, L.L. Tay, K.G. Thomas, Z.Q. Tian, R.P. Van Duyne, T.V. Dinh, Y. Wang, K.A. Willets, C. Xu, H. Xu, Y. Xu, Y.S. Yamamoto, B. Zhao, L.M.L. Marzán, Present and future of surface-enhanced Raman scattering, ACS Nano 14 (2020) 28–117.
[163] J.H. Fu, Z. Zhong, D. Xie, Y.J. Guo, D.X. Kong, Z.X. Zhao, Z. Zhao, M. Li, SERS-active MIL-100(Fe) sensory array for ultrasensitive and multiplex detection of VOCs, Angew. Chem., Int. Ed. 59 (2020) 20489–20498.
[164] H.C.S. Chan, H. Shan, T. Dahoun, H. Vogel, S. Yuan, Advancing drug discovery via artificial intelligence, Trends Pharmacol. Sci. 40 (2019) 592–604.
[165] D. Mrdjenovich, M.K. Horton, J.H. Montoya, C.M. Legaspi, S. Dwaraknath, V. Tshitoyan, A.V. Jain, K.A. Persson, A knowledge graph for materials science, Matter 2 (2020) 464–480.
[166] D.E. Blanco, B. Lee, M.A. Modestino, Optimizing organic electrosynthesis through controlled voltage dosing and artificial intelligence, Proc. Natl. Acad. Sci. 116 (2019) 17683–17689.
[167] K. Hansen, F. Biegler, R. Ramakrishnan, W. Pronobis, A. Lilienfeld, K.R. Müller, A. Tkatchenko, Machine learning predictions of molecular properties: accurate many-body potentials and nonlocality in chemical space, J. Phys. Chem. Lett. 6 (2015) 2326–2331.
[168] M. Sumita, X. Yang, S. Ishihara, R. Tamura, K. Tsuda, Hunting for organic molecules with artificial intelligence: molecules optimized for desired excitation energies, ACS Cent. Sci. 4 (2018) 1126–1133.
[169] J.L. Baylon, N.A. Cilfone, J.R. Gulcher, T.W. Chittenden, Enhancing retrosynthetic reaction prediction with deep learning using multiscale reaction classification, J. Chem. Inf. Model. 59 (2019) 673–688.
[170] H. Gao, T.J. Struble, C.W. Coley, Y. Wang, W.H. Green, K.F. Jensen, Using machine learning to predict suitable conditions for organic reactions, ACS Cent. Sci. 4 (2018) 1465–1476.
[171] C.W. Coley, R. Barzilay, T.S. Jaakkola, W.H. Green, K.F. Jensen, Prediction of organic reaction outcomes using machine learning, ACS Cent. Sci. 3 (2017) 434–443.
[172] L.B. Ayres, F.J.V. Gomez, J.R. Linton, M.F. Silva, C.D. Garcia, Taking the leap between analytical chemistry and artificial intelligence: a tutorial review, Anal. Chim. Acta 1161 (2021) 338403.

Heguang Liu earned a master's degree in material physics and chemistry from the Xi'an University of Technology in 2011. And he received a Ph.D. degree from Northwestern Polytechnical University in materials science in 2017. He is currently an associate professor at the Xi'an University of Technology. His research interest mainly focuses on the design, fabrication, and applications of electromagnetic functional materials.

Caiyin You obtained his BS degree from Xi'an University of Technology in 1997 and his PhD degree from the Institute of Metal Research, Chinese Academy of Sciences in 2003. Then he worked as a post-doc researcher in the National Institute for Materials Science in Japan and a research assistant in Oxford University in UK from 2003 to 2009. Now, he is a professor in the school of materials science and engineering at Xi'an University of Technology and his academic interests are mainly related to the investigation of functional materials and battery materials.

Huageng Liang received his B.S. and Ph.D. degrees from Huazhong University of Science and Technology (HUST) in 2003 and 2009, respectively. He currently serves as a Chief Physician in the Department of Urology at Union Hospital, Tongji Medical College, HUST, and is also a Fellow at the School of Materials Science and Engineering, HUST. His research focuses on biomedical materials and devices, as well as surgical robotics. He has authored over 30 peer-reviewed journal articles, with publications in prestigious journals such as *Advanced Materials, Angewandte Chemie International Edition, and ACS Nano*.

Yuan Li is currently a professor in the School of Materials Science and Engineering in Huazhong University of Science and Technology. His research interest is mainly focused on 2D materials and devices. Prof. Li has published more than 80 peer-reviewed papers in Chemical Reviews, Advanced Materials, Advanced Energy Materials, Advanced Functional Materials, ACS Nano, Nano Letters, Materials Horizons and so on. He was elected for National High-level Young Talent Program of China and Chutian Young Scholar in Hubei province.